MODELING AND OBSERVING ATMOSPHERES OF TERRESTRIAL EXOPLANETS

T. GIANG NGUYEN

A DISSERTATION SUBMITTED TO

THE FACULTY OF GRADUATE STUDIES

IN PARTIAL FULFILMENT OF THE REQUIREMENTS

FOR THE DEGREE OF

DOCTOR OF PHILOSOPHY

GRADUATE PROGRAM IN EARTH AND SPACE SCIENCES AND ENGINEERING

YORK UNIVERSITY

TORONTO, ONTARIO

July 2022

Abstract

The recent launch of the James Webb Space Telescope (JWST) allows us to observe more exoplanets and in greater detail. Now that we can characterize terrestrial planets and their atmospheres, this dissertation features several theoretical works that study atmospheric dynamics and infer observability. First, we explore the processes of non-collisional atmospheres to determine the tendency of exospheric volatile transport. We use a Monte Carlo simulation to infer water cold-trapping efficiency for different planetary configurations and find that there are optimal conditions for planetoids to accumulate water on the surface. Planetoids outside these conditions are either too small and thus lose water to thermal escape, or too large and lose water to photodissociation. Bodies similar in size to the moon are ideal for cold-trapping water, which gives great insight into the solar system and its history. Planetoids that build large reservoirs of water, or other volatiles, can evolve to form observable transient collisional atmospheres. While only relatively small planetoids are subjected to exospheric dynamics and therefore not ideal for observations outside the solar system, the dynamics of a half collisional, half non-collisional atmosphere are present in lava planets. Because of the relative ease in observing these planets, they are currently the best target for detecting a rocky exoplanet atmosphere. We modelled the flow of lava planet K2-141b's silicate atmosphere and inferred atmospheric pressure, temperature, and wind speed. We found that SiO should be the dominant gas species and that winds reach supersonic speed, typical for lava planets. However, our analysis where we coupled radiative transfer to the hydrodynamics suggests that the large wind speed induced from a large negative lapse rate cools down the atmosphere much more than previously thought. Therefore, the simulated eclipse spectrum shows absorptive SiO spectral features, as opposed to emission features, that are prominent enough to be observed with JWST. However, the atmosphere is still too thin and the transit depth too small, making observing K2-141b's atmosphere via transmission spectroscopy too difficult with the current technology.

Dedication

For friends and family.

Acknowledgements

First and foremost, I must acknowledge my supervisor Dr. John Moores who has mentored me for the past six years, from the beginning of my Masters. He is an extraordinarily understanding person and has presented me with opportunities that I once couldn't imagine. I wish I share his enthusiasm for both teaching and learning, and greatly appreciated my time in his lab.

I would also like to thank Dr. Mark Gordon who was also stuck with me for six years as a co-supervisor. His many inquiries and suggestions have helped me greatly and pushed my work beyond its many limits. Likewise, I thank Dr. Neil Tandon for supervising me during my PhD. He is another caring person and a great teacher, for students from all walks of life. Without these people, I would not have made it. I would also like to thank my defense committee members: Dr. Regina Lee, Dr. Sarah Rugheimer, and Dr. Michiel Min; I'm sorry I added more work to your schedule.

I thank Dr. Nicolas Cowan for his instrumental help and mentorship in my research. I owe much of my exoplanet knowledge from him and we learned a lot about lava planets together. I also thank Dr. Raymond Pierrehumbert for teaching me the numerical analysis that formed the basis for many of my work. I thank my co-authors Agnibha Banerjee and Dr. Roxana Lupu for their contribution in helping with the research and publications. Finally, I thank the members of the Planetary Volatiles Laboratory, past and present. You have been great friends and I have enjoyed our time inside and outside the office. I wish you all luck.

Table of contents

List of Tables

List of Figures

1 Introduction

1.1 Objective

The rich history of the search for extrasolar planets, or exoplanets, is an integral aspect of human space exploration. Although it is not easy to determine first people to discover an exoplanet, the scientific community now credits Michel Mayor and Didier Queloz as the first to discover an exoplanet around a Sun-like star (Mayor & Queloz, 1995). Since their discovery, the field of exoplanet research has exploded. Missions with ever increasing complexities have led to the discovery of over five thousands exoplanets (Han et al., 2014).

Exoplanets were first detected by using Doppler spectroscopy which relies on ground-based telescopes. However, since 1995, missions such as Spitzer (Werner et al., 2004), Kepler (Koch et al., 2004), and many others (Charbonneau et al., 1999) have use the transit method to discover an ever wide range of exoplanets. Although early exoplanet detections have been of Jupiter-sized planets, technological progress has allowed us to observe smaller terrestrial planets.

With the recent launch of the James Webb Space Telescope (JWST), we can move beyond simply detecting exoplanets and start to characterize them. An important milestone for assessing habitability, discovering unique physical processes, or exploring planetary formation and composition is to detect an exoplanet's atmosphere. Therefore, the culmination of research in this dissertation attempts to uncover the fundamental dynamics of terrestrial atmospheres and how we might observe them.

1.2 Background

1.2.1 The Atmosphere

Earth's atmosphere, and the atmospheres of many other planets, host many processes that dictate how energy and material is distributed throughout the surface. Because of how important Earth's atmosphere is to life, we often look at a planet's atmosphere to infer its habitability. Although we have yet to find an Earth-like atmosphere, studying unique atmospheres of other planets can help us understand the history of the solar system and the wider cosmos.

Atmospheres can be split into different layers with each layer dominated by different physical regimes. Near the surface, the atmosphere is thick and atmospheric mixing is prevalent while the top of the atmosphere is thin, leading to minimal interactions between molecules. The bottom layer is referred as the homosphere where its composition is relatively uniform while the layer above, the heterosphere, is compositionally stratified and arranged by each constituent's molecular mass. The conditions that separate between these layers can be described by the Knudsen number.

The Knudsen number is the ratio between the molecular mean free path and the fluid's characteristic length scale. The mean free path is calculated via $kT/(\sqrt{2}\pi\sigma_d^2 P)$, where k is the Boltzmann constant, T is local temperature, σ_d is the molecule's kinetic diameter, and P is the local pressure. The scale height, H, is usually used for the characteristic length scale: $H = kT/mg$, where m is the molecular mass and g is the surface gravity. A low Knudsen number (<0.01) implies an extremely short mean free path relative to the length scale. Here, the regime allows for continuous flow where constituents frequently interact with one another leading to a "collisional' atmosphere. A high Knudsen number (>10) means the mean free path is on the same scale as the system's length scale, and molecules rarely come close to each other (Dongari & Agrawal, 2012). This is called the free molecular flow regime and it describes the dynamics of the exosphere, where volatile molecules undergo ballistic motion, independent of each other.

1.2.2 Observing Exoplanets

Early detection of exoplanets used the radial velocity method which relied on high-precision ground-based observatories. Although stars exert the greatest gravitational pull in their respective systems, planets also have their own subtle effects on stars. Because the system's centre of mass, the barycentre, is not the star's centre, the star will orbit about this point. This slight movement can induce a doppler shift of the star's light as it travels to the observer. We can detect this subtle shift in the stellar spectra and discover a nearby orbiting planet.

Currently, the majority of exoplanets are discovered via transit methods, although the radial velocity method is still useful for constraining planetary properties once detected. An exoplanet transit occurs whenever a planet moves in front of a star as viewed from an observer. Because of the blocked starlight from the transiting planet, the measured stellar radiation drops significantly enough for detection; this drop is called a the transit depth.

The transit depth of a gas giant closely orbiting a G-type star, such as the Sun, is about 1% of the stellar flux which can easily be seen from ground-based observatories; transit depths for Earth-sized planets are about two orders of magnitude smaller (Burrows, 2014). The transit depth can vary at certain wavelengths due to interactions between stellar radiation and the planet's atmosphere. Therefore, by measuring the stellar spectrum at transit, we can analyze the planet's atmosphere which is the basis behind transmission spectroscopy for exoplanets. This has been done extensively for Hot Jupiters where we can infer atmospheric composition (Barstow et al., 2016; Madhusudhan et al., 2014), cloud properties (Wakeford & Sing, 2015), or wind speeds (Kempton & Rauscher, 2012).

With better space instruments, atmospheric characterization can now be done for rocky Earth-sized planets. By combining different data sets to constrain orbital parameters of an exoplanet, we can begin to model the possible atmosphere. Deciphering atmospheric properties requires matching simulated observations with actual observations. With new data, different aspects of the planet may reveal themselves prompting further refinement and development of the model.

1.2.3 Stellar Impacts on Exoplanets

Studying an exoplanet, as expected, requires extensive knowledge of the nearby star's spectra. Habitable planets are typically sought around main sequence F, G, K, and M-type stars. Fig. 1.1 shows how the stellar spectra relate to effective temperature. Visible and infrared (IR) wavelengths scale relatively consistently with effective temperature but ultraviolet light does not. UV radiation absorption is particularly important because of how well certain molecules absorb it (i.e Ozone) as well as triggering various chemical processes such as the photolysis of water.

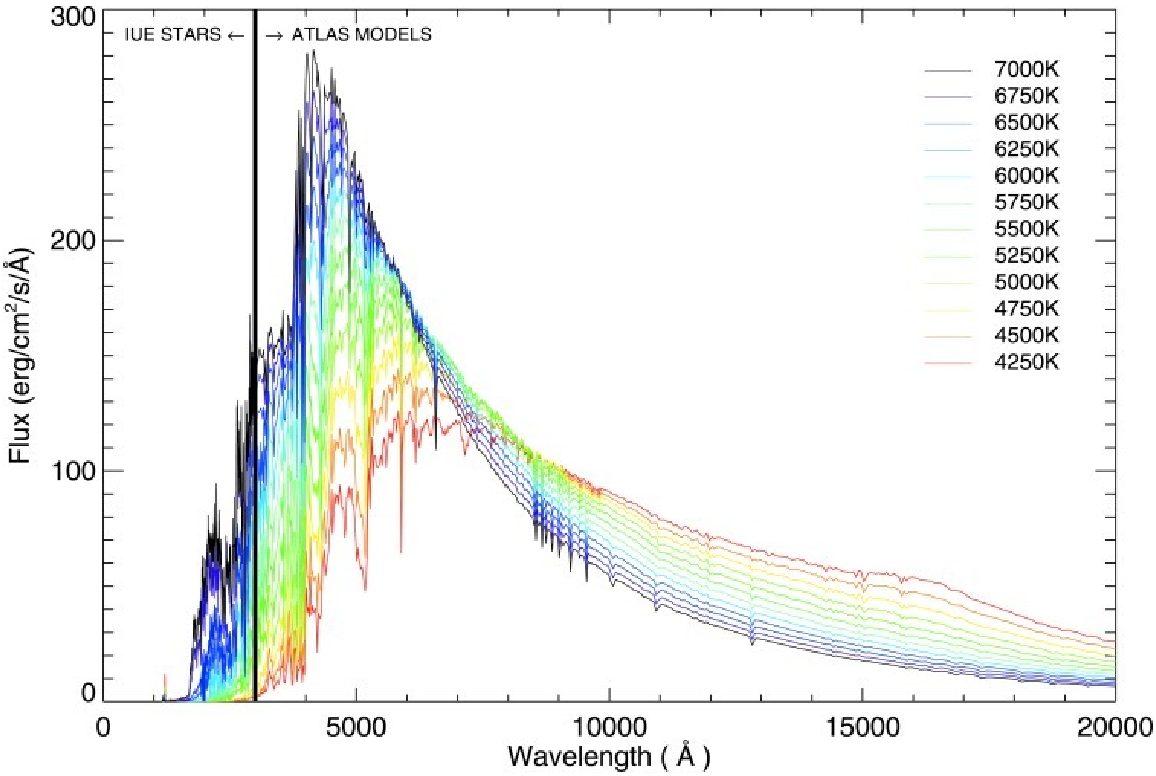

Figure 1.1: Composite stellar spectra with respect to Effective Temperature. Taken from Rugheimer et al. (2013).

UV light can be distinguished between Far (F)UV and Near (N)UV where the wavelength, λ, range is $\lambda <$180 nm and 180 nm $< \lambda <$ 400 nm respectively. M-type and K-type stars have a relatively high FUV to NUV ratio as compared to G-type and F-type stars (Rugheimer et al., 2015). As is often the case, UV atmospheric heating mostly takes place at the top making it vital for for understanding high-altitude processes.

UV stellar radiation is also important for observations. Certain molecules absorb UV very well and measuring the transit depth in the UV may reveal these molecules in the atmosphere. However, to attain a high signal-to-noise ratio, we need to fundamentally catch as many UV photons as possible. This is problematic considering how small UV stellar flux is when compared to visible or IR. Therefore, atmospheric characterization and observation can be sensitive to stellar spectral type.

1.3 Dissertation Content

This dissertation consists of three main projects. The first project, featured in Chapter 2, deals with non-collisional atmospheres. We conduct a parametrical study of water migration in the exosphere using insights from planetoids within the solar system. Here, we test a wide range of orbital configuration to infer the likelihood of cold-trapping water in permanently shadowed regions. This helps to study how water may be distributed in star systems as well as determining which planetoids are likely to exhibit a transient water vapour atmosphere.

This project started with my involvement in Kloos et al. (2019) where I helped Jacob Kloos to calculate surface temperature on the lunar surface. I would adopt the ballistic motion methodology from this work and generalize it to our wide set of planetary properties. I programmed and optimized the model in Python, and handled all the analysis from the model's results. Although featured first in the dissertation, this work is chronologically my last project which has yet been published. However, a manuscript is under preparation where I receive significant help and feedback writing from my supervisor, John Moores.

The next two projects, published as Nguyen et al. (2020) and Nguyen et al. (2022), are spread throughout Chapters 3, 4, and 5. Chapter 3 talks about the discovery of terrestrial lava planet K2-141b and describes the hydrodynamical model used to characterize the planet's atmosphere and magma ocean. It further discusses how the preliminary results may hint at a dominant atmospheric constituent. These works were only possible with NSERC's Technology for ExoPlanetary Sciences (TEPS) program where I was supervised externally by Nicolas Cowan and Raymond Pierrehumbert. The research interest among this academic circle involved characterizing lava planet's atmospheres, and so I was tasked with studying its non-global dynamics using surface boundary layer idealization. I programmed the model from scratch using the equations from Section 3.2. I wrote most of the text for the publications Nguyen et al. (2020) and Nguyen et al. (2022) and also contributed to Zieba et al. (2022) where I added a short formulation and analysis of the model.

While Chapter 3 includes magma ocean discussion, we focus more on the atmosphere in Chapter 4 by including vital radiative processes. This is to harmonize our work with previous radiative transfer models and study how radiative scattering affect the mechanical movement of the atmosphere. The new model also couples the radiative balance between the atmosphere and the surface. These calculations produce unique insights into K2-141b which would eventually help in analyzing Spitzer's observations of the planet (Zieba et al., 2022).

In Chapter 5, we use the results of our 1D radiative hydrodynamical model to prepare for the eventual JWST observations (Dang et al., 2021). The chapter describes how the transmission and emission spectra are simulated at transit and eclipse respectively. While transit spectroscopy is unlikely to detect K2-141b's atmosphere, emission spectroscopy shows great promise for detection by JWST given enough observations. Chapters 2-5 are summarized in Chapter 6 where we also discuss possible future works.

2 | Water Migration in Exospheres

Chapter Summary

Many planetoids in the solar system lack a collisional atmosphere and so volatile transport on these bodies is controlled by exospheric dynamics. Cold-trapping of volatiles which sequesters these gasses as surface ices is an important aspect of the exosphere yet there is a lack of parametrical studies that includes cold-trapping. To fill this gap, we numerically simulate volatile exospheric transport for a wide range of planetary properties with a focus on cold-trapping water molecules in permanently shadowed regions (PSRs). We find that large ballistic hops lead to more cold-trapping while small ballistic hops favour water being photodissociated. Because of the balance between the molecular speed and the surface gravity, an ideal planetoid size exists that maximizes cold-trapping given the solar insolation and bulk density. The Moon coincidentally is almost perfectly sized for cold-trapping water. Therefore, it is expected to build relatively large ice reservoirs in its PSRs.

We start with Section 2.1 where we discuss the scientific motivations for conducting the parametrical study of exospheric water transport. In Sec. 2.2, we detail our Monte Carlo model. We first establish the parameter space (2.2.1), and then describe how water is excited and its motion in the exosphere (2.2.2). Next, we discuss the photodissociation process (2.2.3) and how we generalized the PSR distribution (2.2.4). Section 2.3 presents the results where we first show our model validation (2.3.1) followed by the model's results for our set parameter space (2.3.2). The discussion section, Sec. 2.4, discusses favourable conditions for cold-trapping (2.4.1), implications and applications of our model's results (2.4.2), and caveats of our numerical simulation (2.4.3). Finally, we present the conclusions for this project in Sec. 2.5. This chapter featured work from Jacob Kloos where we had work together on Kloos et al. (2019). I used his program which modelled exospheric transport on the Moon. The code is then generalized and optimized for any given planetoid.

2.1 Motivation

Surface-bound exospheres are very common in the solar system where exospheric processes dominate the dynamics on planetary bodies such as the Moon, Mercury, and Ceres. Exospheric dynamics are therefore vital for understanding the molecular surface distribution on these airless bodies. Because of the significant interest in exospheres, partly driven by lunar exploration, there have been many studies on this subject.

Most studies of volatile transport in an exosphere focus on specific bodies such as the Moon (e.g. Kloos et al., 2019; Moores, 2016; Schorghofer, 2014), Ceres (e.g. Schorghofer et al., 2016), and various outer solar system bodies (e.g. Steckloff et al., 2022). The work of Killen, Burger, and Farrell (2018) studies general exospheric trends across a wide range of planet size and surface temperature. However, this study focused on gravitational escape of molecules therefore neglecting photodissociation and cold-trapping mechanisms. Another study by Steckloff et al. (2022) did account for photodissociation across for many outer solar system moons but likewise ignored cold-trapping.

Cold-trapping volatiles is an important aspect of exospheric dynamics as it acts to retain volatile molecules, such as water, that would otherwise be lost to space. Substantial reservoirs can build up at the polar regions, even for highly irradiated bodies such as Mercury (Deutsch, Neumann, & Head, 2017). Large impacts or sudden change of obliquity can expose the polar ice and potentially produce transient collisional atmospheres. Therefore, understanding these exospheric processes may yield great insights into how certain molecules are distributed throughout the solar system as well as within other star systems.

Our objective is to determine the orbital parameter space for which cold-trapping water is efficient. We focus on water as it is important towards human exploration (particularly on the Moon) as well as characterizing habitability for exoplanets and exomoons. Water transport on surface-bound exospheres is also well-studied which makes it easy to validate models. In this study, we run a Monte Carlo simulation for various orbital configurations to determine the fates of water molecules as they travel within the exosphere. Illustrations of similar numerical simulations can be found in Appendix A.1, Fig. A.1.

2.2 The Monte Carlo Simulation

2.2.1 Finding the Parameter Space

Our methods are similar to that of Kloos et al. (2019) but instead of focusing on the Moon, we will test many planetary bodies with varied physical properties. When a molecule's thermal velocity is comparable to the planet's escape velocity, the molecule is likely to escape to space and the exosphere is not bound to surface. On the other hand, when the escape velocity is much greater than the thermal velocity (generally at least 6 times), Jeans escape is negligible and the molecule will bounce around the surface indefinitely barring any chemical processes (Catling & Kasting, 2017). Therefore, the parameter space of interest lies between these two boundaries.

Given the computation intensiveness of the Monte Carlo simulation done by Kloos et al. (2019), we must be pragmatic about which physical properties and orbital configurations to parameterize. Because volatile transport on exospheres depends mostly on the balance between the kinetic energy and the gravitational energy, it is prudent to simply vary the planet's bulk density, radius, and received stellar flux. Unfortunately, this means that we cannot directly account for orbital properties such as the planet's rotation, eccentricity, and many others. For these specified properties, we assume a rotational period of one Earth day and zero eccentricity.

The lower limit for received stellar flux is determined by the minimum energy required to excite a water molecule on the surface which initiates its ballistic migration. The upper limit is determined by the photodissociation timescale with respect to the ballistic hopping timescale where the water will almost certainly undergo photolysis before being cold-trapped. Through preliminary simulations, setting the maximum stellar flux to sustain a max surface temperature of 800 K ensures this. We set the bulk density to range between 2 - 6 g cm^{-3}. The radius range is subsequently set via the ratio between the molecular speed and the escape velocity. This gives us the parameter space shown in Fig. 2.1.

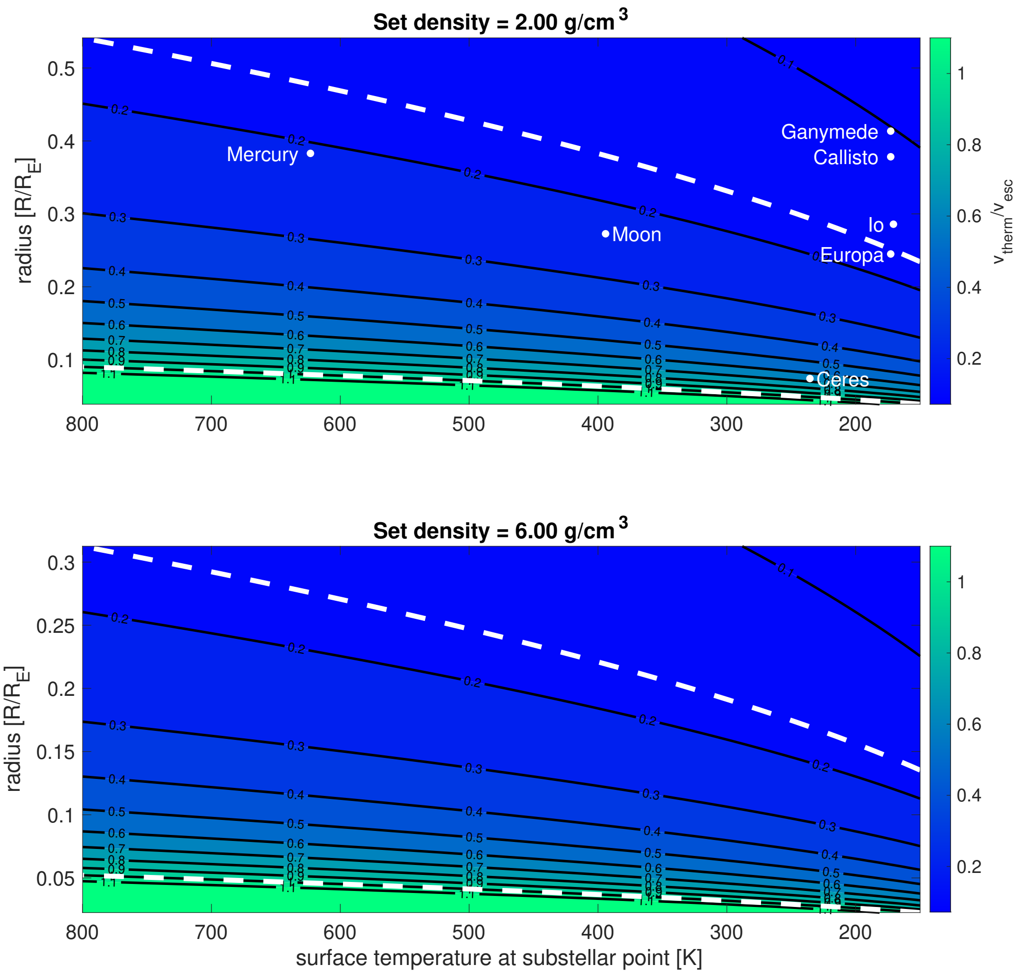

Figure 2.1: Parameter space of interest for exospheres as described in 2.2.1. The colour map shows the ratio between the thermal velocity and escape velocity. The area above the top dashed line is where the thermal velocity is small ($\sim$1/6) compared to the escape velocity, therefore molecules are expected to be bound to the exosphere. The area below the lower striped line is where the thermal velocity is greater than the escape velocity, and molecules are expected to escape from the exosphere. The area in between and around the boundaries is the parameter space of interest, where determining whether water molecules will be bound to the exosphere or escape from it is not trivial.

2.2.2 Modeling Ballistic Motion

With the parameter space established, we can now describe the dynamics that will govern water migration in an exosphere. We first explore how a water molecule is sublimated which begins the ballistic hopping. We assume thermal equilibrium between the surface and the molecules. This allows us to calculate the adsorption residence time, t_{res}, which determines how long the molecule stays on the surface before being released from the surface. Langmuir (1916) defined this as:

$$t_{\mathrm{res}} = \frac{1}{\upsilon_0} \exp\big(\frac{E_a}{k_B T_e}\big), \tag{2.1}$$

where υ_0 is the lattice vibrational frequency of water which is 2×10^{12} s^{-1} (Sandford & Allamandola, 1988), E_a is the activation/binding energy which is typically taken to be 0.53 eV (Schorghofer & Taylor, 2007), k_B is the Boltzmann constant, and T_e is the equilibrium temperature between the molecule and the surface. When the residence time, t_{res}, is short enough (< 1 hr), the molecule is thermally active enough to escape from the surface.

Molecules are initially randomly placed around the substellar point where the surface temperature is hot enough to have very short residence time ($t_{res} < 1$ s). If a molecule finds itself on the nightside, it must wait until dawn for surface temperatures to increase so that the water can be sublimated. When the molecule is released, we assume it has the same temperature as the surface which allows us to apply the classical Maxwell-Boltzmann molecular speed distribution:

$$D = \frac{4s^{3/2}}{\sqrt{\pi}} v^2 e^{-sv^2}, \tag{2.2}$$

where v is the molecular speed. The variable s is defined by the molecular mass, m:

$$s = \frac{m}{2k_B T_e}. \tag{2.3}$$

We assume the surface is in thermal equilibrium with the incoming stellar flux and so, surface temperature is calculated as:

$$T_e = \left(\frac{F_*}{\sigma} \cos\theta \right)^{1/4}, \tag{2.4}$$

where F_* is the stellar flux, σ is the Stefan-Boltzmann constant, and θ is the angular distance from the substellar point. Note that θ not only depends on the location of the molecule, but also on the position of the star in the planet's sky.

With the escaping molecule's speed dictated by the Maxwell-Boltzmann distribution dependent on the surface temperature, its trajectory is evenly distributed across all angles of the sky. Therefore, the azimuth angle is randomized uniformly while the elevation angle is weighted by a cosine factor to account for smaller spherical grid size when approaching the zenith. If the molecular speed exceeds the escape velocity, then the molecule is lost due to thermal Jeans escape. If not, the molecule travels in a ballistic motion purely influenced by gravity due to the lack of a collision-induced atmosphere (Watson, Murray, & Brown, 1961). During the ballistic hop, the molecule can also be destroyed via photodissociation.

2.2.3 The photodissociation Process

Exposure to starlight can split water molecules into H, O, and OH products. This occurs in the UV range for two different absorption bands: $\lambda < 145$ nm and 145 nm$< \lambda < 186$ nm. Water photolysis from the Sun occurs mainly in the second band accounting for 53% of molecules destroyed. On the other hand, the band $\lambda < 145$ nm generally accounts for small amount of photodissociation except for the Ly α emission at λ =121.6 nm (Crovisier, 1989).

Because photodissociation depends almost entirely on the UV radiation, its rate should vary significantly for stars other than the Sun which is a G2V star with an effective temperature of 5800 K. In the NUV (180-400 nm), the flux [W m^{-2} nm^{-1}] scales with stellar spectral class: F $\sim 10^{-1} - 1$, G $\sim 10^{-2} - 10^{-1}$, K $\sim 10^{-3} - 10^{-2}$, and M $\sim 10^{-4}$ –10^{-3}. However, the FUV (<180 nm) stellar flux does not have the same scaling and there is less distinction between the star types. Therefore, M-type and K-type stars have significantly high FUV to NUV flux ratio relative to F-type and G-type stars (Rugheimer et al., 2015).

The Ly α solar emission accounts for a significant 36% of molecules destroyed. The emission at this wavelength originates from the transition region between the chromosphere and the corona (Lean & Skumanich, 1983). Furthermore, solar Ly α

emission can vary up to 10% throughout several cycles owing to the Sun's rotation and interior dynamics (Machol et al., 2019; Woods et al., 2000). Ly α emission for various FGKM stars can be found in France et al. (2018).

Going back to the model, received stellar flux is a parameter we adjust and it depends almost entirely on stellar properties and the planet's proximity to it. However, since we starting with the Sun, we are essentially testing different orbital radii from a G-type star. At 1 AU, this corresponds to a rate of 1.26×10^{-5} molecules/s destroyed for current average solar conditions (Crovisier, 1989). The probability of photolysis is dependent on stellar intensity and likewise follows the inverse square law. Therefore, following Steckloff et al. (2022) and Kloos et al. (2019), the probability of photodissociation, P_{photo}, is:

$$P_{\text{photo}} = 1 - \exp\left(\frac{-t_{\text{fly}}}{t_{\text{photo}}}\right), \tag{2.5}$$

where t_{fly} is the cumulative time the molecule spent being airborne (exospheric residence time). The photodissociation timescale, t_{photo}, is calculated from the planet's proximity to the star d:

$$t_{\text{photo}} = t_{\text{photo@1AU}}\left(\frac{1AU}{d}\right)^2. \tag{2.6}$$

For the tracked molecule's initial hops, the cumulative airborne time is low and photodissociation is unlikely to occur. The molecule's position depends on its randomized trajectory and speed determined from the Maxwell-Boltzmann distribution. If the molecule lands far from the equator, it may find itself in a permanently shadowed region (PSR). Here, surface temperature is very low and the adsorption residence time is too long making it impossible for the molecule to be thermally released back from the surface. Although the molecule is lost to the exosphere and our simulation of it ends, PSRs can accumulate water which can later be released non-thermally by meteor impacts (Benna et al., 2019). All the parameters mentioned in this chapter can be found in Table A.1 along with their descriptions.

2.2.4 The Permanently Shadowed Regions

Planetary bodies that have low obliquity with respect to the ecliptic, such as the Moon, Mercury, or Ceres can host large permanently shadowed regions. With an obliquity of less than 1.59°, the total area of PSRs on the Moon is 31,059 km^2, or 0.08% of its surface (McGovern et al., 2013). Ceres, with a slightly higher obliquity of 4°, hosts approximately 1800 km^2 of PSRs in the northern hemisphere, or 0.13% of the hemisphere (Schorghofer et al., 2016). Ceres' obliquity has historically been as high as 20°, yet Ermakov et al. (2017) showed that PSRs on Ceres still exist for this extreme condition, although the total area will only add up to 1.6 km^2.

PSRs on planetary bodies mentioned above are essentially areas within impact craters near the polar regions. Therefore, the age of the planet plays an important role in forming PSRs as older planetoids will be bombarded more than younger ones.

Relatively large impact events at the poles can significantly change the total area of PSRs, which explains the moon's asymmetrical PSR distribution between the northern and southern hemisphere. This becomes even more prominent for smaller bodies.

While PSRs are formed by seemingly random processes, we can still establish their distribution using data from the Moon. However, this means that our test planetary body has to share the moon's low obliquity and age. Due to the moon's proximity from Earth, its topography is well studied and we can use data from the Lunar Reconnaissance Orbiter (McGovern et al., 2013) to determine the distribution of PSRs with respect to latitude (see Fig. 2.2, top panel). We can further parameterize the amount of PSRs by scaling the lunar PSR distribution to give us the bottom panel of Fig. 2.2. This is useful later where we vary the PSR coverage and see its effects on cold-trapping water.

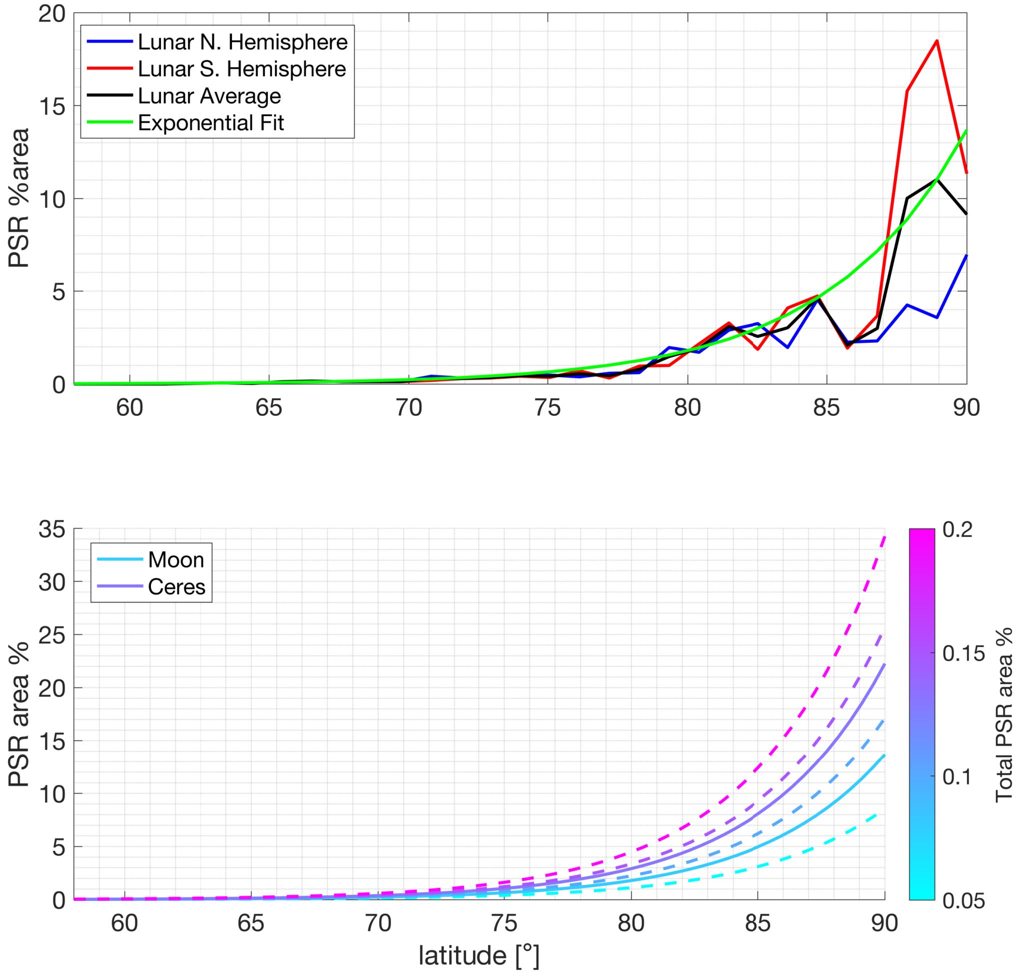

Figure 2.2: Lunar PSRs and PSR coverage. *Top*: Permanently shadowed regions with respect to latitude on the Moon. The blue and red lines show the northern hemisphere and southern hemisphere regions respectively; the black line is the average of the two and the green line is the fit for the averaged data. *Bottom*: The PSR distribution scaled to different PSR coverage. The colours correspond to the total PSR area percentage; the Moon and Ceres (solid lines) have 0.08% and 0.13% of their surface area covered in constant darkness, respectively.

Interpolating the data of the Moon's PSRs yields a latitudinal dependence, which we can broadly apply to our test cases. This is particularly useful because we can avoid building actual topography and use ray-tracing to find the PSRs. The data is rather a conservative estimate due to the spatial resolution of the observations. Surface topography smaller than 1 km in scale is unaccounted for and theoretical "micro cold traps" should account for a considerable amount of shadowed regions (Hayne, Aharonson, & Schörghofer, 2021).

In summary, we ran a Monte Carlo simulation to characterize a planetary body's ability to retain water in its permanently shadowed regions. The process starts with a molecule tracer being thermally excited near the substellar point. Its trajectory is randomized but its speed is taken from the Maxwell-Boltzmann distribution. As the molecule travels, it can escape if the molecular speed is fast enough or it can be destroyed via photolysis. Upon landing, the probability of being cold trapped is inferred from the observed lunar PSRs distribution. We do this for 10^4 molecules per orbital configuration, where each setup lies within the parameter space described in 2.2.1.

2.3 Results

2.3.1 Model Validation

Initially we run the simulation for the moon with 10^6 tracer water molecules which is on par with Moores (2016) and other lunar exospheric models. Approximately 19.4% of all molecules were trapped, which agrees well with Kloos et al. (2019); they recorded 10.7% and 11% of particles trapped in the northern and southern hemisphere respectively. This result is shown as Fig 2.3.

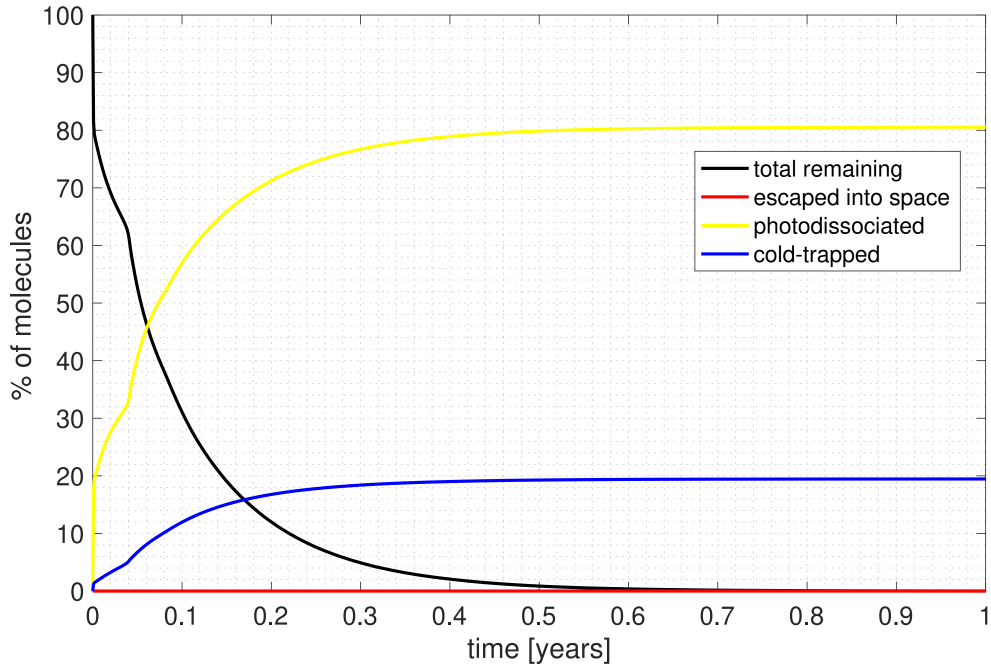

Figure 2.3: Simulated molecules tracked with time. The black line shows the percentage of molecules remaining in the simulation. The yellow, blue, and red lines show the percentage of molecules that have been lost due to photolysis, cold-trapped, and escaped to space respectively.

We also test how varying the solar radiation affects how much water is cold-trapped. This is shown in Fig. 2.4 where we can see that, as expected, lower flux leads to more trapping. This is mainly due to a lower photodissociation rate which scales linearly with insolation as explained in 2.2.3. This exercise also serves to decide how many tracers should be run per case.

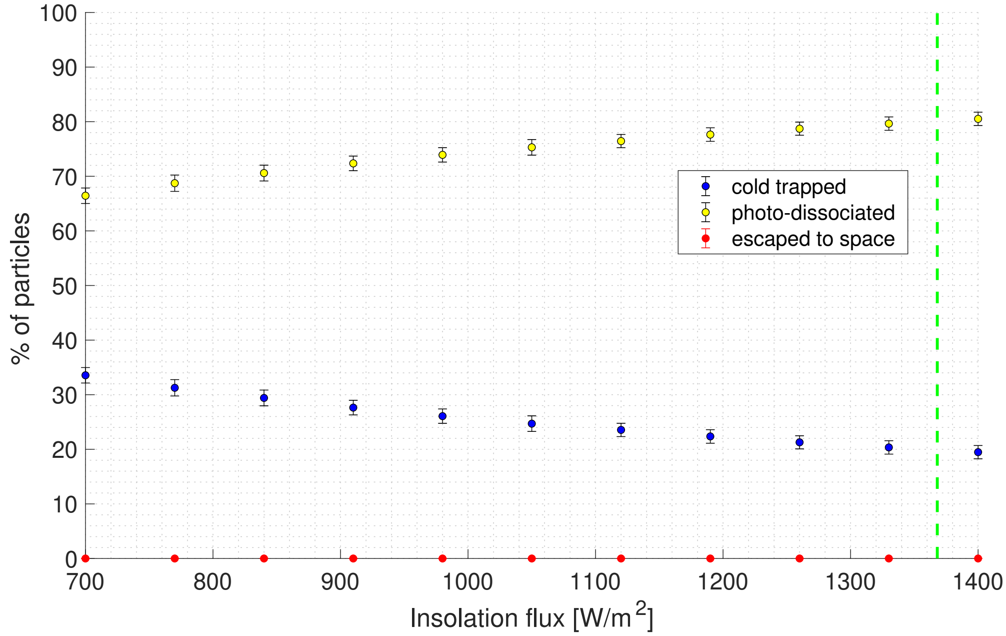

Figure 2.4: Relationship between molecules being cold-trapped or photodissociated on the Moon as solar flux is varied. Each case has a total of 10^6 tracers but if we split the run into 100 smaller runs with 10^4 tracers, then the error bar represents 3 standard deviations for the smaller runs. These 3σ error bars are very small implying that running a simulation with 10^4 molecules will yield negligible differences from simulations with more tracers.

Each molecule can jump over 1000 times before being lost to the system which can be computational intensive. Characteristic of Monte Carlo simulations, increasing the amount of tracers used will yield diminishing returns on precision after a certain point; this point was deemed to be 10^4 molecules. As seen in Fig. 2.4, the difference between 10^6 and 10^4 tracers is negligible yet the computational time is much greater for the former.

2.3.2 Results for the Parameter Space

We run the Monte Carlo simulation for different planetary bodies with varying radii, substellar surface temperature at different bulk densities. The parameter space grid is shown in Fig. 2.5 with each point having 10^4 simulated molecules. We can then further interpolate the grid to produce Fig. 2.6.

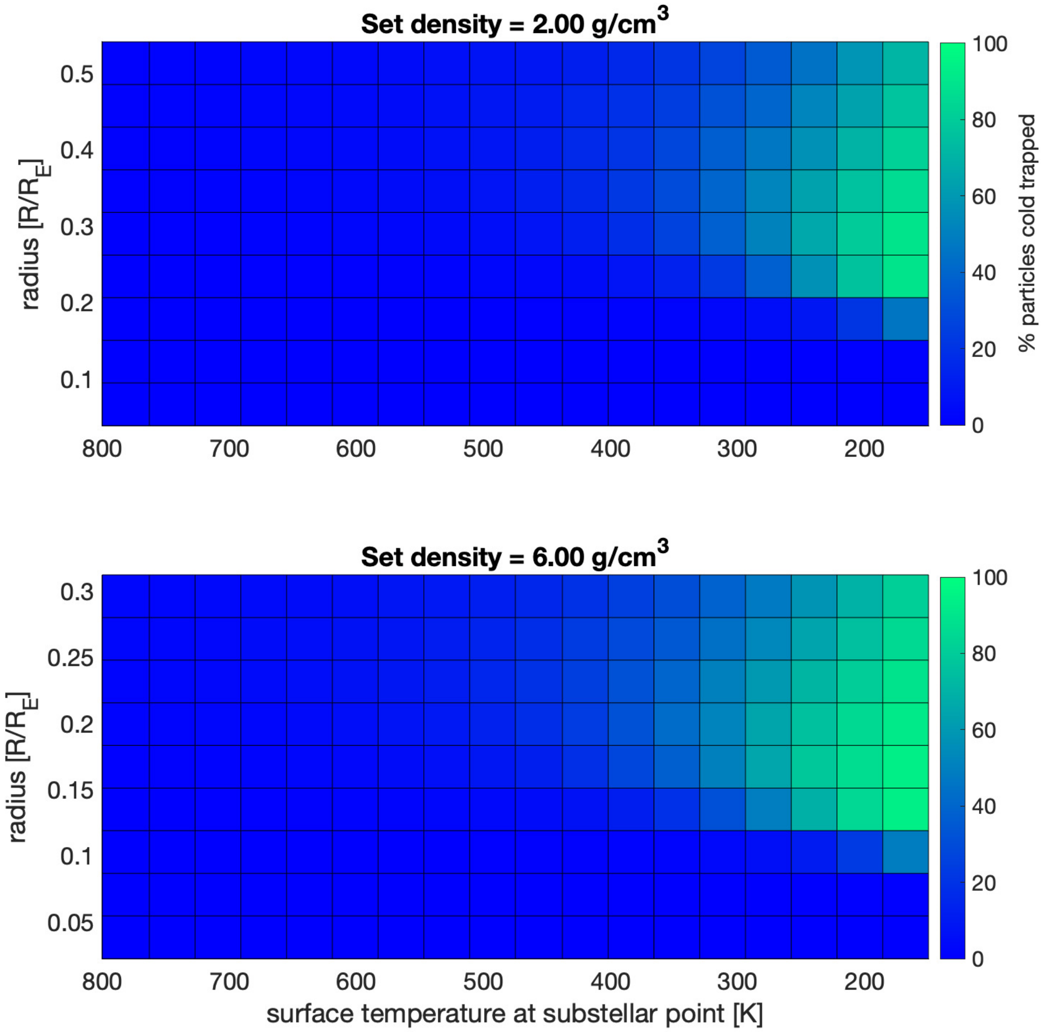

Figure 2.5: Percentage of molecules being cold-trapped within the parameter space shown in Fig. 2.1. Note that the temperature axis is reversed.

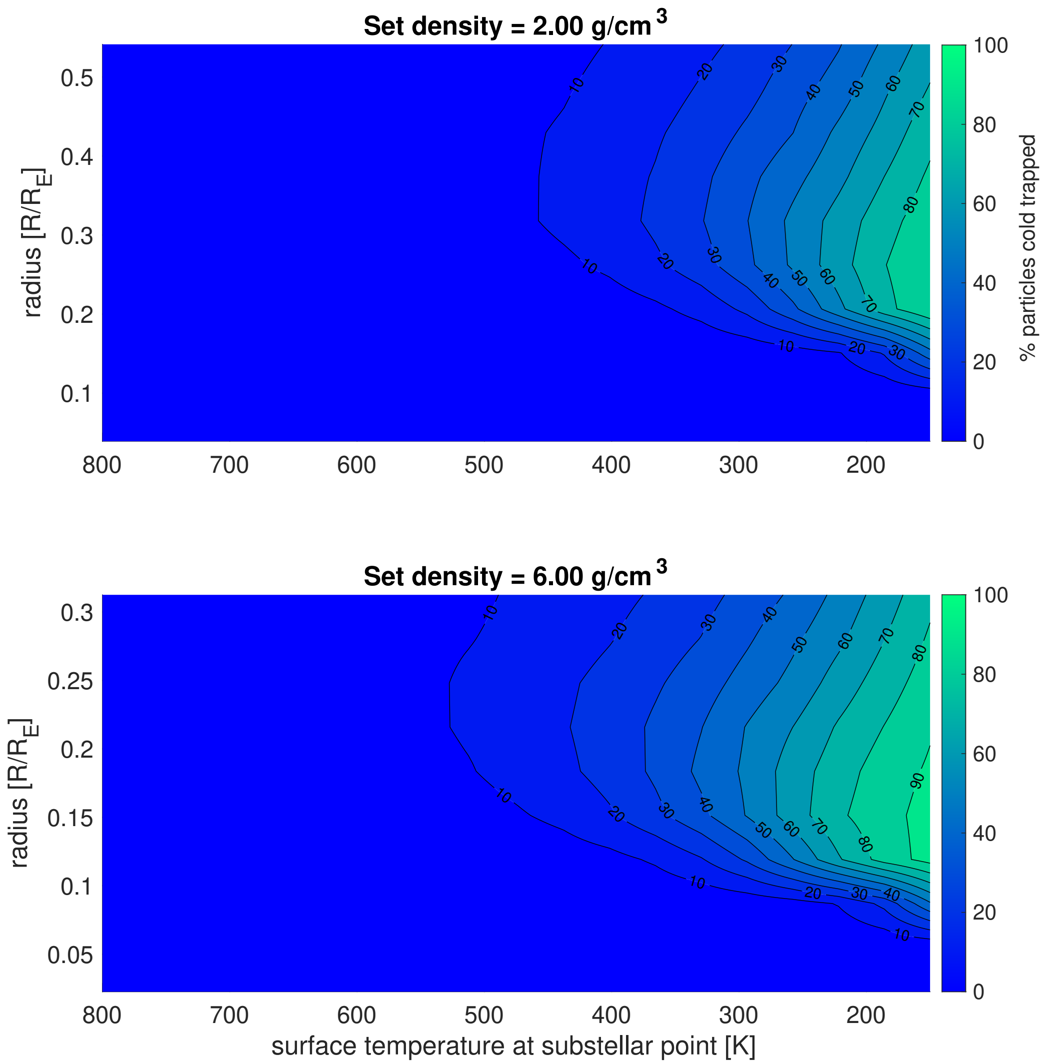

Figure 2.6: Percentage of molecules being cold-trapped interpolated from Fig. 2.5.

When analyzing the parameter space to determine favourability of cold-trapping, photodissociation, and thermal escape, three prominent zones can be seen, as shown in Fig 2.7. A radius smaller than 0.1 R_E has little gravity so the overwhelming amount of simulated tracers are lost to space. Planetoids with temperatures at the substellar point greater than 550 K will cause a significant amount of water molecules to be photodissociated. This is due to the very short photo-dissociation timescale caused by the intense stellar radiation. Plots similar to Fig. 2.7 but at different bulk densities can be found in Appendix A.3.

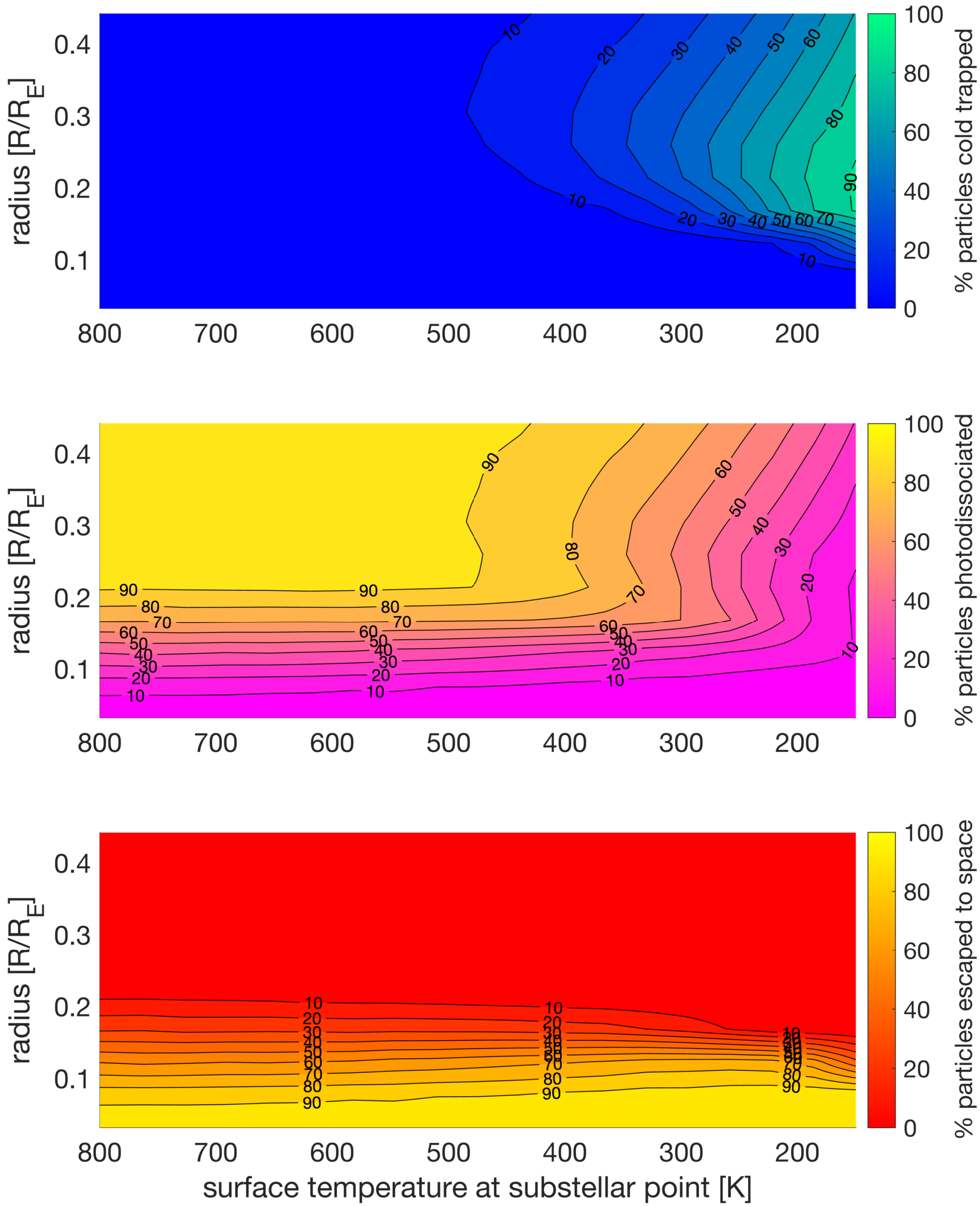

Figure 2.7: Cold-trapping (*top*), photodissociation (*middle*), and thermal Jeans escape (*bottom*) within the parameter space. Small planetary radii favours thermal escape while hot and large planetoids increase the likelihood of photodissociation. Cold but moderately sized planetoids maximizes the amount of water cold-trapping. The bulk density is set to 3 g cm^{-3}. The results at different densities can be found in Appendix A.3.

2.4 Discussion

2.4.1 Cold-trapping Efficiency

As seen in Fig. 2.7, having a small radius lowers the gravity for a set bulk density, and induces significant thermal Jeans escape. This makes water cold-trapping inefficient, regardless of the stellar flux used. However, having a large radius also lowers the amount of molecules being cold-trapped. Therefore, as seen in Fig. 2.8, an ideal size exists that maximizes cold-trapping at a given stellar flux. The dynamics at play revolve around how quickly molecules can reach the polar regions with an abundance of PSRs compared to the photodissociation time-scale.

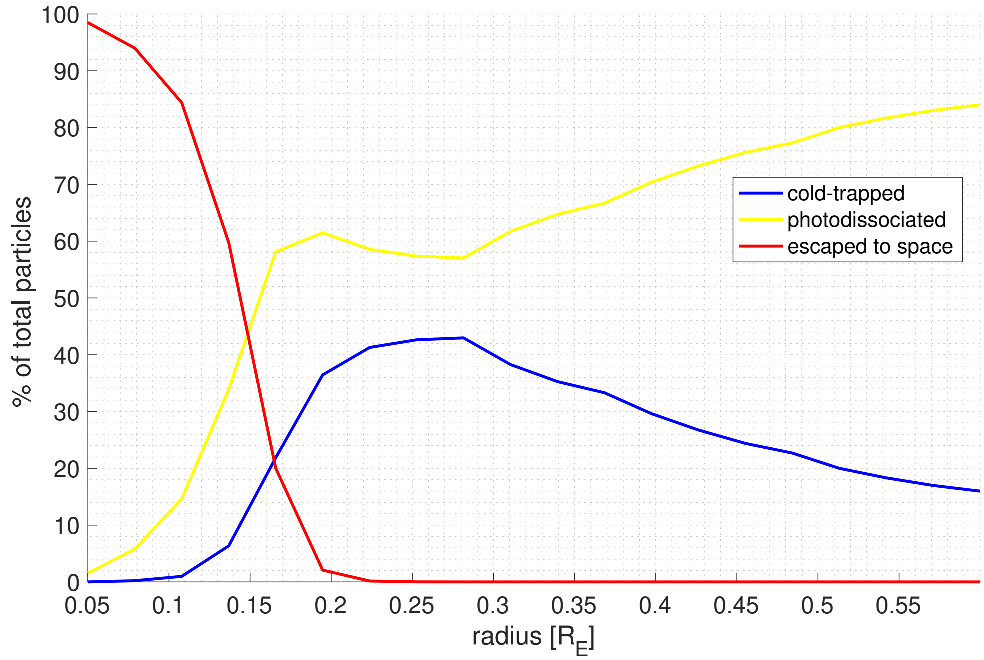

Figure 2.8: Cold-trapping (blue), photodissocation (yellow), and thermal escape(red) of water at 300 K and planetary bulk density of 3 g cm^{-3}. When the planet's radius is small, gravity is weak and thermal escape is likely for the water molecule. At larger radii, photodissociation is dominant due to longer distances and more requiring more ballistic hops for molecules to reach the PSRs.

Photodissociation timescale depends only on incoming stellar radiation and is therefore independent from the planetary body's physical properties. However, the odds of photolysis is determined via the ratio between the photodissociation and ballistic timescale and the total time the molecule spent airborne. This total flight time depends on both surface gravity and molecular speed.

At a given bulk density, planetary volume, and likewise mass, has a cubic relation with radius. On the other hand, gravitational force follows the inverse square law and consequently shares a quadratic relation with radius. Because of these two relationships, surface gravity will always increase with respect to planetary radius within the context of our numerical simulations. This is shown in Fig. 2.9.

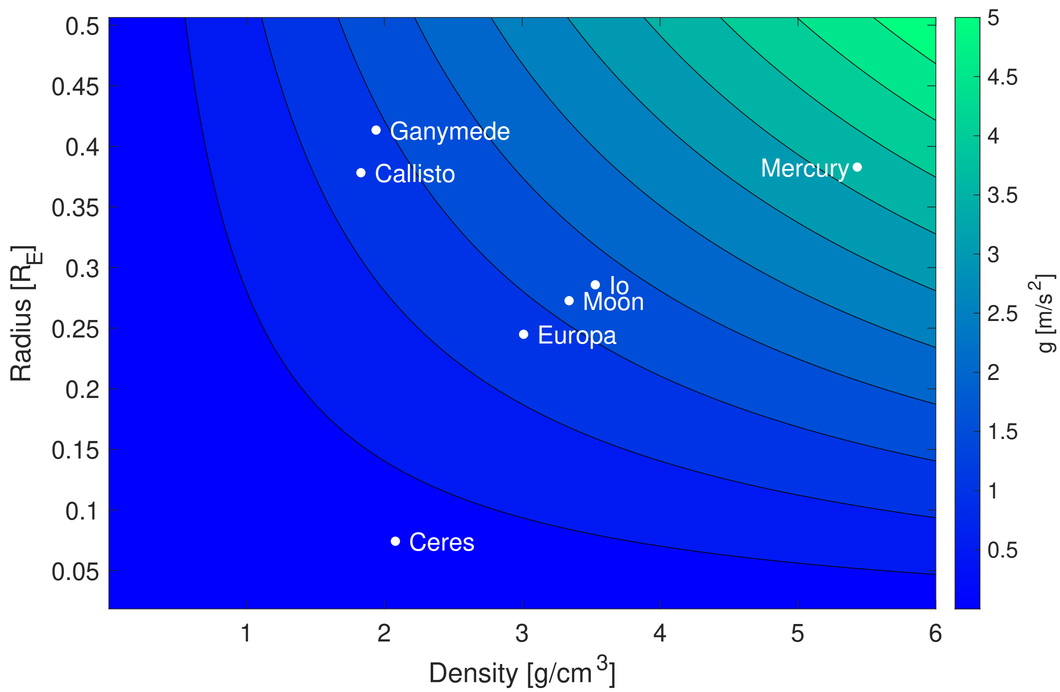

Figure 2.9: Surface gravity with respect to planet's radius and bulk density. At fixed density, increasing the planetary radius also increases the gravitation force.

Coming back to our example where the stellar flux is fixed (Fig. 2.8), the thermal speed of a molecule is also fixed and therefore the molecule's initial velocity is constant regardless of the planet's size and mass. Since gravity is stronger for larger planets, each ballistic hop has a shorter distance and flight time. However, as seen in Fig. 2.10, there is a negligible difference between total flight time and distance travelled between planets of different sizes ; the only noticeable contrast comes from the number of ballistic hops. Molecules on the smaller planetoid would generally take fewer jumps before water molecules become cold-trapped or photodissociated.

If we isolate data from Fig. 2.10 to include only cold-trapped molecules, we get Fig. 2.11. In the figure, we can see that the number of jumps made is the largest distinguishable factor between different test radii. The cumulative flight time and distance traveled for cold trapped particles appear to have the same timescale and length scale, regardless of planetary size. Evidently but counter-intuitively, the model shows that having relatively few ballistic hops maximizes the chance of excited molecules landing in PSRs.

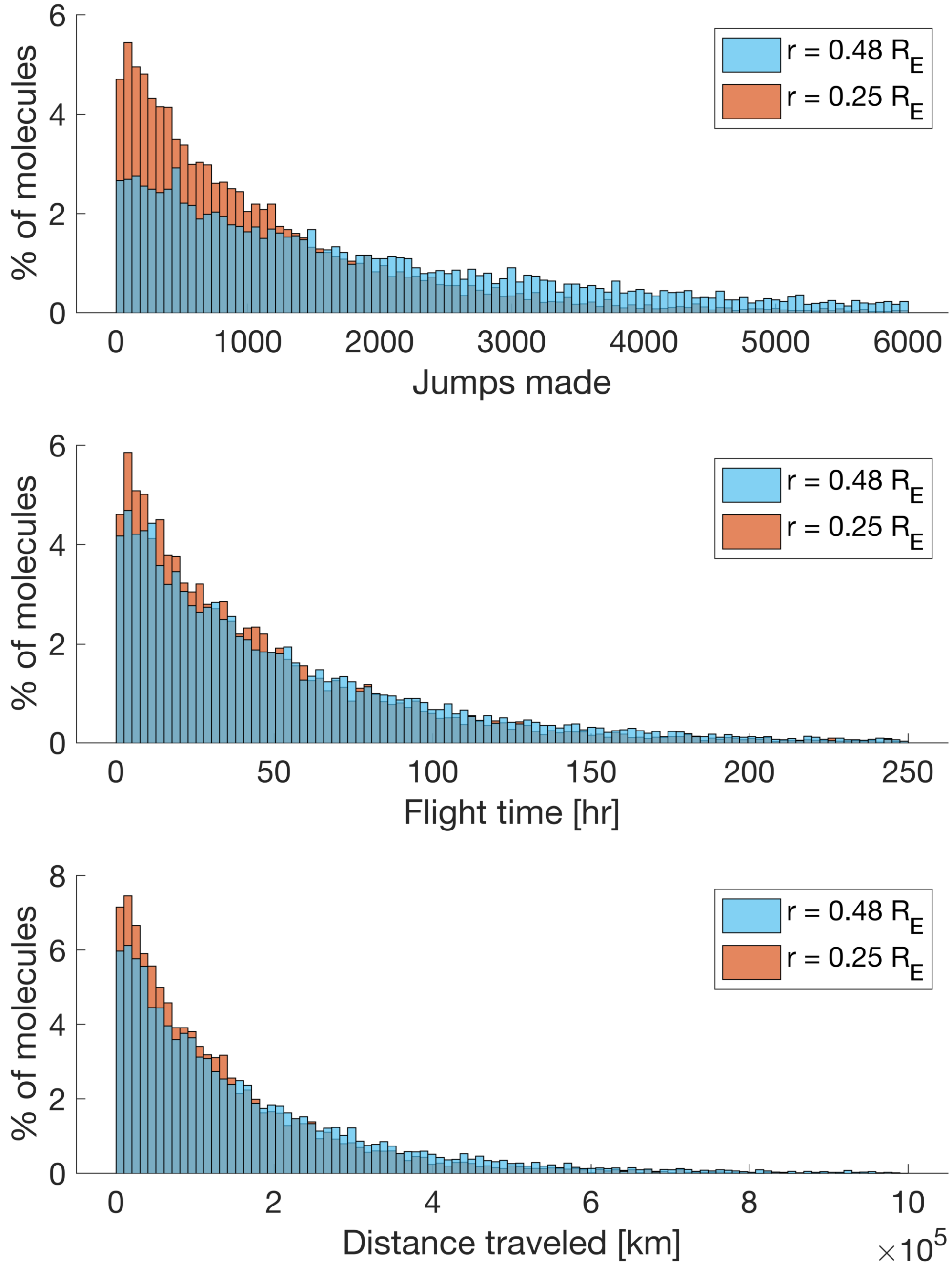

Figure 2.10: Distribution of jumps made (*Top*), cumulative flight time, or exospheric residence time (*Middle*), and cumulative distance traveled (*Bottom*). Both cases have a max surface temperature of 300 K.

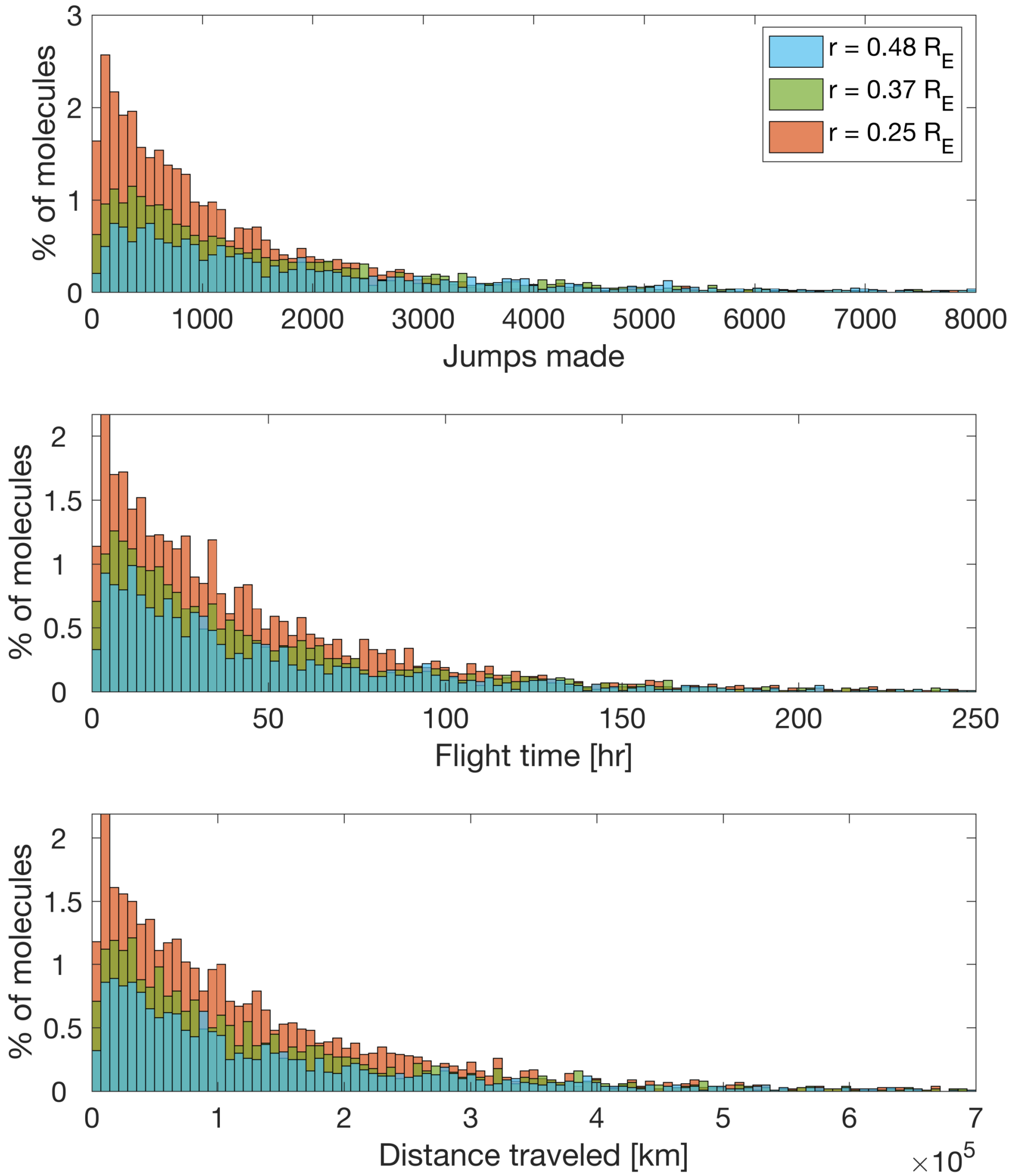

Figure 2.11: Cold-Trapped Molecules Statistics at 300 K. *Top*: Jumps made. *Middle*: Cumulative time spent airborne, or exospheric residence time. *Bottom*: Cumulative distance traveled.

In summation, a small planetoid size makes Jeans thermal escape likely while a large size makes photodissociation likely. Therefore, there is an ideal planet size that retains the most water molecules at the poles for a given incoming stellar flux and bulk density. Using our results, we find the radius and surface temperature combinations that cold-trapped the most water to produce Fig. 2.12; doing this for different bulk densities yields Fig. 2.13.

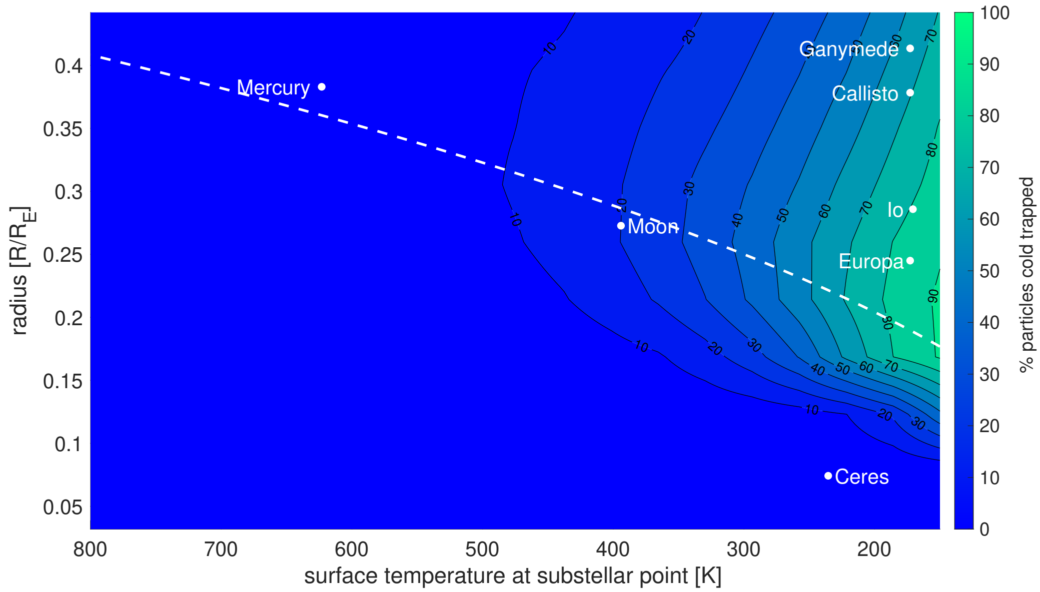

Figure 2.12: Orbital configuration where cold-trapping is most efficient. The dashed line represents where the most simulated molecules are cold trapped for a given maximum surface temperature. The set bulk density here is 3 g cm^{-3}.

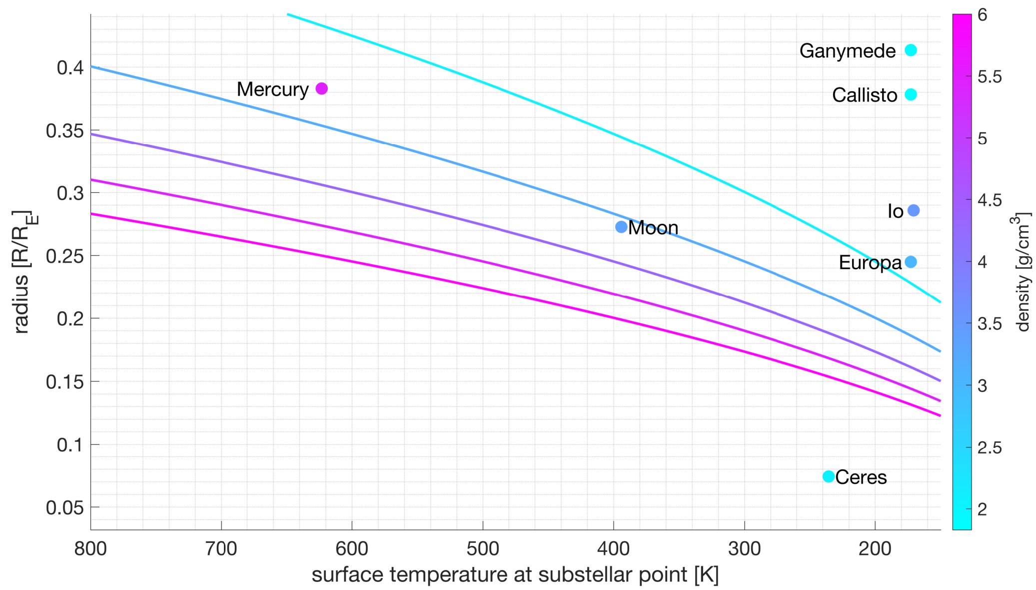

Figure 2.13: Ideal cold-trapping configuration. The lines show the best size and surface temperature for cold-trapping water in permanently shadowed regions at a specific bulk density.

We test the effects of varying the amount of PSRs by scaling the lunar PSR distribution, shown in Fig. 2.2; this produces Fig. 2.14. As seen in the figure where surface temperature and bulk density are fixed, the "ideal" radius that favours the most water cold-trapping is the same regardless of how much of the planet is permanently shadowed. Although higher PSR coverage does lead to more water molecules trapped, the effect is diminished when there is already a significant amount of PSRs. This effect is even more muted when the planet is either much bigger or smaller than the ideal cold-trapping size.

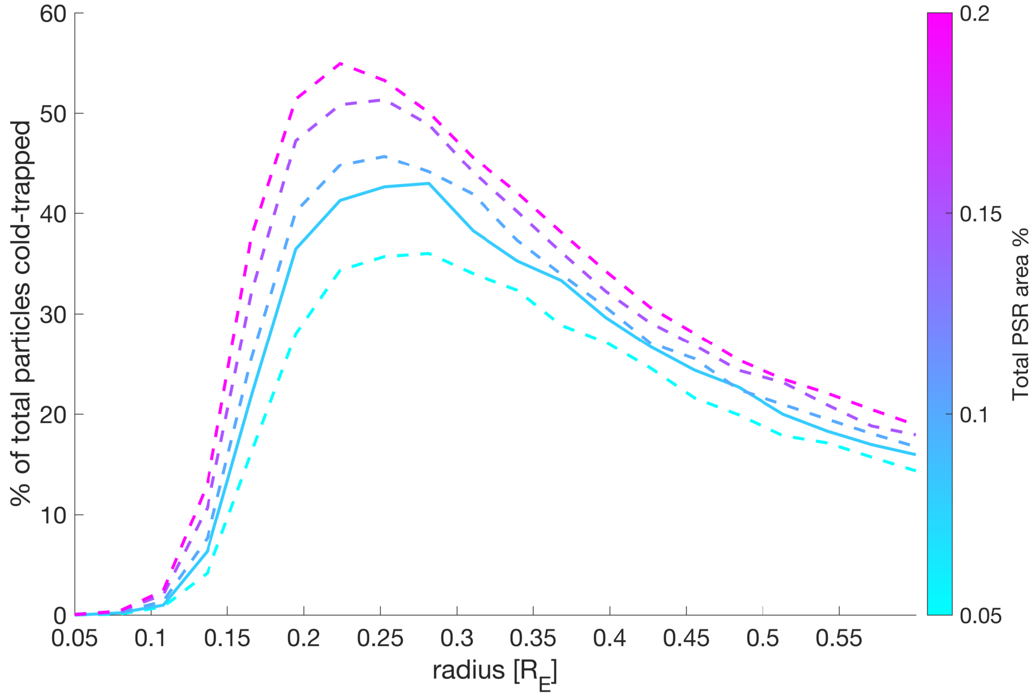

Figure 2.14: Cold-trapping for varying PSR coverage. The substellar surface temperature is fixed at 300 K as is the bulk density at 3 g cm^{-3}. We vary the total PSR coverage between 0.05% and 0.20%, represented by the dashed lines. The solid line is the Lunar PSR distribution where 0.08% of the Moon's surface lies in constant darkness.

2.4.2 Implications

Inside the Solar System

Our model provides very interesting insights about exospheric dynamics and water distribution within the solar system. If treated as bare rock moons, we would expect Europa and Io to cold-trap over 80% of sublimated water molecules. Likewise for Ganymede and Callisto, even though they are much larger than the ideal size for cold-trapping water, they are still efficient at trapping water molecules (70% tracers cold-trapped).

Although the Galilean moons mentioned above are favoured to accumulate a lot of water in our model, this depends on whether or not there is a collisional atmosphere. Atmospheric modelling and observations show a thin partial SO_2 atmosphere on Io (Ballester et al., 1994; Strobel & Wolven, 2001); this can significantly affect water migration. The other moons are also expected to have atmospheres full of O_2 that interact with water (Ganymede: Roth et al., 2021, Callisto: Mogan et al., 2021, Europa: Shematovich et al., 2005). However, our work shows that sublimated water is likely to be cold-trapped in PSRs before undergoing photolysis and this may significantly affect O_2 and H_2 abundances in the moons' atmospheres. For Ceres, we find that it is too small and most sublimated water molecules will be lost to space via Jeans thermal escape, similar to Steckloff et al. (2022); this explains the cometary properties of Ceres.

Mercury, unlike the Galilean moons, is very close to the Sun so most H_2O molecules in the exosphere will almost certainly undergo photodissociation; this agrees well with Steckloff et al. (2022). Even if Mercury becomes smaller (0.3 R_E) to ideally cold-trap water molecules in PSRs, the amount of molecules trapped would be less than 5%. Despite the small amount of water predicted to lie in PSRs on Mercury in our model, substantial ice deposits are observed on its surface (Deutsch, Neumann, & Head, 2017; Rubanenko, Venkatraman, & Paige, 2019). This could be caused by a temporary transient atmosphere blocking solar radiation (Prem et al., 2015), or from water-rich meteoroids that impact Mercury at high latitudes (Butler, 1997; Frantseva et al., 2022).

Testing the parameter space near the Moon gives a surprising insight. Referring to Fig. 2.13, the Moon is very close to the ideal cold-trapping configuration curve. This means that the Moon is essentially perfectly sized to maximize cold-trapping in PSRs given its composition and proximity to the Sun. This remains the case when we vary the total PSR coverage, as seen in Fig. 2.14. Despite this, the Moon is observed to have less water ice than Mercury hinting that another process may have impeded water transport on the Moon or that it may have undergone huge changes in obliquity and expose surface ices to sublimate.

Outside the Solar System

For outside the solar system, the results can be used to characterize general trends in exomoons and dwarf exoplanets. Small iron-core planets/moons (0.2-0.4 R_E) should be very efficient at cold-trapping water and therefore build significant water deposits at the poles. In the absence of a thin transient atmosphere, cold icy bodies similar to Europa or Io are expected to trap the majority of water in the exosphere in their PSRs. Although the results shown are for the Sun, the photolysis scales with stellar FUV flux and the photodissociation rate should be within an order of magnitude of what Crovisier (1989) calculated.

Even if we vary the photodissociation rate significantly, we do not expect the results to change qualitatively. The balancing point between the photolysis timescale and ballistic hopping timescale would simply be shifted to a new spot in the parameter space. Therefore, at a specific density, an ideal size exists to maximize water cold-trapping. These timescales are different for other volatiles and there also exists ideal conditions to cold-trap those molecules as well. With better understanding of exoplanet and exomoon population statistics, we can apply this work to gauge generally how volatiles like water, CO_2, or CH_4 might be distributed within star systems.

2.4.3 Caveats

Due to the computational work required to run the Monte Carlo simulation, we had to limit the scope of what can be parameterized. We could only test different radii, bulk densities, and received insolation. Any other physical properties such as obliquity and PSR distribution are based on the Moon which may not be widely applicable to other planetary bodies. We also neglect important aspects such as the role of regolith in absorbing and desorbing water molecules as well as the recombination of Hydrogen and Oxygen to return water back to the exosphere.

Each simulated scenario has the same amount of tracers, and therefore the same initial distribution of water on the surface. However, this is not the case for the solar system as there is a wide range of water available for exospheric transport on each planetary body. Therefore, we can only compare the relative cold-trapping rate and not the absolute amount of volatiles cold-trapped in the polar system. Still, if we treat our results as a relative baseline, we can infer which planetoids have sequestered an unusually large amount of water on their surfaces or which planetoids are abnormally deficient of water.

Meteor impacts that supply water are sporadic and can land anywhere on a planetoid; excited water molecules can start from anywhere. Therefore our cold-trapping results are rather conservative as we set the sublimated volatile to start near the equator. Exospheric water transport works that allow for a wider range of initial tracer location do show more volatiles being cold-trapped in PSRs (Butler, 1997).

2.5 Chapter Conclusions

Water distribution between various planetary bodies is an important aspect of habitability and human exploration. For many airless bodies within and outside the solar system, water is transported in the exosphere and may end up in permanently shadowed regions; over time, these regions may build up large reservoirs of water. To determine planetary properties that favour cold-trapping in PSRs, we produce a Monte Carlo model to simulate water molecules undergoing ballistic hops across the surface. Predictably, our results suggest minimal cold-trapping in PSRs for Mercury and a modest water abundance build up for the Moon, consistent with other similar numerical works. Ceres is too small and most sublimated water molecules are thermally lost to space. The Galilean moons, on the other hand, are expected to cold-trap most of the sublimated water molecules. However, each of these cases exhibits a thin collisional atmosphere on the dayside and our exospheric transport model no longer applies.

Examining the parameter space where cold-trapping is efficient yields surprising results. Orbital configuration and physical properties that favour large ballistic hops are seen to increase cold-trapping while small ballistic hops tend to lead to more photodissociation. Therefore, given a certain incoming instellation and bulk density, there is an ideal size that maximizes how much water gets cold-trapped. Coincidentally, our lunar neighbour is indeed perfectly sized for water to be cold-trapped in PSRs. This ideal size stays fairly constant even if we change the total PSR coverage significantly. Applying these findings to exoplanet population studies can help to infer water abundances on possible exoplanets and exomoons yet to be discovered.

3 | Modeling Lava Planets: I

Chapter Summary

The recently discovered exoplanet K2-141b is revealed to be a superEarth closely orbiting a K-type star. Its extreme orbital configuration gives it a distinctly high signal-to-noise ratio. K2-141b is therefore an ideal target for probing into terrestrial dynamics, especially atmospheric processes. Being a tidally locked lava planet, K2-141b's atmosphere is constrained on the dayside which requires a more specialized approach for modelling. In this chapter, we used surface boundary layer model, originally developed for icy worlds, to simulate the atmosphere on K2-141b. We tested 3 main atmospheric constituents and find that very volatile components like Na may be not be replenishable on the dayside surface. SiO, on the other hand, should be abundant and volatile enough to make it a substantial part of K2-141b's atmosphere. However, SiO's spectral properties require implementing radiative transfer in the model, which will be discussed in the next chapter.

Section 3.1 begins with the discovery of K2-141b (3.1.1) and the background on

lava planets (3.1.2). Section 3.2 and 3.3 describe the surface boundary layer model and the magma ocean respectively. The results are found in Sec. 3.4 where subsection 3.4.1 is for the atmosphere and 3.4.2 is for the magma ocean. We discuss our model's limitations in Sec. 3.5. Finally, the chapter conclusions can be found in Sec. 3.6. This chapter includes work from Agnibha Banerjee who provided the calculations from Kopal (1954). John Moores and Nicolas Cowan helped with feedback for the publication, Nguyen et al. (2020).

3.1 Background

3.1.1 Discovery of K2-141b

Initial exoplanet detections relied on the radial velocity method. This involves measuring the star's spectral shift as it is tugged by nearby planets' gravitational pull. Large exoplanets that orbit closely to their stars can induce a significant enough shift and be easily characterized. And so, early exoplanets discoveries are often highly irradiated "Hot Jupiters". However, with incremental progress in instrumentation on both ground-based and space-based observatories, we can now detect much smaller planets.

The Kepler program was designed to survey the sky for planets of all size and was prolific in doing so: the mission has led over two thousands confirmed exoplanets (Han et al., 2014). Although technical difficulties hampered Kepler's original scope, the subsequent K2 campaigns were still instrumental in detecting and characterizing exoplanets. During K2's campaign 12 between December 2016 and March 2017, an exoplanet was discovered called K2-141b (Barragán et al., 2018).

After the K2 discovery, follow up high-precision Doppler observations of K2-141b were conducted. Observations were made by the Nordic Optical Telescope at the Roque de los Muchachos Observatory and the ESO-3.6m telescope at La Silla observatory. The cumulative data analyzed by Barragán et al. (2018) and Malavolta et al. (2018) reveal that K2-141b is a rocky planet 1.5 times the radius of Earth, and 5 times its weight. The orbit around the star, K2-141, is extremely tight (0.007 AU) and fast (6.7 hr period).

K2-141b's extreme orbital configuration allows for unprecedented precision of observational data for planets of its size, at least at the time of discovery. The prospect of observing the planet in greater detail makes K2-141b an enticing target for Spitzer (Kreidberg et al., 2018) and JWST (Dang et al., 2021). Therefore, there is an immediate need to characterize the planet, especially if there is an atmosphere. Being so irradiated, K2-141b's rocky surface should be molten, earning its place among "lava planets".

3.1.2 Lava Planets

Lava planets are rocky exoplanets that orbit close to their star. Being tidally-locked into synchronous rotation, these planets have large surface temperature contrasts between the permanent dayside and nightside. On the dayside, the stellar flux is intense enough to vaporize rocks, generating a thin atmosphere of mineral vapour (Schaefer & Fegley, 2009). On the nightside, the temperature drops and the atmosphere may collapse back onto the surface as has been predicted for volatiles on M-Earths (Wordsworth, 2015). In order to qualify as a lava planet, a world must have a density consistent with rocky bulk composition, and the surface temperature must exceed the solidus for silicates; examples include CoRoT-7b (Léger et al., 2011) and Kepler-10b (Batalha et al., 2011).

The atmosphere on a lava planet is in vapour equilibrium with the magma ocean, so atmospheric and interior dynamics are intertwined (Kite et al., 2016). Therefore, atmospheric detection and characterization of a lava planet may reveal the bulk composition of its rocky mantle. However, the collisional atmospheric regime on the dayside and non-collisional exospheric regime on the nightside makes modelling difficult, extremely so for global general circulation models.

Dynamics of the partial atmospheres on lava planets are similar to that of Callisto (Mogan et al., 2021), Io (Tsang et al., 2016) or Pluto (Gladstone & Young, 2019). As such, icy bodies in the solar system are counter-intuitively analogous to lava planets and studying one can help to understand the other. Atmospheric modelling for partial atmospheres often uses surface boundary layer approximations and has been applied to Io (Ingersoll, Summers, & Schlipf, 1985) and hypothetical ice ball or ocean-world exoplanets (Ding & Pierrehumbert, 2018).

Following the work of Castan and Menou (2011), we use the surface boundary layer model of Ingersoll, Summers, and Schlipf (1985) to produce initial atmospheric characterizations of the lava planet K2-141b. We improve upon the model by implementing more realistic surface temperatures, as well as explore the dynamics of the magma ocean. This will work towards the goal of observing terrestrial atmospheres outside the solar system, an important milestone for exoplanetary exploration.

3.2 The Surface Boundary Layer

3.2.1 Assumptions

As a short-period planet on a circular orbit, K2-141b is expected to be tidally locked into synchronous rotation, leading to a permanent dayside and nightside. Not only does this introduce symmetry in how the planet is illuminated, it also leads to equilibrium dynamics (Schaefer & Fegley, 2009). The atmosphere of a lava planet originates from the sublimation/evaporation of the surface and the flow is maintained by the pressure gradient between the nightside and dayside. The solutions are therefore dependent on the surface temperature and solely a function of the angular distance from the sub-solar point (θ_{ss}).

We assume a hydrostatically bound “thin" atmosphere with negligible absorption of radiation. Although radiative transfer simulations of mineral-vapour atmospheres suggest that this is not the case (Ito et al., 2015), it is a useful first approximation and makes the problem tractable. We also neglect Coriolis forces to keep the problem one-dimensional although our estimated Rossby number of 10^{-1} suggests that Coriolis forces may be stronger on K2-141b than on other lava planets (Castan & Menou, 2011). Lastly, we assume that the atmosphere is turbulent and well-mixed, leading the vertically-uniform wind velocity, V_*. Other state variables, pressure P_* and temperature T_*, are values calculated at the top of the boundary layer (Ingersoll, Summers, & Schlipf, 1985).

We compute the surface temperature ahead of time because, as stated above, we assume it is unaffected by the atmosphere. The atmosphere is idealized to be pure and condensible because of the model's limitations. Likely composition and abundances modelled by Schaefer and Fegley (2009) are shown in Appendix B.1, Fig. B.1. We first consider a pure Na atmosphere, neglecting dissociation processes that unbind Na from other molecules as is done by previous studies of lava planets (e.g., Castan and Menou, 2011; Kite et al., 2016). Na is relatively scarce in a rocky planet's crust (Schaefer & Fegley, 2009) whereas SiO_2 is the dominant constituent. Therefore, we also run the model using SiO in the same spirit as Na. Since gas-phase SiO will likely condense as SiO_2 and may recombine with oxygen even before condensing, we finally use a pure SiO_2 atmosphere. The model was derived from the shallow-water equations by Ingersoll, Summers, and Schlipf (1985) and adapted by Castan and Menou (2011) for exoplanets. It describes the conservation of mass (Eq. 3.2), energy (Eq. 3.5), and momentum (Eq. 3.16). Parameters for the model can be found in Appendix B.2.

3.2.2 The System of Equations

Conservation of Mass

To determine the conservation of mass, we initially have:

$$\partial_t h + \nabla \cdot (\rho h v) = 0, \tag{3.1}$$

where ρ is the fluid density, h is the fluid's column thickness, and v is the horizontal flow. Applying this equation to our case requires time invariance, $\partial_t h = 0$, hydrostatic equilibrium, $h = P/(\rho g)$, and a source/sink to account for evaporation/condensation such that the right hand side of Equation (2) is no longer 0 but some mass flux rate, E [molecules s^{-1} m^{-2}]. The final step is to change to spherical coordinates which gives our mass conservation equation:

$$\frac{1}{r\ \sin(\theta)} \frac{d}{d\theta} \left(\frac{V_*\ P_*\ \sin(\theta)}{g} \right) = m\ E, \tag{3.2}$$

where r is the planet's radius (9.62×10^6 m), m is the mass per molecule, and g is the surface gravity (21.8 m/s^2). E is the mass flux and is calculated by the evaporation/sublimation of the surface through the difference between the saturated vapour pressure and the atmospheric pressure:

$$E = \frac{(P_v - P_*) v_c}{\sqrt{2\pi}\ m\ R\ T_s}. \tag{3.3}$$

The kinetic speed of sublimation/evaporation is denoted by v_c, which for any species sublimating into a near vacuum, is $\sqrt{kT_s/m}$, where k is the Boltzmann's constant.

Conservation of Energy

The general equation that describes the fluid column's kinetic energy ($v^2/2$) and internal heat energy ($C_\mathrm{p}T$) is:

$$\nabla \cdot \left(\rho h v \left(\frac{v^2}{2} + C_p T\right)\right) = Q, \tag{3.4}$$

where C_P is the heat capacity. Energy is conserved if the vertically integrated kinetic energy flux, internal heat energy, gravitational energy, and work done via adiabatic expansion is balanced out by energy exchanged with the surface, Q [W m^{-2}]. The sum of the internal heat, gravity, and work terms becomes the enthalpy per unit mass at the top of the boundary layer: $C_p T_*$. Considering 1D steady state flow in spherical coordinates yields the equation for energy conservation:

$$\frac{1}{r\ \sin(\theta)} \frac{d}{d\theta}\left(\frac{(V_*^2/2 +\ C_p\ T_*)V_*\ P_*\ \sin(\theta)}{g}\right) = Q. \tag{3.5}$$

The energy flux Q, a combination of enthalpy at the surface and top of boundary layer as well as kinetic energy, is calculated by the following:

$$Q = \rho_s(w_s\ C_p\ T_s - w_a\ (V_*^2/2 + C_p\ T_*)), \tag{3.6}$$

where w_s and w_a are transfer velocities defined by Ingersoll, Summers, and Schlipf, 1985 that further parameterize energy contribution from the surface and atmosphere respectively. Both w_s and w_a are evaluated from Equations 3.7 to 3.10, where Eq. 3.7 and 3.8 are used when there is net deposition (E <0) and Eq. 3.9 and 3.10 are for net evaporation (E >0):

$$w_a = \frac{V_e^2 - 2V_d\ V_e + 2V_d^2}{-V_e + 2V_d}\ , E < 0 \tag{3.7}$$

$$w_s = \frac{2V_d^2}{-V_e + 2V_d}\ , E < 0 \tag{3.8}$$

$$w_a = \frac{2V_d^2}{V_e + 2V_d}\ , E \geq 0 \tag{3.9}$$

$$w_s = \frac{V_e^2 - 2V_d\ V_e + 2V_d^2}{V_e + 2V_d}\ , E \geq 0. \tag{3.10}$$

The transfer coefficients are dependent on two velocity values: V_e and V_d. V_e represents the mean flow and is calculated by: $V_e = m\ E/\rho_s$. V_d represents the effects of eddies which is calculated by: $V_d = V_{\mathrm{f}}^2/V$ where V_{f} is the friction velocity; this must be calculated iteratively from:

$$V_{\mathrm{f},n+1} = \frac{V}{2.5\ log(9\ V_{\mathrm{f},n}\ H\ \rho_s/(2\eta))} \tag{3.11}$$

where η is the dynamic viscosity whose calculations can be found in Appendix B.2 and H is the atmospheric scale height:

$$H = \frac{kT}{mg}. \tag{3.12}$$

Conservation of Momentum

Momentum is the final component for solving the model, which is affected by pressure gradient forces and surface drag τ [kg m^{-1} s^{-2}]. This relation has the general steady-state form:

$$\nabla \cdot (\rho h v^2) = -\nabla \int_z P + \tau. \tag{3.13}$$

To solve the momentum equation, P is vertically integrated with height by using the pressure and temperature at the top of the boundary layer, P_* and T_* respectively:

$$\int_0^\infty P dz = \int_0^{P_*} \frac{\Phi}{g} dP = \frac{C_p}{g} \int_0^{P_*} (T_* - T) dP, \tag{3.14}$$

where Φ is the geopotential. The change in Φ is the work done as the vaporized particles ascend from the surface to the top of the boundary layer; this can be expressed as $C_p(T_* - T)$. In order to close the problem, we must assume a vertical temperature profile. For an adiabatic profile, we have $T = T_*(P/P_*)^{R/C_p}$ where R is the gas constant. Substituting this into the integral in Eq. 3.14 yields:

$$\frac{C_p}{g}\left(T_*P_* - T_*P_*\left(\frac{1}{R/C_p+1}\right)\right) = \frac{C_pT_*P_*\beta}{g}, \tag{3.15}$$

where $\beta = R/(R+C_p)$ for an adiabatic profile. Note that we can arbitrarily change β to parameterize different vertical temperature profiles, which will be useful for later chapters. More details on β can be found in B.4.1. Substituting the mass for a product of V, P and g, integrating ∇P vertically, collecting like terms, and changing to spherical coordinates yields the momentum conservation equation:

$$\frac{1}{r\ \sin(\theta)}\frac{d}{d\theta}\left(\frac{(V_*^2 + \beta\ C_p\ T_*)P_*\ \sin(\theta)}{g}\right) = \frac{\beta\ C_p\ T_*\ P_*}{g\ r\ \tan(\theta)} + \tau. \tag{3.16}$$

The momentum flux τ is calculated by the following:

$$\tau = \rho_s(-V_*\ w_a), \tag{3.17}$$

There is a negative sign to denote that this force always acts against the flow. The vapour density, ρ is determined via the ideal gas law. For convenience, Table B.1 contains a brief description of all the parameters featured above.

3.2.3 Numerically Solving the Model

The state variables at the surface layer's boundary, (P_*, V_*, T_*), can be calculated given initial values at the boundary (substellar and antistellar point) by integration of fluxes in the right-hand side of Eq. 3.2, 3.5, and 3.16. If we treat these equation as a single equation, we get:

$$\frac{d}{d\theta}(f_{\text{state}}(\theta)) = f_{\text{fluxes}}(\theta) \tag{3.18}$$

The state variable can be calculated at the next spatial step (the change in angular distance $\Delta\theta$) through finite differences:

$$f_{\text{state}}(\theta + \Delta\theta) = f_{\text{fluxes}}(\theta) \times \Delta\theta + f_{\text{state}}(\theta) \tag{3.19}$$

We solve for a solution through finite-differences using a Runge-Kutta scheme to the second order accuracy. After acquiring f_{state}, the state variables can be solved arithmetically but due to the quadratic nature of V in the equations, two branches can be extracted corresponding to the flow being either subsonic or supersonic. Although, a higher order scheme could remedy the sensitivity of modelling fluid transitioning from subsonic to supersonic flow, the calculations to extract the state variables from Eq. 3.2, 3.5, and 3.16 would take longer. Therefore, we elect to employ other schemes to control the instability inherent in the model, as described below.

We use the shooting method where we guess the initial $P(\theta = 0)$ and find a solution that fits the boundary conditions: V is 0 at $\theta = 0°$ and $\theta = 180°$, $T(\theta = 0) = T_{ss}$. The instability of the non-linear system of equations can lead to solutions either exponentially expanding or decaying. The goal, therefore, is to solve for a solution that exists in between the bounds of solutions that blew up (upper) or decayed to 0 (lower) exponentially. Conditions that define whenever a solution expands or decays exponentially are explicitly described by Ingersoll, Summers, and Schlipf (1985).

Solving for velocity will yield two solutions, one for subsonic flow and the other for supersonic flow. Getting to the critical point where the flow transition between different subsonic and supersonic regimes can be difficult. Therefore, we dynamically increase the spatial resolution whenever the upper bound and lower bound solution start to diverge past a set parameter. A solution close to the "true" solution (which lies in between the upper and lower bound) will approach Mach 1 more reliably, after which we extrapolate the flow into the supersonic regime. This extrapolation process is done by linearizing the state variables with respect to θ until Mach 1 is achieved. The flow is then calculated using the supersonic branch of the solutions.

3.3 Surface Conditions and the Magma Ocean

To find the surface tempature, we adopt planetary parameters from Malavolta et al. (2018) and Barragán et al. (2018) where the substellar equilibrium temperature according to Malavolta et al. (2018) is 3038 $\pm$ 64 K; a nice rounded value of 3000 K is consistent within this range, which we adopt for the rest of the study. Previous estimates of the surface temperature (T_s) by Castan and Menou (2011) and Kite et al. (2016) accounted for the zero-albedo local radiative equilibrium temperature and geothermal heating:

$$T_s = \begin{cases} (T_{ss} - T_{as}) \cos^{1/4}(\theta) + T_{as} & \text{for } \theta \le 90^{\circ}, \\ \\ T_{as} & \text{for } \theta > 90^{\circ}, \end{cases} \tag{3.20}$$

where T_{ss} and T_{as} are the temperature at the subsolar and antisolar point respectively and θ is the angular distance from the subsolar point. The $\cos^{1/4}\theta$ expression is only valid in the limit of a distant star, $R_*/a << 1$. K2-141b is located close enough to its star, however, that the the star subtends 132 degrees on the sky as seen from the planet and the surface can still be illuminated well past $\theta = 90^{\circ}$. Here, we employ a more accurate analytic expression for the surface temperature originally developed for binary star systems (Kopal, 1954). The surface temperature of K2-141b calculated using these two schemes is shown in Fig. 3.3. Beyond $\theta \simeq 115^{\circ}$, the illumination flux is so low that the temperature is mainly dependent on a geothermal flux, which we neglect. Our model will show that the atmosphere fully condenses out well before this point.

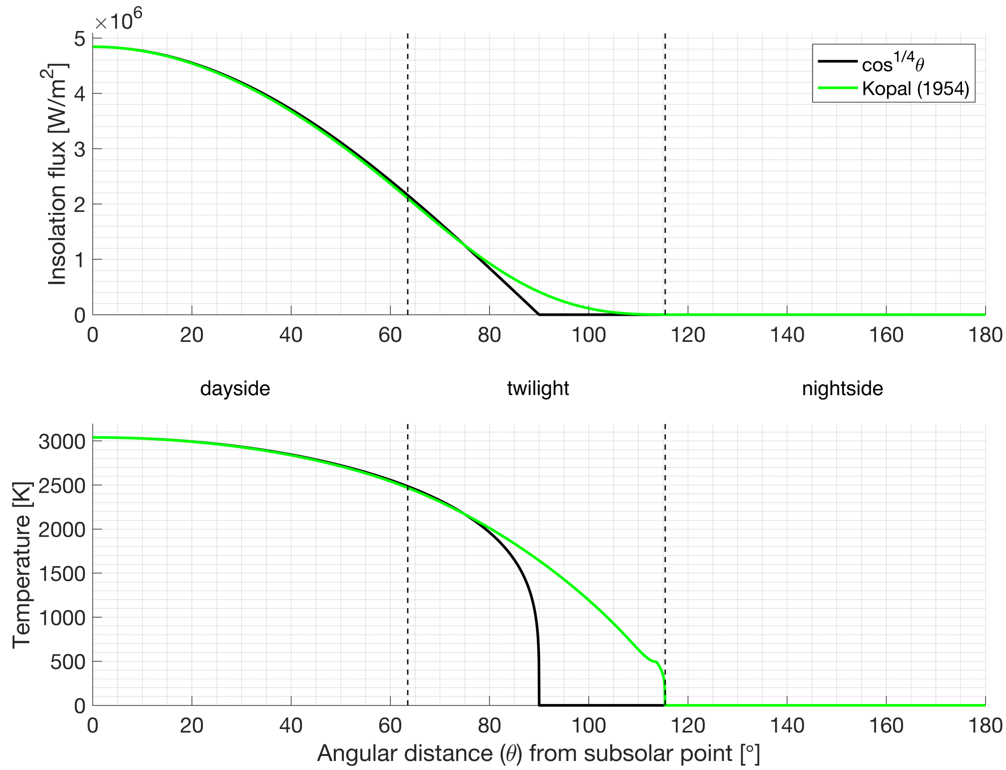

Figure 3.1: Top: the illumination received by K2-141b as a function of distance from the sub-stellar point. Bottom: equilibrium temperature. In both panels, the black line shows the $\cos^{1/4}\theta$ flux dependence adopted by previous researchers while the green line shows more accurate formulation that accounts for the large angular size of the star as seen from the planet.

With the surface temperature now calculated, we can infer physical properties of the magma ocean by making a few assumptions and simplifications for two cases. For the first case: silicate materials dominate the composition of rocky planets (Schaefer & Fegley, 2009) and K2-141b's bulk density is comparable to Earth (Malavolta et al., 2018), so we assume that K2-141b's crust is entirely silica (SiO_2). We further assume that the temperature is vertically constant below the surface for the top 150 km. We neglect geothermal heating, which is reasonable if the ocean is relatively shallow and well mixed.

We determine the magma ocean depth assuming a constant subsurface temperature profile, appropriate surface gravity, the density of SiO_2 (2650 kg/m^3), and the phase diagram shown in Fig. 3.2 (Swamy et al., 1994) in the appendix. The relation between pressure and temperature for the phase change is not smooth as it relates to the crystallization of SiO_2. The most prominent anomaly can be seen at low pressure ($< 1 \times 10^8$ Pa) where the transition from liquid to solid (cristobalite) is almost entirely dependent on temperature ($\sim 2000K$). Using these data, we calculate the depth of magma ocean column as a function of the surface temperature at the top of the column, also shown in Fig. 3.2.

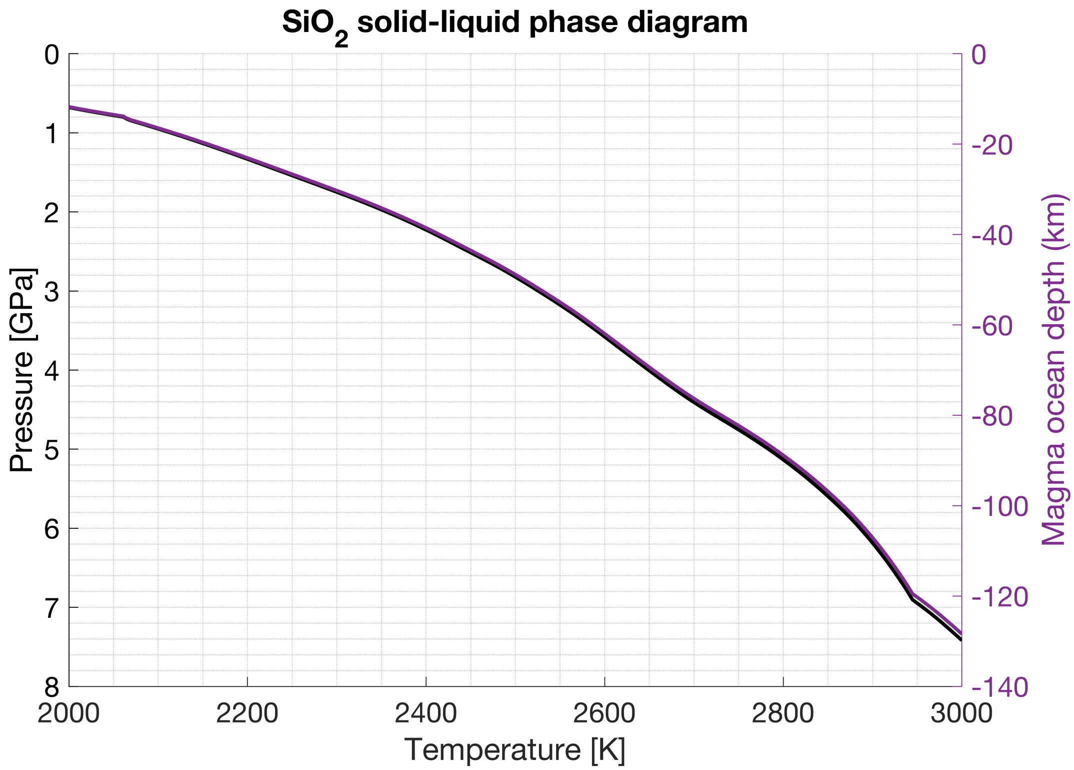

Figure 3.2: Phase diagram (black) and magma ocean depth (purple). Left axis shows the pressure while the right shows the depth at which the phase will change between solid and liquid given the temperature and pressure. The Inflection points reflect transitioning between different SiO_2 crystal structures which are, in increasing pressure: cristobalite, β-quartz, coesite, and stishovite (Swamy et al., 1994).

Ultimately, considering the composition of the crust, we expect the evaporation of the magma ocean to contain SiO and SiO_2. We test for these species as well as Na, since it is very volatile and commonly used for Lava planets. We also inspect the effects of atmospheric flow on the oceanic flow, a first for studies of this type.

3.4 Preliminary Results

3.4.1 The Atmosphere

We used the model described in Section 3.2 to determine the steady-state flow of a pure Na, SiO, and SiO_2 atmosphere for lava planet K2-141b. Atmospheric pressure, wind velocity, and temperature, at the layer's boundary for the three cases are shown in Fig. 3.3. Na is the most volatile molecule, making the Na atmosphere the thickest of the three with the maximum pressure at the substellar point of 13.8 kPa. The Na atmosphere fully condenses out at $\theta = 102°$ where wind speed can reach up to 2.3 km/s (Mach 30). The atmospheric temperature of Na can drop to near zero before fully collapsing.

SiO is not as volatile as Na making the SiO atmosphere thinner with a maximum pressure of 5.25 kPa. The wind accelerates slightly faster than the Na case with velocities reaching up to 2.2 km/s and the atmosphere condenses out at $\theta = 92°$. The temperature also drops slightly faster. Running the model for SiO_2 produces the thinnest atmosphere with a maximum pressure of 240 Pa and collapses at $\theta = 89°$. The wind is slower with a maximum speed of 1.75 km/s but the SiO_2 atmosphere is much warmer as the temperature remains above 1500 K.

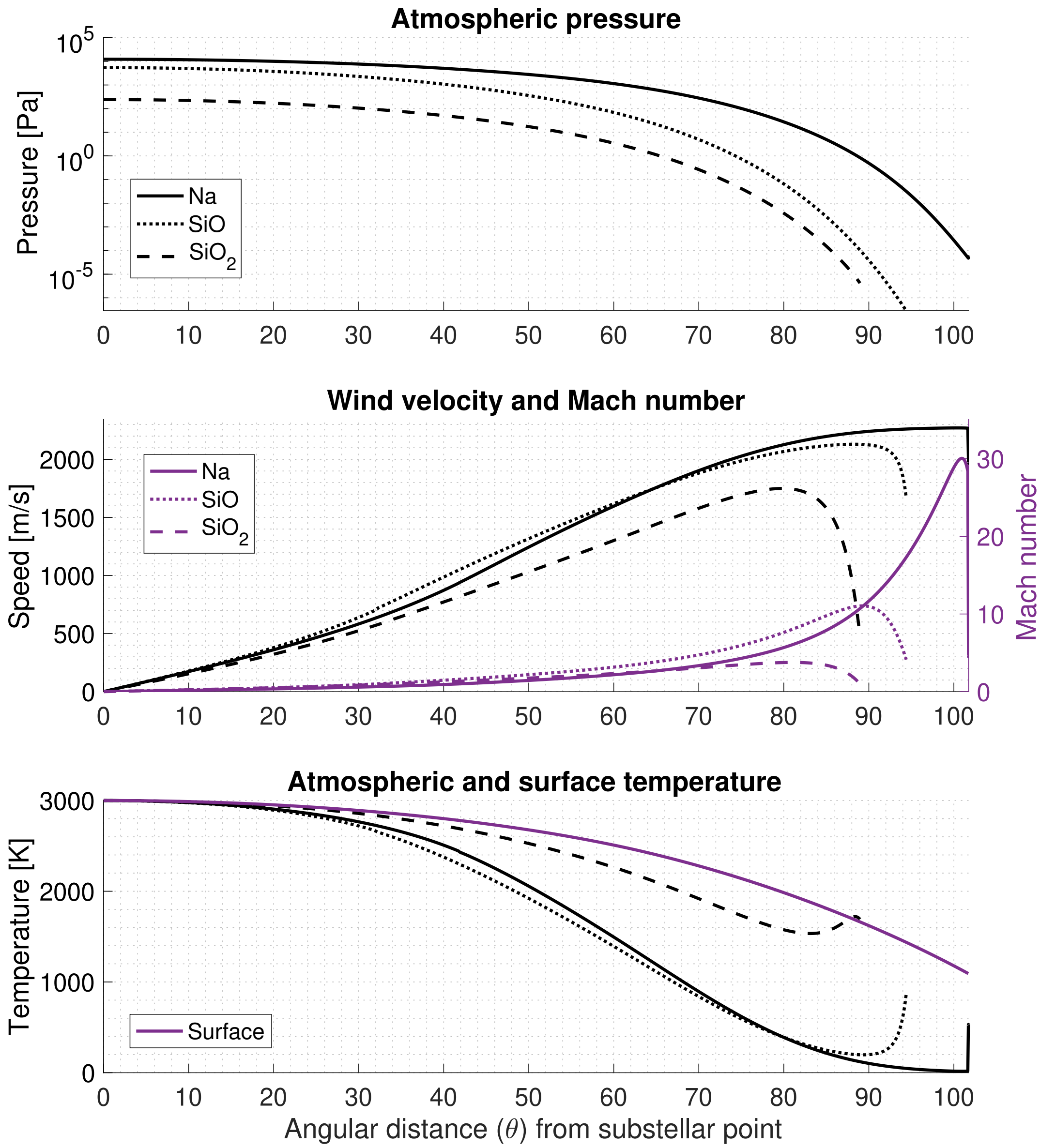

Figure 3.3: Top panel: atmospheric boundary-layer pressure for a pure sodium (Na), silicon monoxide (SiO), and silica (SiO_2) atmosphere. Middle panel: wind velocity (left/black) and mach number (right/purple). Bottom panel: atmospheric and surface temperatures (solid purple line).

With the pressure and temperature determined, we can further characterize the atmosphere. The Knudsen number can help us infer where the homosphere and heterosphere are. The homopause is where atmospheric composition starts to stratify as the collisions between molecules become less and less. Here, the molecular mean free path is on the same scale as the atmospheric scale height.

The molecular mean free path is calculated by: $kT/(\sqrt{2}\pi\sigma_d^2 P)$, where σ_d is the molecule's kinetic diameter, which for simple diatomic molecules, should be on the Angstrom scale (Mehio, Dai, & Jiang, 2014); P is the pressure. Using the scale height, H, we can determine the pressure level for which the Knudsen number is approximately 1. This exercise leads to a pressure on the scale of 10^{-6} Pa for an Na, SiO, and SiO_2 atmosphere.

For a surface pressure of $\sim 10^3$ Pa, 10^{-6} Pa is about 20 scale height up. However, the pressure drops significantly as you move away from the substellar point. And so, at large θ, the homopause can drop to within a few scale heights. The temperature becomes colder which makes the scale height smaller. Because the atmosphere is non-global, there comes a point where the the homopause meets the surface. The atmosphere is too thin and continuous free flow regime no longer applies; from that point on, exospheric dynamics come into play.

3.4.2 The magma ocean

To maintain steady-state atmospheric flow, material must be transported back to the sub-stellar region along the surface, most likely through currents in the magma ocean.

Horizontal mass transport is determined by calculating the cumulative mass that has evaporated and subsequently condensed. Therefore, the atmospheric mass transport (M_T) at some θ is given by:

$$M_T(\theta) = \int_0^\theta mE(\theta)d\theta. \tag{3.21}$$

The ocean return flow, v_o, that balances the atmospheric mass transport is therefore calculated via:

$$v_o(\theta) = M_T(\theta)/(\rho\ A(\theta)), \tag{3.22}$$

where ρ is the density of the magma ocean: 2650 kg/m^3 for SiO_2 or 2270 kg/m^3 for Na_2O (Na likely exists as Na_2O; Miguel et al., 2011). $A(\theta)$ is the cross-sectional area of the magma ocean given the magma ocean depth (estimated in section 2.1 and shown in Fig. 3.2). Eqs. 3.21 and 3.22 predict the ocean velocity without accounting for the dissociation of oxygen. This approximation may be fine for the SiO_2 atmosphere, but not for the SiO and Na scenarios. To account for the oxygen dissociated from SiO_2 or Na_2O, we simply scale the m value in Eq. 3.21 to conserve the mass of oxygen during the evaporation and condensation processes: scaling factor $= (1 + m_O/m_{SiO})$ for SiO and $(1 + 0.5 \times m_O/m_{Na})$ for Na.

As the magma is predominantly SiO_2, the ocean circulation is dictated by our SiO atmosphere (recall that SiO has a much greater vapour pressure than SiO_2). These calculations yield a maximum magma ocean return flow of 2-3$\times10^{-4}$ m/s, very slow compared to ocean circulation on Earth. The evaporation rate and inferred ocean velocities are shown as Fig. 3.4.

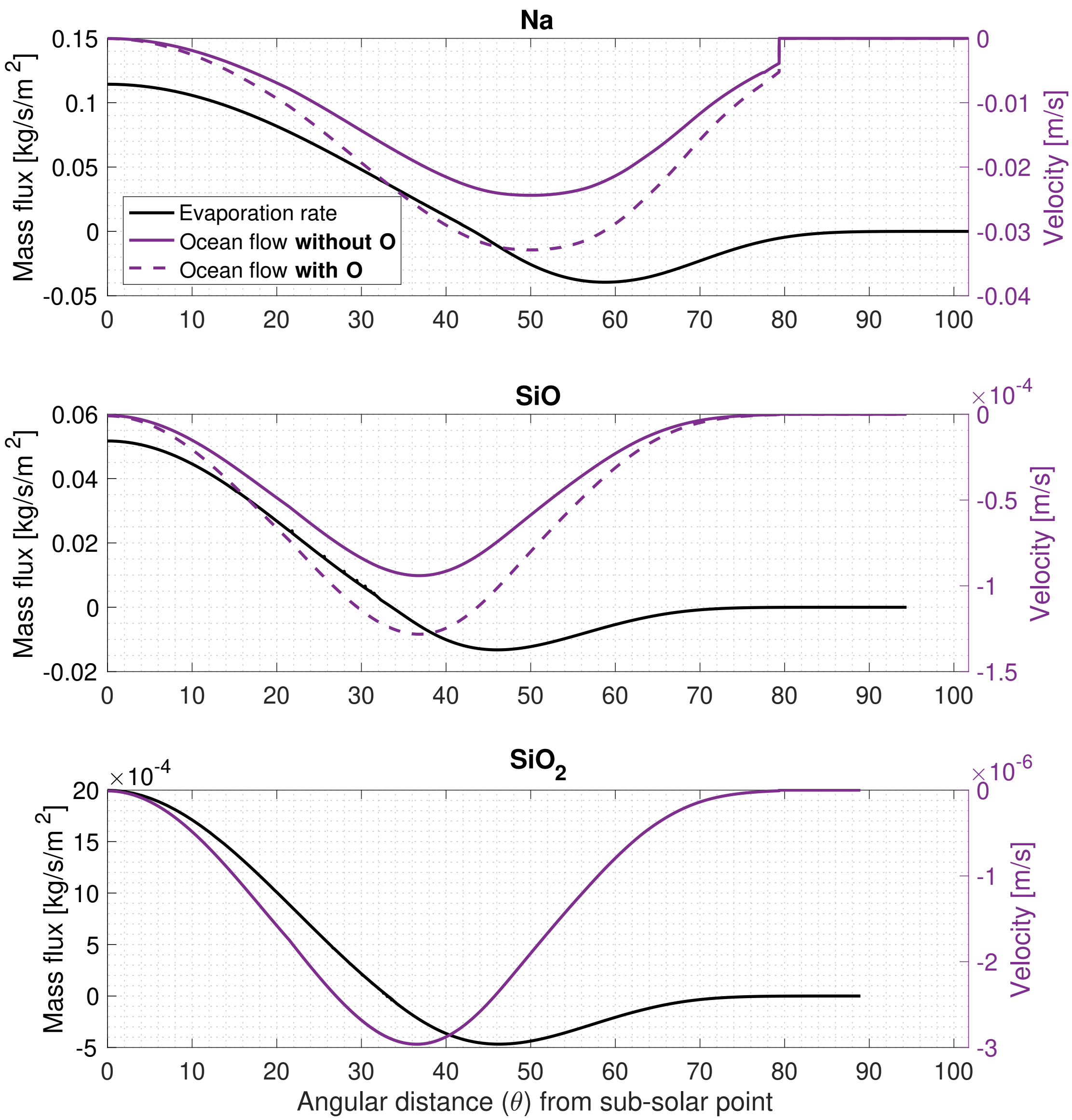

Figure 3.4: Left/black: evaporation rate per square metre (negative numbers denote condensation). Right/purple: velocity of magma ocean return flow. Negative values denote mass flow towards the subsolar point (in the negative θ direction). Solid purple lines denote calculations neglecting the transport of oxygen while dashed lines includes oxygen to maintain mass balance.

If we assume a SiO_2 to Na ratio similar to that of a Bulk Silicate Earth (where

Na_2O accounts for 0.7% of the BSE), then Na accounts for 1.52% by mass of our idealized crust (Miguel et al., 2011). Applying the same ratio to the magma ocean, we calculate the ocean circulation required to maintain mass balance for Na which resulted in a maximum velocity of 2-3 cm/s, two orders of magnitude faster than the expected circulation in the magma ocean. While not much mass condenses beyond the magma ocean for our SiO and SiO_2 cases, a significant amount of Na is deposited onto solid ground. Here, material can no longer be transported by ocean circulation, but rather by solid flow akin to glaciers flowing into the ocean on Earth.

Our calculated return flow of SiO_2 through the magma ocean is slow (10^{-4} m/s), so mass balance can be easily achieved. This supports a steady-state silicate flow whereas the volatile Na atmosphere would be limited by the return flow through the magma ocean. Although K2-141b is an especially good target for atmospheric observation, our results regarding atmospheric dynamics, replenishment via the magma ocean, and transit geometry may apply to other lava planets.

3.5 Model Limitations

Our proposed pure or nearly pure SiO_2 magma ocean is likely affected by interior dynamics which we neglect. The calculated ocean flow only accounts for the bulk mass transport along θ to balance the evaporation and condensation rates. We also neglect Coriolis forces despite the fast rotation of K2-141b. Qualitatively, Coriolis force would deflect the wind en route to the cold nightside and the mass transport of both the atmosphere and the ocean would be constrained to a smaller area, presumably near the equator. Despite this, there should still be net mass transport in the atmosphere as the evaporated volatiles would still move from an area of high vapour pressure to areas of low vapour pressure. This also applies to the magma ocean as mass would need to recirculate to maintain net mass balance between the surface and atmosphere.

If atmospheric dynamics were dictated by both vapour pressure gradients and Coriolis forces, then it would lead to the formation of Rossby waves and possibly weather systems. The ocean flow is slower than the atmosphere, so it would be even more affected by Coriolis forces. Ultimately, a Global Circulation Model (GCM) is required to accurately infer atmospheric dynamics that arise from the planet's rotation. However, this is difficult for a lava planet because the GCM would need to handle supersonic winds in an atmosphere that fully collapses far away from the sub-solar point.

Another approximation is the fixed surface temperature which allowed for the energy of the surface and atmosphere to be decoupled. This adds significant stability to the model especially as supersonic flow is guaranteed. Coupling the energy budgets of the surface and atmosphere in post-processing can help to estimate the actual surface temperature. We calculated how much energy it would take to heat up the advected ocean mass to the equilibrium surface temperature from the model's results. This is done by taking the bulk transported mass per θ and multiplying it with the heat capacity and the temperature gradient. This energy peaks at 10^2 W/m^2 which is minuscule compared to other energy contributions.

Latent heat, may be a more significant source of energy for the surface. But the maximum latent heat generation rate per square metre produced by the evaporation of silica ($\sim 10^2$ W/m^2), silicon monoxide, and sodium (both $\sim 10^5$ W/m^2) are at least an order of magnitude smaller than the instellation ($\sim 10^6$ W/m^2). This suggests that latent heat would barely affect the surface temperature, in agreement with Castan and Menou (2011) and Kite et al. (2016). It remains to be seen whether the energy of dissociation (e.g., SiO_2 -> SiO + O) is as important for lava planets as it has proven to be for ultra hot Jupiters (Bell & Cowan, 2018; Mansfield et al., 2020; Tan & Komacek, 2019).

Another important limitation with our model is the lack of consideration for radiative processes in the atmosphere. Although the work of Ito et al. (2015) suggests that there should be strong radiation absorption in the upper atmosphere, their results are sensitive to specific atmospheric compositions, stellar spectra in the ultraviolet, and atomic/molecular line lists, all of which are difficult to know for exoplanets.

The composition of the atmosphere is also very idealized as we ignore chemical processes where SiO_2 or Na_2O dissociate to form O and O_2, both of which are more volatile than SiO_2 but less volatile than Na. This has huge implications on transit spectroscopy as each molecule has its own distinct spectral features. Even in our idealized case where we focused on evaporation and condensation at great length, we neglected macro-scale meteorological processes, chiefly cloud formation. This also greatly affects observations as clouds can trap heat via longwave radiation absorption but reflect shortwave radiation.

3.6 Chapter Conclusions

The recently discovered exoplanet K2-141b is a great target for observing terrestrial atmosphere because of its high signal-to-noise ratio. Being so close to its star, the planet may outgas silicate material leading to a thin mineral vapour atmosphere on the dayside. However, the dynamics of a partial atmosphere is difficult to model and so we relied on surface boundary layer approximations that are commonly used for icy bodies. We tested different gas constituents (Na, SiO and SiO_2) and implemented significantly improved surface temperature calculations.

Although more than half the planet is illuminated, none of the modelled atmosphere makes it far into the nightside. The Na atmosphere is the thickest since Na is very volatile, its sublimation is typically an order of magnitude greater than its silicate counterparts. However, the dayside magma ocean must readily supply the atmosphere with Na and oceanic flow must be fast to maintain the steady state. Because this oceanic flow must be several orders of magnitude greater than what is required to maintain an SiO and SiO_2 atmosphere, we expect Na to be starved from the atmosphere over time.

As for the pure SiO_2 atmosphere, it is the warmest of the three cases. Despite this, the pressure is very weak meaning that the SiO_2 relative abundance is likewise low in an actual mixed atmosphere. We therefore expect the effects of SiO_2 to play a small role in K2-141b's dynamics. SiO, on the other hand, is readily abundant on the surface and comparably volatile. The molecule's spectral features in the near-infrared are ideal for Spitzer and JWST. However, because of the SiO spectral properties, we must consider radiative heating in the model. Doing so not only captures a more realistic picture of K2-141b, but can also simulate observations with existing instruments.

4 Modeling Lava Planets: II

Chapter Summary

Our initial results for the atmospheric simulation of K2-141b show that an SiO dominated atmosphere is thin and hosts supersonic winds, typical for lava planets. However, our methods neglected radiative processes, and diverged significantly with models focusing on radiative transfer. Therefore, we couple the radiative dynamics to the existing hydrodynamics to better characterize lava planet atmospheres. Radiative transfer models show that the silicate atmosphere is expected to be hotter than the surface, and exhibit a strong negative lapse rate. However, our new results show that a strong negative lapse rate induces faster winds, and can cool the atmosphere significantly. We also see that when the atmosphere is far away from the substellar point, the increasingly thin atmosphere becomes horizontally isothermal, due to the heating and cooling radiative balance in the ultraviolet.

We begin with Section 4.1 discussing the insights of radiative transfer studies on lava planets. The steps to couple radiative processes to the hydrodynamics is featured in Sec. 4.2 and the model's results are in Sec. 4.3. In the Discussion section (4.4), we show how UV radiative heating and cooling (Sec. 4.4.1) and different vertical temperature profile (Sec. 4.4.2) affect K2-141b's atmosphere. Finally, the chapter conclusions can be found in 4.5. This chapter features work from Roxana Lupu where she provided the spectral properties of SiO. John Moores, Nicolas Cowan, and Raymond Pierrehumbert helped with feedback for the publication, Nguyen et al. (2022).

4.1 Motivation

As mentioned in Chapter 3, lava planets are expected to have a non-global atmosphere which is very difficult for general circulation models to handle. Many atmospheric studies on these planets therefore use radiative transfer models (e.g. Ito et al., 2015; Zilinskas et al., 2022). These works show that the silicate atmosphere on the dayside can heat up to be warmer than the surface and the temperature profiles can exhibit strong inversions. This is shown in Appendix B.4, Fig. B.2. As such, infrared spectroscopy should reveal dayside SiO emission features. However, these radiative transfer simulations neglect atmospheric circulation.

In contrast, we focused on the hydrodynamical flow of the silicate atmosphere, with an emphasis on the horizontal advection of heat and the spatial extent of the atmosphere. We had modelled an optically thin silicate atmosphere that did not absorb or emit any radiation. This made it difficult to simulate observables such as emission and transmission spectra. By construction, the optically thin atmosphere does not absorb stellar radiation and thus was everywhere colder than the surface.

Although our work are insightful for atmospheric dynamics, we have assumed a transparent atmosphere. Since SiO vapour absorbs infrared and ultraviolet radiation very well, we aim to eliminate this approximation by adding radiative transfer to the evaporation-driven hydrodynamics of K2-141b. We have also assumed a dry adiabatic vertical temperature profile, contrary to the radiative transfer studies of Ito et al. (2015) and Zilinskas et al. (2022). We therefore also test a wider range of vertical temperature profiles to harmonize with the radiative transfer simulations. The resulting model couples radiative transfer to atmospheric circulation, something yet to be done for lava planets. As an ancillary benefit, they also allow us to more faithfully predict observables.

4.2 Implementing Radiative Transfer

The numerical methods stay the same as those described in Chapter 3, Section 3.2, except for changes to the momentum and energy equations. First, the vertical temperature profile is parameterized with a constant β where $\beta = R/(R + C_p)$ for an adiabatic profile. For an isothermal atmosphere, on the other hand, $\beta = 1$. Likewise an atmosphere with a temperature inversion would have β greater than 1 (Figure 4.1 shows temperature – pressure profiles for different β). Details on β can be found in B.4.1. The isothermal and inverted profiles are more in line with the temperature profile predicted by Ito et al., 2015. We will test these three different profiles and see their effects on the dynamics and observability of the K2-141b's atmosphere.

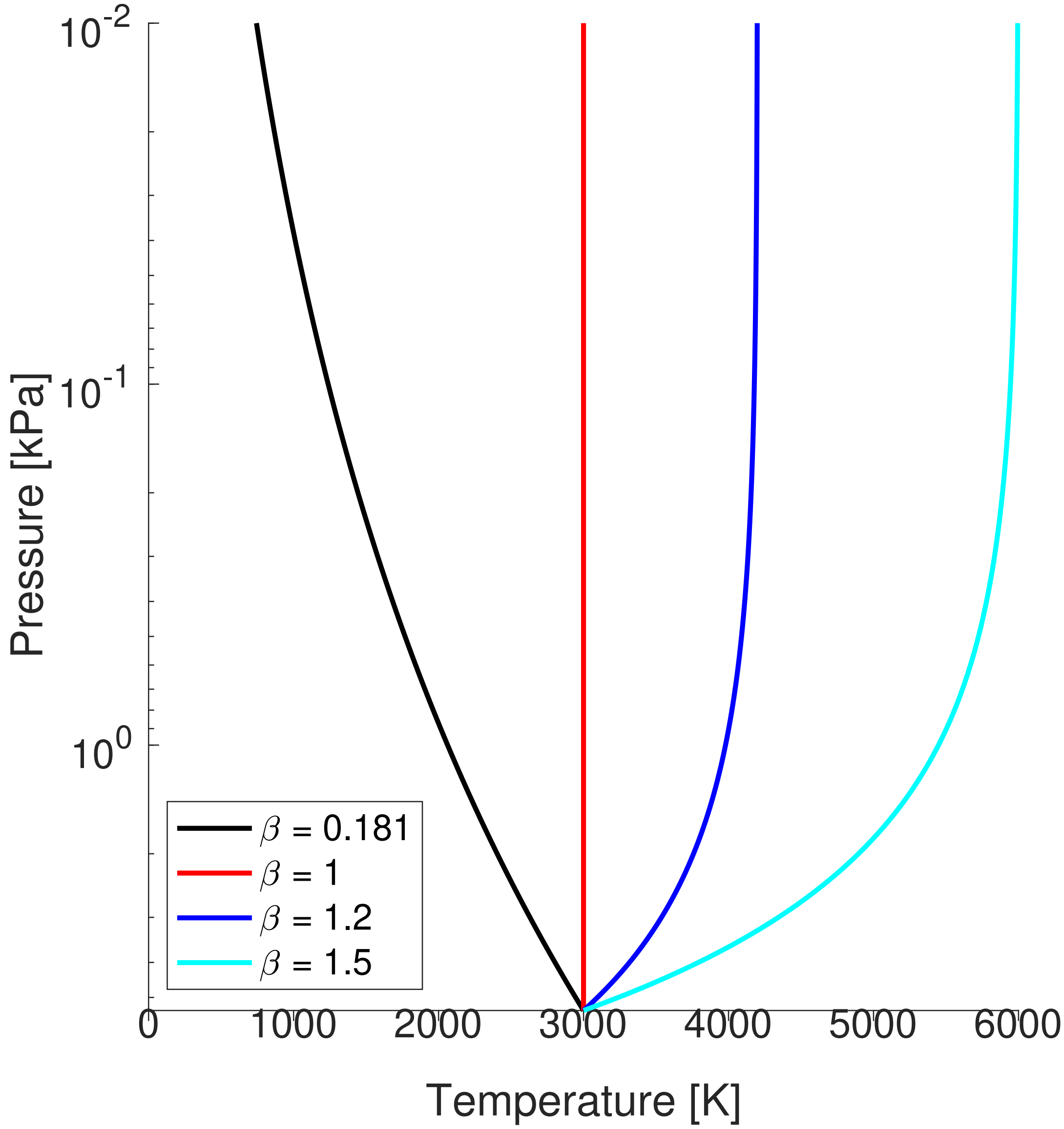

Figure 4.1: T-P profiles at the substellar point for different β. The black line represents the adiabatic profile. The red line represents isothermal and the two blue lines represent profiles with a temperature inversion.

Now we can introduce radiative terms to the energy balance, but we need the wavelength-dependent absorptivity of SiO and the stellar spectrum, both shown in Fig. 4.2. SiO absorbs strongly in the ultraviolet and relatively weakly in the infrared. Since SiO has negligible optical absorption, we only consider the IR and UV bands for heating and cooling of the atmosphere.

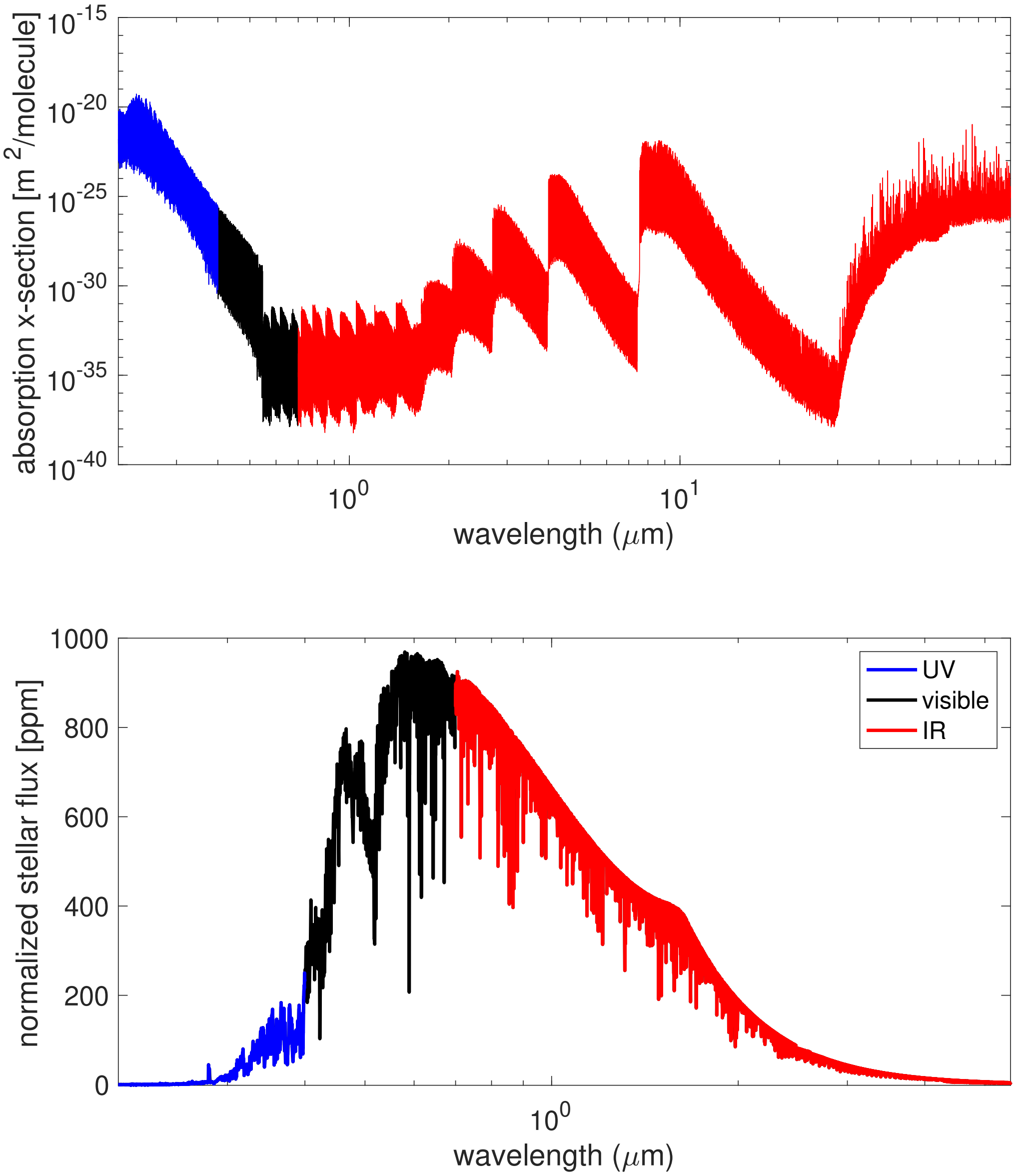

Figure 4.2: *Top*: absorption cross-section of SiO at 1 kPa and 2800 K. The UV data are from Kurucz, 1992 while the remainder are from Barton, Yurchenko, and Tennyson, 2013. Broadening parameters are approximated based on HITRAN data for similar diatomic molecules, assuming an H_2/He background atmosphere (Gordon et al., 2017); although this assumption is hard to justify, this is currently the best source of SiO absorption cross-section at high temperatures. *Bottom*: stellar spectrum of HD 85512 (France et al., 2016), a close analogue of K2-141.

Implementing radiative transfer starts with determining the absorptivity, or equivalently the emissivity, ϵ, in each waveband:

$$\epsilon = 1 - e^{-\tau_d}, \tag{4.1}$$

where τ_d is the optical depth. This depth is determined using the surface pressure:

$$\tau_d = xP_*/mg, \tag{4.2}$$

where x is the absorption cross-section of SiO in the IR or UV: $x_{\mathrm{IR}} = 10^{-29}\ \ \mathrm{m}^2/\mathrm{mole}$ and $x_{\mathrm{UV}} = 10^{-22}\ \ \mathrm{m}^2/\mathrm{mole}$.

With emissivity and absorptivity accounted for, we can now define the atmospheric heating Q as:

$$Q = Q_{\mathrm{sens}} + F_{\mathrm{IR}} + F_{\mathrm{UV}} + F_{\mathrm{surf}} - 2F_{\mathrm{RC}}, \tag{4.3}$$

where Q_{sens} is the sensible heating as described in Sec. 3.2, F_{IR} is the atmospheric absorption of stellar IR, F_{UV} is the atmospheric absorption of stellar UV, F_{surf} is the blackbody radiation emitted by the surface and subsequently absorbed by the atmosphere, and F_{RC} is the radiative cooling of the atmosphere. The radiative heating terms for the atmosphere are:

$$F_{\mathrm{IR}} = \epsilon_{\mathrm{IR}}\ C_{\mathrm{IR}}\ F_*, \tag{4.4}$$

$$F_{\mathrm{UV}} = \epsilon_{\mathrm{UV}}\ C_{\mathrm{UV}}\ F_*, \tag{4.5}$$

$$F_{\mathrm{surf}} = \epsilon_{\mathrm{IR}} \sigma T_s^4. \tag{4.6}$$

In the equations above, F_* is the incident stellar flux, which is a function of θ calculated following Kopal (1954) to account for the non-negligible angular size of the star as seen from the planet. For the stellar spectrum, we use the star HD 85512 as it is a close analogue of K2-141; $C_{\mathrm{IR}} = 0.532$ and $C_{\mathrm{UV}} = 0.009$ are the fraction of stellar flux in the IR and UV range, respectively (France et al., 2016). Both HD 85512 and K2-141 are K-type stars with an effective temperature of roughly 4400 K (Stassun et al., 2019).

We ignore stellar UV absorption via photo-dissociation of SiO because, as we show below, absorptivity and emissivity in the UV is $\sim$1 for most the dayside. Since nearly all of the stellar UV has been absorbed, any processes that can further absorb UV are negligible. Furthermore, significant photo-dissociation of SiO occurs at wavelengths less than 0.14 μm (Jolicard et al., 1997) and stellar flux in this range is negligible.

For radiative cooling, only considering IR emission would yield $F_{\mathrm{RC}} = \epsilon_{\mathrm{IR}} \sigma T_*^4$. However, since the absorption cross-section of the atmosphere is several orders of magnitude larger in the UV than the IR, UV emission becomes non-negligible. Therefore we split the $\epsilon \sigma T_*^4$ term using definite integrals of the Planck function, B, over IR and UV wavelengths, λ, and the equation for $F_{\rm RC}$ becomes:

$$F_{\rm RC}(T) = \pi\left(\epsilon_{\rm IR}\int_{\lambda_{\rm IR}} B(\lambda, T)d\lambda + \epsilon_{\rm UV}\int_{\lambda_{\rm UV}} B(\lambda, T)d\lambda\right). \tag{4.7}$$

A computationally efficient way to evaluate the Planck integral can be found in Appendix B.3. The surface albedo is assumed to be 0 and this is justified as quenched glass and liquid lava surfaces are expected to have very low albedo (Essack, Seager, & Pajusalu, 2020). We account for the greenhouse effect by radiatively coupling the atmospheric and surface temperatures:

$$\sigma T_s^4 = F_* - F_{\rm IR} - F_{\rm UV} + F_{\rm RC}(T). \tag{4.8}$$

Tying all these calculations into the system of equations in Sec. 3.2 will couple the radiative transfer to the hydrodynamics. We still solve for the state variables P_*, V_*, and T_* at the surface layer's boundary using the same numerical analysis.

4.3 Results

Starting with an adiabatic profile ($\beta = 0.18$), we first only include IR absorption and emission. The results did not differ much from a transparent atmosphere aside from having slightly stronger winds and warmer atmospheric temperatures. Atmospheric temperatures are still always cooler than the surface (cf. dotted and dashed lines in Fig. 4.3). Pressure almost never changes regardless of the radiative schemes or temperature profiles used as it cannot deviate far from the local saturation vapour pressure.

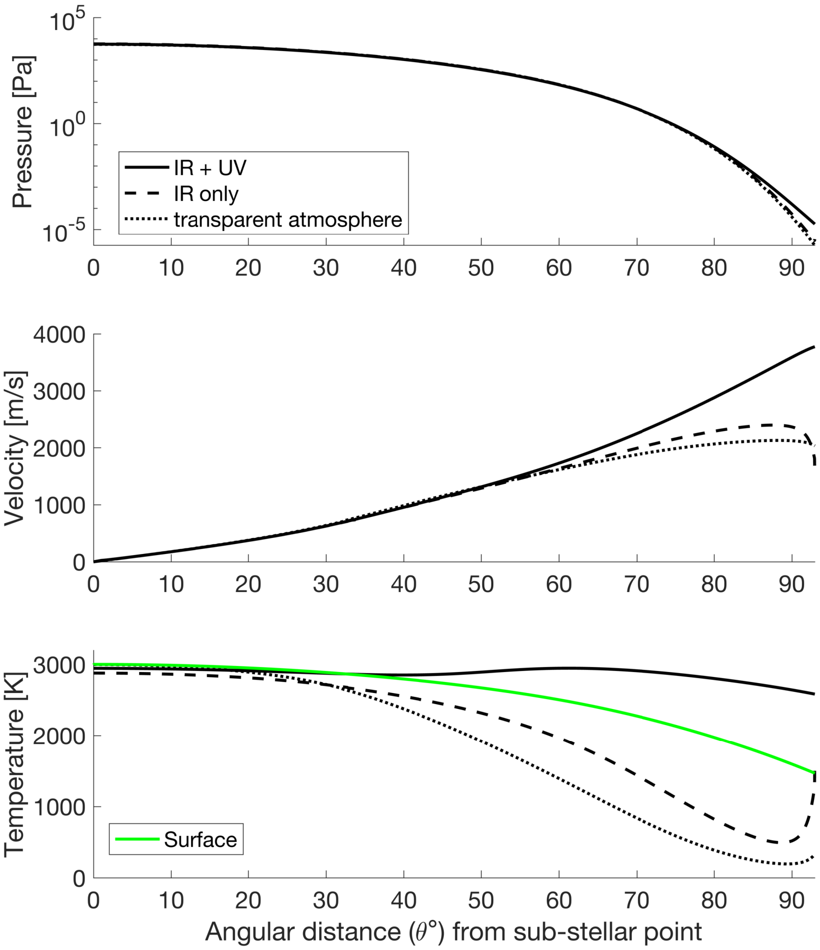

Figure 4.3: Atmospheric pressure, wind velocity and temperature from 1D hydrodynamic + radiative transfer simulations of K2-141b assuming an adiabatic vertical temperature-pressure profile. In each panel the dotted line represents the transparent atmosphere (no radiative transfer, as in Nguyen et al., 2020), the dashed line represents the simulation with only IR radiative transfer, and the solid line is the simulation incorporating both IR and UV radiative transfer. The IR-only radiative scheme is similar to the transparent case but the scheme with UV radiation produces stronger winds and a much hotter atmosphere. It can be seen that the temperature for the IR-only case rises significantly at high θ. This is caused by viscosity which slow winds and raises the temperature, but is only effective at low temperatures. However, the transparent atmosphere is just as cold but does not heat up. This is because it has significantly less pressure than its IR-only counterpart and there is not enough atmospheric mass for friction to take effect.

When we add UV radiation in addition to IR, the resulting winds are stronger and the atmospheric temperature exceeds that of the surface for $\theta > 32^\circ$ (solid lines in the bottom panel of Fig. 4.3). The reason for the high atmospheric temperature is the high optical depth in the UV compared to that in the IR. As shown in the middle panel of Fig. 4.4, UV absorptivity hovers around unity while the IR opacity, being very sensitive to pressure, drops exponentially with θ.

The bottom panel of Fig. 4.4 shows that IR absorption from stellar flux and surface blackbody radiation start out as the dominant heating terms, balanced by IR radiative cooling. As pressure drops, however, IR radiation becomes negligible and the UV radiative terms come to dominate the energy balance.

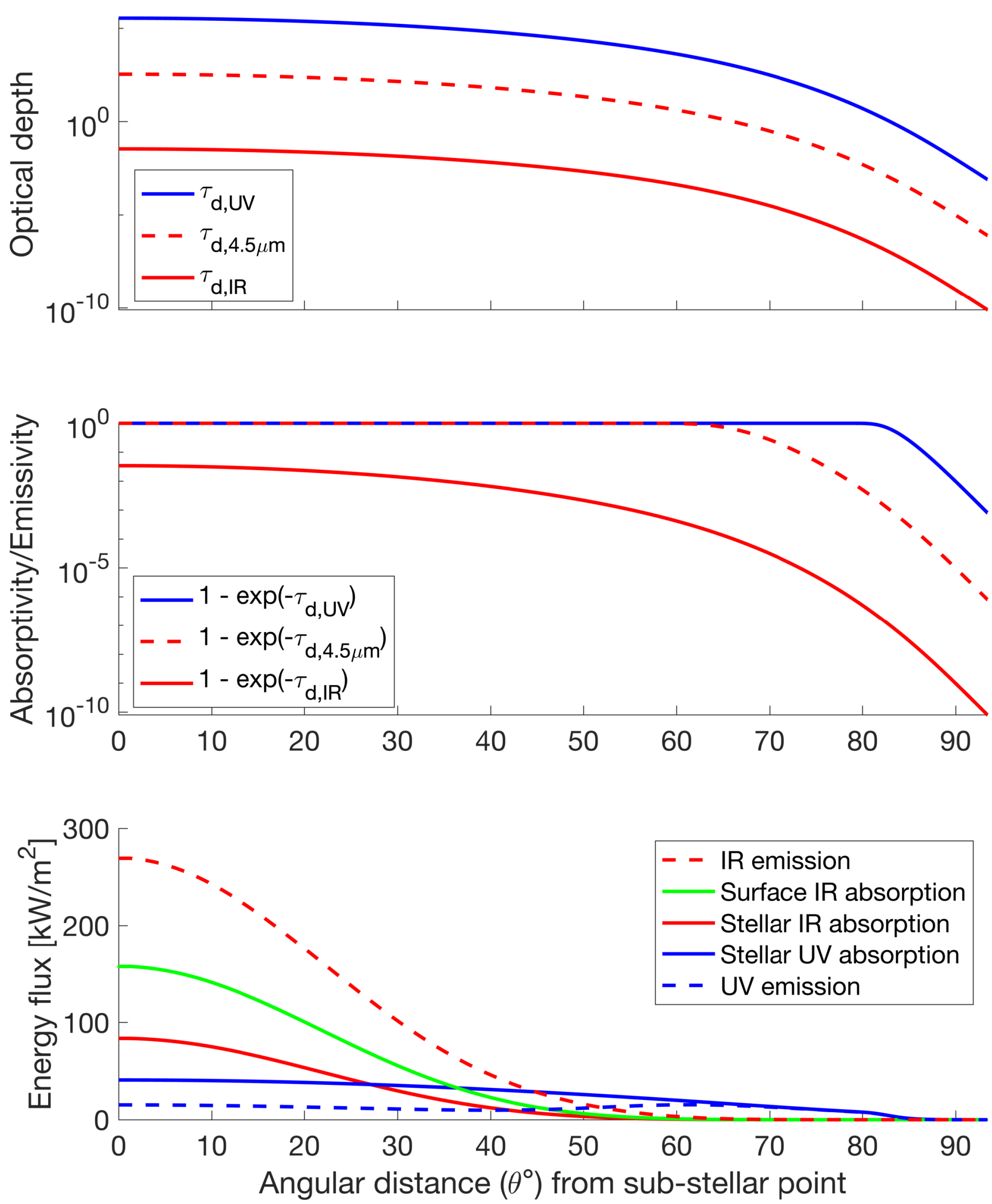

Figure 4.4: Radiative properties of the adiabatic atmosphere. *Top*: vertical optical depth of the SiO atmosphere. *Middle*: vertically integrated absorptivity (equivalently emissivity). *Bottom*: radiative fluxes absorbed and emitted by the atmosphere. The emissivity in the UV is ~1 for most of the dayside while emissivity in the IR drops exponentially away from the substellar point. While UV heating and cooling are relative small near the sub-stellar point, they dominate the radiation budget at $\theta > 50^{\circ}$.

Finally, we incorporate IR and UV radiation to two other vertical temperature profiles: isothermal ($\beta = 1$) and inverted ($\beta = 1.2$). Pressure, wind speed, and temperature for the three vertical profiles are shown in Fig. 4.5. Higher β produce stronger winds and a cooler atmosphere; in Section 4.4.2, we offer a physical explanation of this phenomenon. Near the day-night terminator, however, atmospheric temperatures are the same regardless of β.

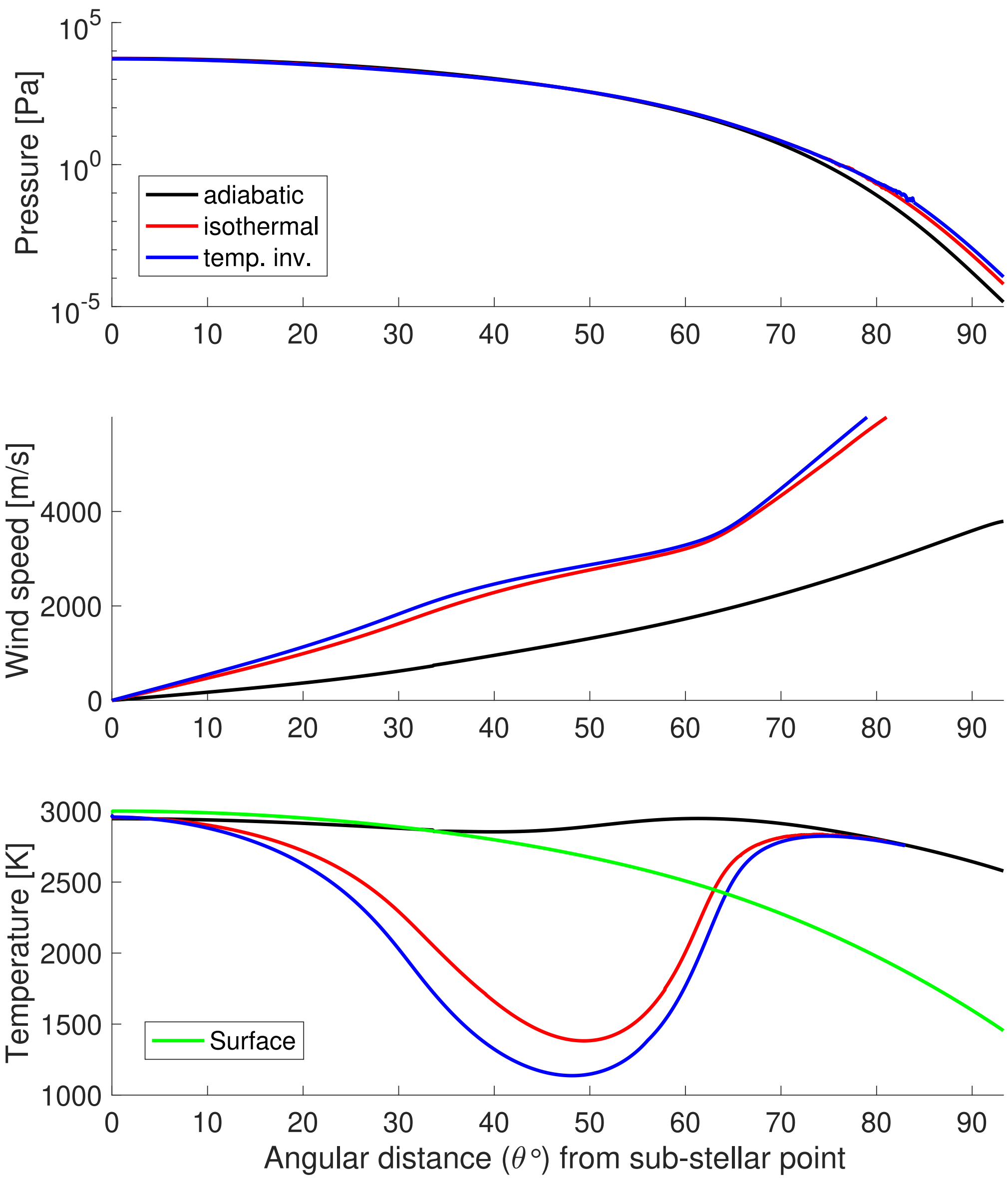

Figure 4.5: Results of hydrodynamic simulations including IR and UV radiative transfer for different vertical temperature profiles. *Top*: atmospheric pressure. *Middle*: wind velocity. *Bottom*: atmospheric temperature. The black line is the adiabatic profile, red is isothermal, and blue is the inverted temperature profile. Larger β increase wind speed and decrease temperature. However, the temperature for all three profiles converge at $\theta > 80°$.

4.4 Discussion

4.4.1 UV impact on dynamics

Our simulations show that the exchange of IR radiation between surface and atmosphere does not change the dynamics significantly despite the large fluxes. This is because IR heating and cooling are well balanced, leading to a near zero net radiation budget. However, IR radiation becomes negligible at low pressure making UV stellar flux the dominant heating term, balanced by UV radiative cooling.

The importance of UV cooling in a planetary atmosphere is surprising but understandable. Fig. 4.6 shows the IR and UV cooling at a fixed pressure. For uniform emissivity at all wavelengths, the blackbody radiation in the IR accounts for almost all of the radiative cooling. However, because emissivity in the IR is much lower than in the UV, UV emission can overtake the IR with only a slight increase in temperature.

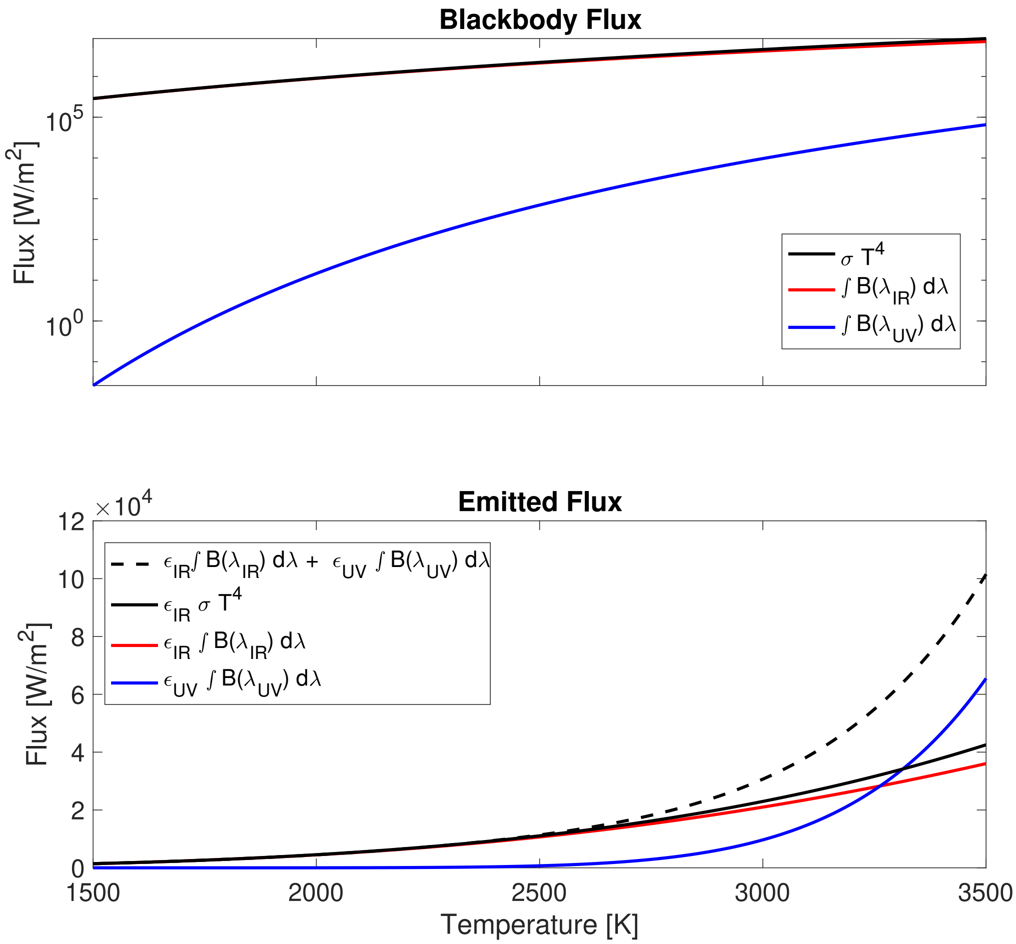

Figure 4.6: *Top*: atmospheric radiative cooling terms featured in Eq. 4.7. The black line is the total blackbody radiative flux across all wavelengths, red is the IR contribution, and blue is the UV contribution. At constant emissivity, IR flux would be order of magnitude greater than UV flux. *Bottom*: emitted blackbody radiation at a fixed pressure. The dashed black line is the total emitted flux, the solid black line is what the emitted flux would be if the total emission is dependent only on IR emissivity, the red line is the individual emitted flux in the IR and blue in the UV. Note that UV emission becomes non-negligible when atmospheric temperatures exceed 2500 K.

The temperature sensitivity of UV emission explains the horizontal uniformity in temperature, especially near the terminator ($\theta = 90°$). As pressure drops, UV stellar flux is the only heating term and IR cooling is ineffective. The atmosphere will get hotter until UV radiative cooling takes over. Therefore, temperature will hover around 2600 K where UV heating and cooling are in equilibrium, regardless of the assumed vertical profile (see bottom panel of Fig. 4.5).

4.4.2 Effects of Different Temperature Profiles

As described in section 3.2, the model atmosphere's vertical temperature profile can be made isothermal by setting $\beta = 1$ or inverted for $\beta > 1$. This stems from the vertical integration of the pressure which only affects the momentum equation (Eq. 3.16). The higher β value implies a much stronger pressure force, the term $\beta C_p T_* P_*/[gr\tan(\theta)]$ in Eq. 3.16. This is why winds are stronger for isothermal and inverted temperature profiles as seen in Fig. 4.5. We plot the temperature profiles at two different locations in Fig 4.7.

Physically, a negative lapse rate means the near surface atmosphere is cooler and therefore always denser than the air above it. Vertical flow is restricted in this regime and this leads to stronger horizontal flow. The dynamics here is most pronounced when the vertical temperature inversion is near the surface, where most of the atmospheric mass lies. On Earth, where the stratosphere is far from the surface, a negative lapse rate does not force stronger horizontal motion.

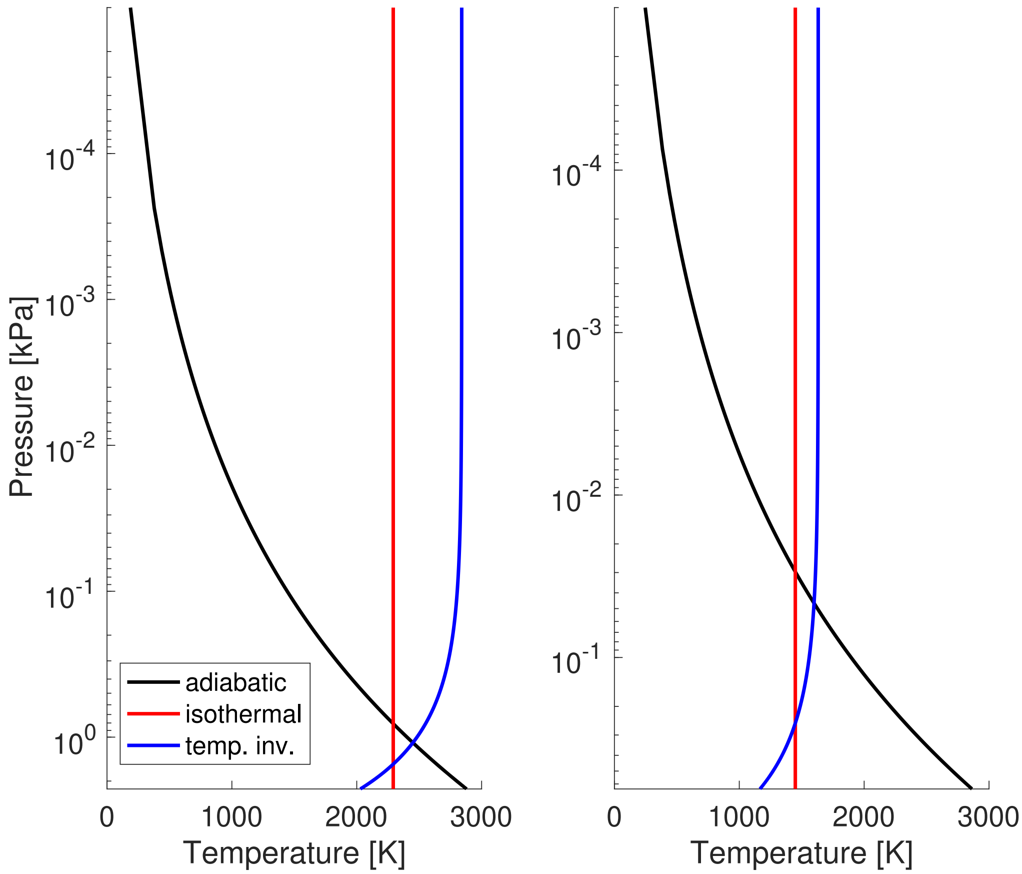

Figure 4.7: Temperature profiles at $\theta = 30°$ (left) and $\theta = 45°$ (right). While the adiabatic profile stays largely the same at both location (cf. Bottom panel of Fig. 4.5), the isothermal and inverted temperature profiles are cooler at $\theta = 45°$.

Stronger winds also induce more evaporation and condensation and this can be inferred from the mass equation (Eq. 3.2): a larger V_* must lead to a larger E. Therefore, a strong vertical temperature inversion has a greater evaporation and condensation rate as seen in Fig. 4.8.

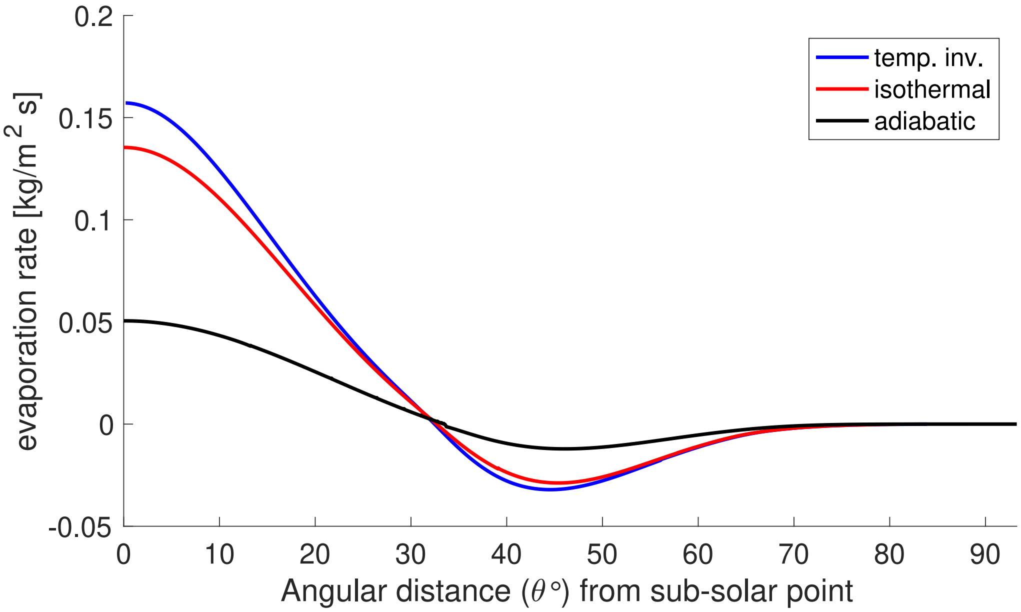

Figure 4.8: Evaporation rate for different vertical temperature profiles. Because decreasing the lapse rate results in stronger winds, evaporation and condensation are greater for the isothermal and inverted temperature profiles than the adiabatic profile.

Wind speed and atmospheric temperature are coupled within the energy equation (Eq. 3.5), hence the increase in wind speed greatly affects temperature. The term $(V_*^2/2 + C_pT_*)$ is balanced by Q which is mostly dependent on the incoming stellar flux. As stellar flux does not change regardless of the vertical temperature profile, a lower temperature is required to balance out the stronger wind speeds.

Radiative transfer models that do not account for horizontal flow predict an inverted temperature profile where the overall atmospheric temperature is hotter than the surface (Ito et al., 2015). The hydrodynamics we present here suggests otherwise: the stronger the inversion, the faster the horizontal flow and the cooler the atmosphere. However, because the lapse rate is set up to be the same everywhere (β is constant with respect to θ), the hydrodynamical effects may be overestimated.

4.5 Chapter Conclusions

We have improved upon our 1D hydrodynamic model by implementing radiative transfer. We reapplied this new model to the lava planet K2-141b and tested the effects of different vertical temperature profiles. Our analysis leads to two key insights.

Our first insight is that the atmosphere far from the sub-stellar point will be hotter than the surface. Since UV heating dominates over IR when pressure is low, atmospheric temperatures will rise to $\sim$2600K, at which point UV radiative cooling takes effect. As a result, atmospheric temperatures should be horizontally uniform near the terminator ($\theta \approx 90°$), regardless of vertical temperature profile.

The second insight is that a vertical temperature inversion produces a cooler atmosphere. A strong temperature inversion also leads to a greater horizontal pressure gradient force and hence greater wind speeds. To conserve energy, thermal energy in the atmosphere is reduced as a reaction to the greater kinetic energy. This result is particularly important as it shows how hydrodynamics can lead to a significantly different atmosphere when compared to models that focus on 1D radiative balance (e.g., Ito et al., 2015).

Because we have implemented radiative processes for our atmospheric model, we can now account for the planet's radiative absorption and emission. The silicate atmosphere of lava planets, dominated by SiO, has a very strong absorption feature in the near-infrared region observable with Spitzer and JWST. Therefore, we can use our results to simulate observations to help characterize K2-141b's atmosphere using Spitzer data (Zieba et al., 2022), and eventually JWST (Dang et al., 2021).

5 | Observing Lava Planets

Chapter Summary

We have coupled radiative transfer to the 1D hydrodynamical model of K2-141b's in the previous chapter. Because this has yet to be done for lava planets, our work has lead to unique insights into the atmosphere's dynamics. Since our analysis is different from previous radiative transfer only studies, we should get different simulated observations as well. Using our results, we simulate the transit and eclipse spectra of K2-141b. Even though a silicate atmosphere with full radiative processes is warmer, and has a larger scale height, the pressure at the terminator is still too low to produce a meaningful transmission signal in the IR; the transit depth in the UV is much greater but is currently out of reach for current instruments. The eclipse spectrum shows significant SiO features visible with Spitzer and JWST. However, due to the hydrodynamics, what should be observed are absorption features as opposed to emission features as hypothesized by previous studies.

Section 5.1 describes how lava planet atmospheres might be observed. Section 5.2

shows the formulation for finding the transit depth and our simulated transmission spectrum. Likewise, Section 5.3 shows how emissions are determined and features our simulated phase curve and emission spectrum of K2-141b. Finally, the chapter conclusions are found in Sec. 5.5.

5.1 Background

Lava planets have extreme orbits similar to Hot Jupiters. Their proximity to the star, as well as having "ultra-short" periods, can lead to great signal-to-noise ratio when using the radial velocity or the transit method. As such, these planets are prime targets for observing terrestrial exoplanets and may be the first rocky bodies to have an atmosphere detected outside the solar system. Since its discovery, K2-141b remains the best target among lava planets due to the unprecedented precision of its orbital measurements (Dang et al., 2021; Kreidberg et al., 2018; Malavolta et al., 2018).

Our analysis in Chapter 3 suggests that the dominant gas species in the atmosphere is SiO due to its abundance in the crust and volatility; other radiative transfer works such as Zilinskas et al. (2022) share the same conclusion. Lighter, more volatile components such as Na, are scarce, unable to diffuse back to the dayside, and prone to hydrodynamical escape (Ito & Ikoma, 2021). Therefore, probing for SiO features remain the best way to observe an atmosphere on K2-141b and other lava planets.

SiO has strong absorption features in the IR, making it ideal to detect with Spitzer and JWST. However, its much stronger absorptivity in the UV may heat up the atmosphere's upper levels and induce a strong negative lapse rate. Such scenarios often lead to emission features where the atmosphere's signal is stronger than a bare-rock case at eclipse. However, our results in Chapter 4 show a cooler silicate atmosphere, which can produce a much different spectra than what was previous thought. Therefore, we simulate transit and eclipse observations from our radiative hydrodynamical simulation of K2-141b.

5.2 Transmission Spectroscopy

When a planet transits a star, some of the starlight is blocked from the observer and we see a noticeable dip in stellar flux; this is the most common method of detecting exoplanets. During transit, some of the starlight traverses through the atmosphere and its spectrum subtly changes. Atmospheric detection and subsequent characterization for winds or clouds have been done for Hot Jupiters (Snellen, 2014; Wakeford & Sing, 2015).

It is generally assumed that transit spectroscopy only probes the atmosphere 90° from the subsolar point. However, the especially close orbit of K2-141b deviates substantially from the default transit geometry. As illustrated in Fig. 5.1, regions probed during transit can be quite far from $\theta = 90°$ for ultra-short period planets. The start and end of transit therefore probe regions with a significant atmosphere. For the specific case of K2-141b and assuming an impact parameter of zero (consistent with observational constraints), ingress and egress probe equatorial regions at an angle $\tan^{-1}(R_*/a) \simeq 26^\circ$ away from the usually assumed $\theta = 90^\circ$ (for sight lines offset from the planetary equator, the observed θ is closer to 90°).

This opens up an avenue for high-dispersion spectroscopy where Doppler shifts from the changing radial velocity of the planet can help disentangle planetary and stellar absorption features and potentially detect atmospheric winds (Snellen, 2014). Note that the extreme orbit of K2-141b leads to significant changes in radial velocity over the course of the transit.

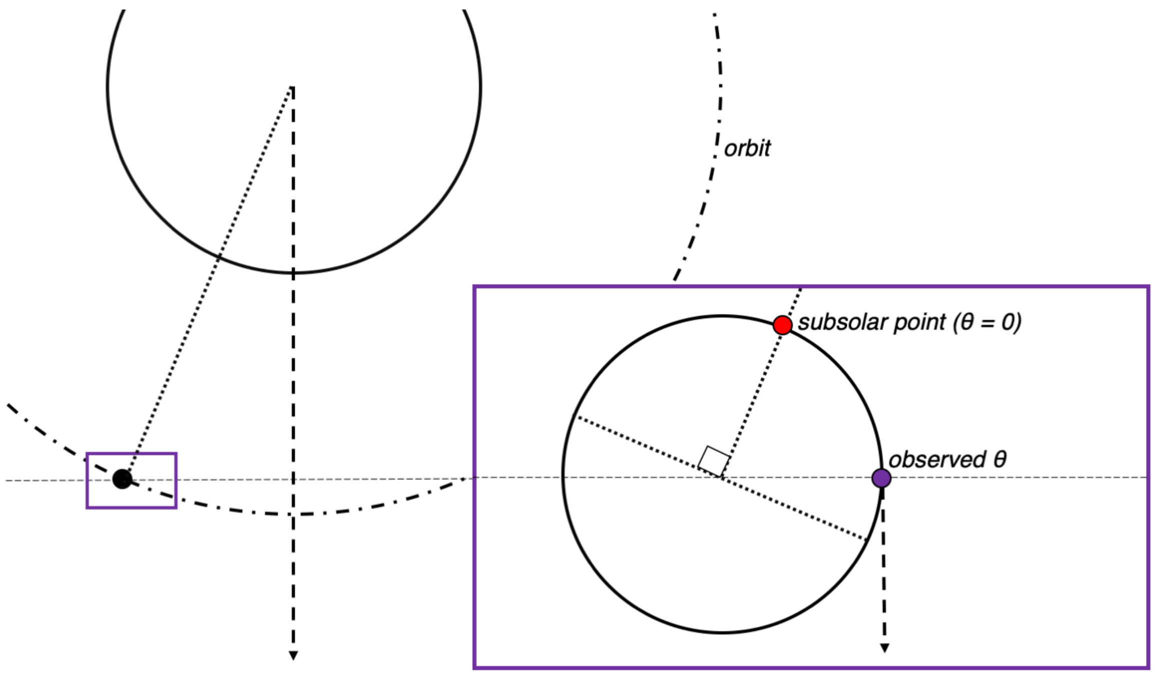

Figure 5.1: Illustration of the observed longitude during a transit (the observer is at the bottom of the page). The star and planetary orbit are drawn to scale.

We can now use our model atmospheres to simulate observations, the first of which is a transit spectrum. This is done by calculating the transit depth, D, the fraction of stellar flux blocked as the planet passes in front of its star. This is evaluated by:

$$D(\lambda)_{\mathrm{t}} = \left(\frac{r}{r_*}\right)^2 + \frac{2}{r_*^2}\int_r^{r_*} b(1 - e^{-\tau_c(\lambda, b)})db, \tag{5.1}$$

where r and r_* are the planetary and stellar radii respectively, b is the projected distance to the planet's centre, and τ_c is the optical depth along the cord. Optical depth is calculated by:

$$\tau_c(b) = \frac{xP_*}{mg}\sqrt{\frac{2\pi r}{H}}, \tag{5.2}$$

where H is the atmospheric scale height in the middle of the transit, the relevant surface pressure P_* and H must be evaluated at $\theta = 90°$, but the extreme geometry of lava planets means that the a wide range of θ, surface pressures, and scale heights are probed throughout transit, as shown in Fig. 5.2. Because the boundary layer is geometrically thin compared to scale height, P_* can be approximated as the surface pressure.

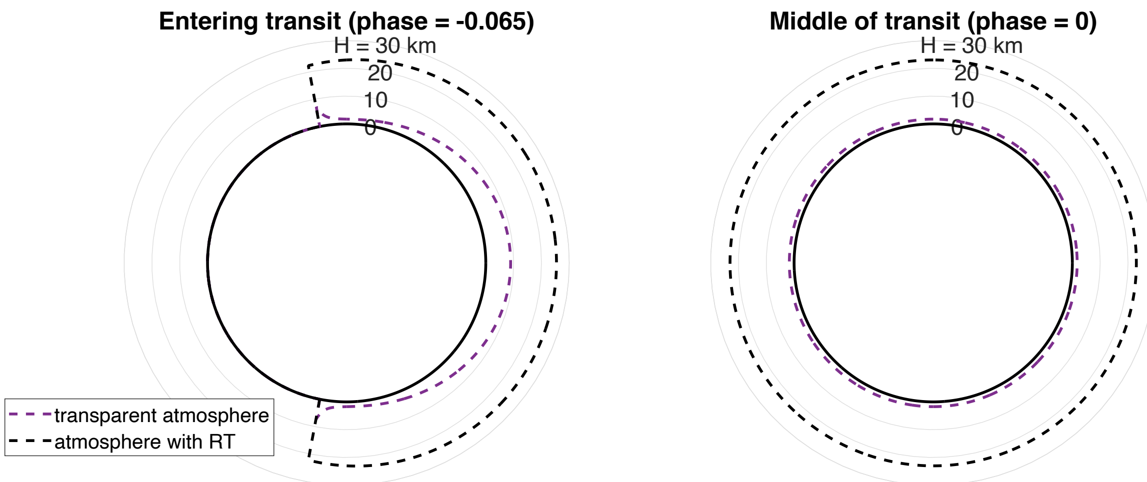

Figure 5.2: Scale height as observed at ingress (left) and transit (right). Assuming an impact parameter of 0, we plot the expected scale height around the planet's limb. At ingress, the viewing geometry exposes much of the airless nightside (left side of the limb) and we can only see the dayside atmosphere on the right-hand side. At transit, limb measurements only probe where $\theta = 90°$ and scale height is constant due to the imposed axial symmetry. Incorporating radiative transfer in our dynamical model produces a much hotter and hence more extended atmosphere near the terminator, leading to a near-constant transmission spectrum throughout the transit.

Due to the UV radiative equilibrium, atmospheric temperatures would hypothetically be the same temperature at the terminator regardless of the vertical temperature profile. These temperatures are much hotter than that of the transparent atmosphere described in Chapter 3, increasing the atmospheric scale height and providing a stronger signal for transmission spectroscopy of lava planets.

Evaluating τ_c and completing the integration in Eq. 5.1 produces the transit spectra shown in Fig. 5.3. The biggest peak is at $\sim$0.25 μm and the second biggest at $\sim$9 μm, both corresponding to SiO absorption features since our model atmosphere is entirely composed of that gas. By virtue of having slightly higher atmospheric pressure and therefore greater optical depth at the terminator (see Fig. 4.5), the isothermal and inverted atmospheres have larger transit spectrum features than the adiabatic case.

The spectral feature in the UV is the strongest but likely requires precision beyond the capabilities of the Hubble Space Telescope. But we only simulate the bound atmosphere of the planet—it is possible that UV observations with Hubble would be sensitive to its exosphere. Transit spectral features in the range of JWST NIRSpec and Spitzer IRAC are negligible while features in the range of JWST MIRI are significant. We use the PandExo tool from Batalha et al. (2017) to simulate JWST measurement uncertainties for 16 transits and conclude that neither NIRSpec or MIRI have the precision to identify any spectral features induced by the atmosphere in transit.

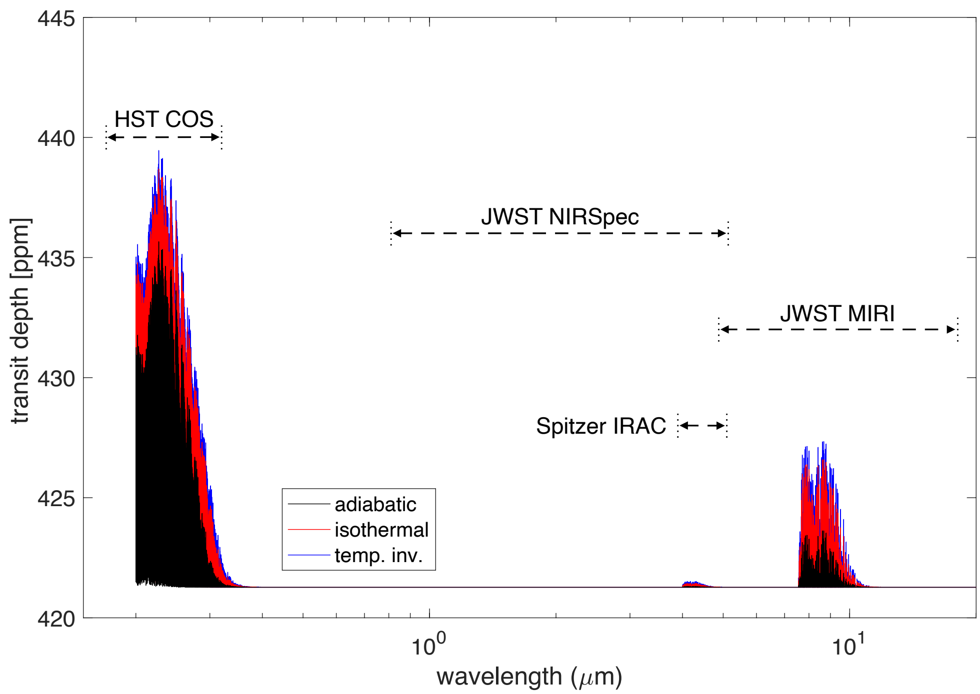

Figure 5.3: Expected transit spectrum of K2-141b for three possible vertical temperature profiles. Dashed lines show the bandpasses for HST/COS (Green et al., 2011), JWST/NIRSpec (Birkmann et al., 2016), Spitzer/IRAC channel 2, and JWST/MIRI (Wells et al., 2015). The UV spectral feature is in-band for Hubble but is likely too small to be detectable. Likewise, the IR features around 4.5 and 9 μm, while in-band for Spitzer or JWST, are too faint to be disentangled from noise. Although cases with different T-P profiles have roughly the same scale height at $\theta = 90°$, the surface pressure is slightly larger for profiles with a negative lapse rate. This explains the slight differences in transit depth between the T-P profiles.

5.3 Emissions and Phase Curves

The predicted blackbody radiation of K2-141b required to produce the planet's emission is calculated using the methods from Cowan and Agol (2008) and Cowan and

Agol (2011). The first step is to convert temperature, T to blackbody radiative intensity, I [W m^{-2} m^{-1} sr^{-1}] at wavelength λ:

$$I = \frac{2hc^2}{\lambda^5} \frac{1}{e^{hc/(\lambda kT)} - 1}, \tag{5.3}$$

where h is the Planck constant, c is the speed of light, and k is the Boltzmann constant. The next step is to create an intensity map with latitude (α) and longitude (ϕ) from angular distance (θ) from the subsolar point using the Spherical Pythagorean Theorem:

$$I(\alpha, \phi) = I(\theta = \cos^{-1}[\cos(\alpha)\cos(\phi)]). \tag{5.4}$$

Now that each latitude (α) and longitude (ϕ) coordinate has a radiative intensity, we then integrate the intensity across the hemisphere visible to the observer. Assuming an edge-on viewing geometry where the observer is on the planet's orbital plane, the observed radiative flux, F, is calculated by:

$$F(\xi) = \int_0^{\pi} \int_{\xi-\pi/2}^{\xi+\pi/2} I(\alpha, \phi) \sin^2 \alpha \cos(\phi - \xi)\ d\alpha\ d\phi, \tag{5.5}$$

where ξ is the planet's position around the orbit. The stellar flux at the corresponding wavelength is calculated in the exact same way but with a uniform temperature of 4599 K (Malavolta et al., 2018) and scaled to the ratio of $(r_{\mathrm{star}}/r_{\mathrm{planet}})^2$. This therefore yields the ratio of planetary to stellar flux at that point as a function of the planet's orbital motion about its star, the so-called phase curve. All the parameters mentioned in the chapter are summarized in Table B.2.

We can use our preliminary results from Chapter 3 to simulate K2-141b's phase curves for different atmospheric constituents (see Fig. 5.4). These initial results did not radiatively couple the surface and the atmosphere, and so emissions from the surface and atmosphere are done separately. For the phase curves of Fig. 5.4 to be correct, the atmosphere would have to have an opacity of $\sim$1 at the the specified wavelength and $\sim$0 around said wavelength. However, with the inclusion of radiative transfer, and more so the energy coupling of the surface and atmosphere in Chapter 4, we can simulate a more realistic emission spectrum of K2-141b.

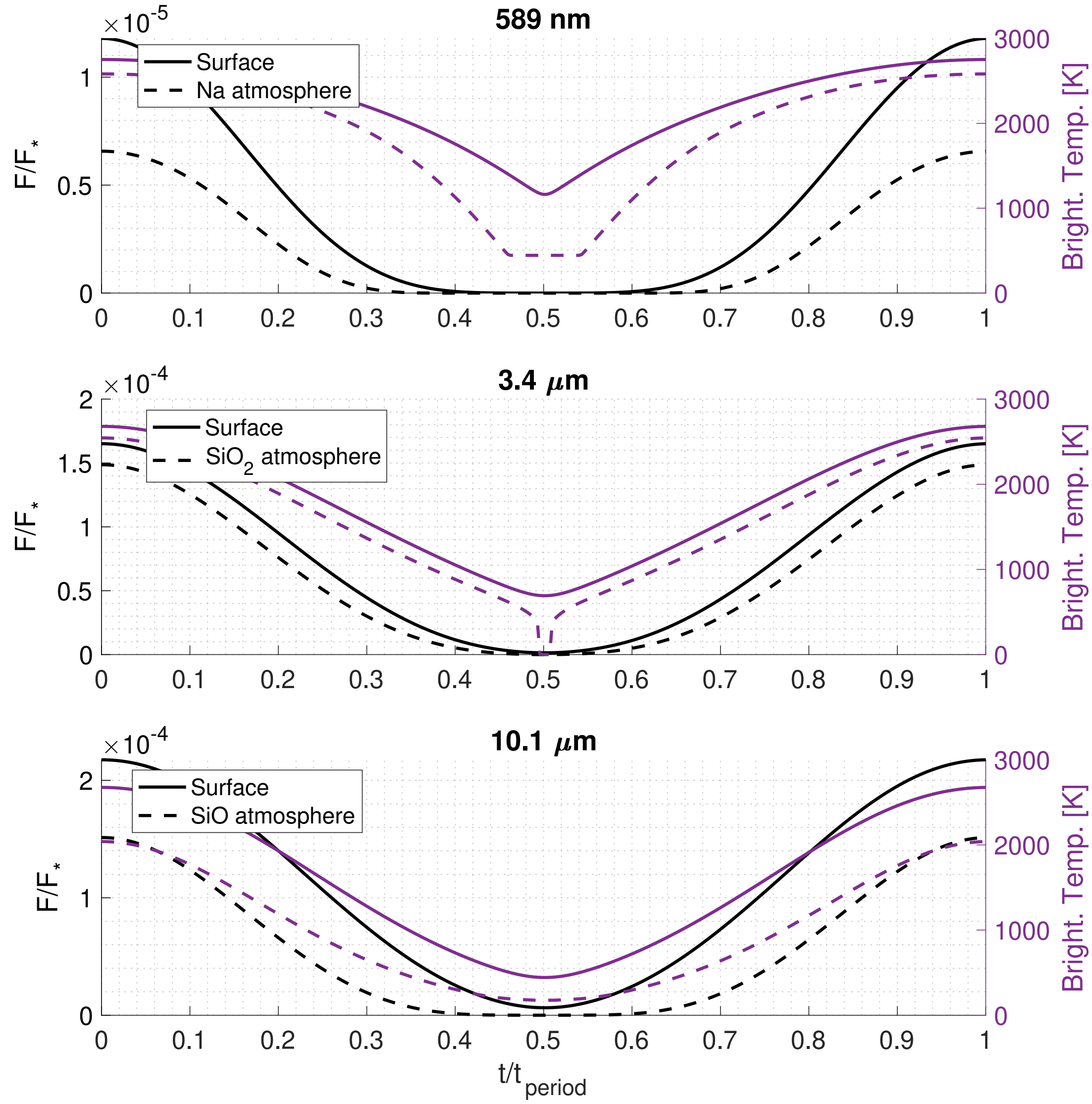

Figure 5.4: Top: predicted blackbody radiation of K2-141b at 589 Na spectral feature (left/black) and phase-dependent disk-integrated planetary brightness temperature (right/purple). Middle: the same for the 3.4 micron SiO_2 spectral feature. Bottom: the same for the 10.1 micron SiO spectral feature. Note that eclipses and transit have been omitted but would occur at 0 and 0.5 respectively. The phase curve is shown as the flux ratio between the planet and star. Solid lines refer to the surface (a wavelength just outside the spectral feature) and dashed lines refer to the atmosphere (a wavelength in the spectral feature).

To better calculate the emission spectrum of K2-141b at eclipse, we first calculate the top-of-atmosphere outgoing irradiance, which is a combination of atmospheric and planetary emission. While the greenhouse effect barely changes the surface temperature, it is significant enough to affect the planet's emission spectrum. Emission from the atmosphere is calculated as $\epsilon_\lambda B(\lambda, T_*)$ while the surface contribution is calculated as $(1 - \epsilon_\lambda)B(\lambda, T_s)$. The top two panels of Fig. 5.5 show the atmospheric and surface irradiance at 4.5 μm, where there is a strong SiO spectral feature. The bottom panel shows the total top-of-atmosphere outgoing irradiance.

The optical depth, $\tau_d = 1$, in the IR if the pressure is 1.6×10^5 Pa; $\tau_d = 1$ in the UV whenever the pressure is 0.016 Pa. This signifies how vertically constrained UV heating is in a pure SiO atmosphere. At 4.5 μm, $\tau_d = 1$ when the pressure is 16 Pa. At the substellar point where surface pressure is 10^3 Pa, observations at 4.5 μm will only probe the top of the atmosphere (here, $H = 25$ km). However, pressure decreases significantly when far away from the substellar point where τ_d is 1 within a scale height if the angular distance, θ is greater than 60°.

Although it is justifiable to use surface temperatures when far away from the substellar point, emissivity at 4.5 μm is sensitive to top of the atmosphere near the substellar point. From our definition of β which can be found in B.4.1, the general lapse rate is set but local lapse rate can vary.It is possible for T-P profiles to have wildly different temperatures at the top of the atmosphere yet yield the same β parameterization. Ultimately, there is still too much variability in how we determine T-P profile and using near surface atmospheric conditions simplify simulated observations greatly.

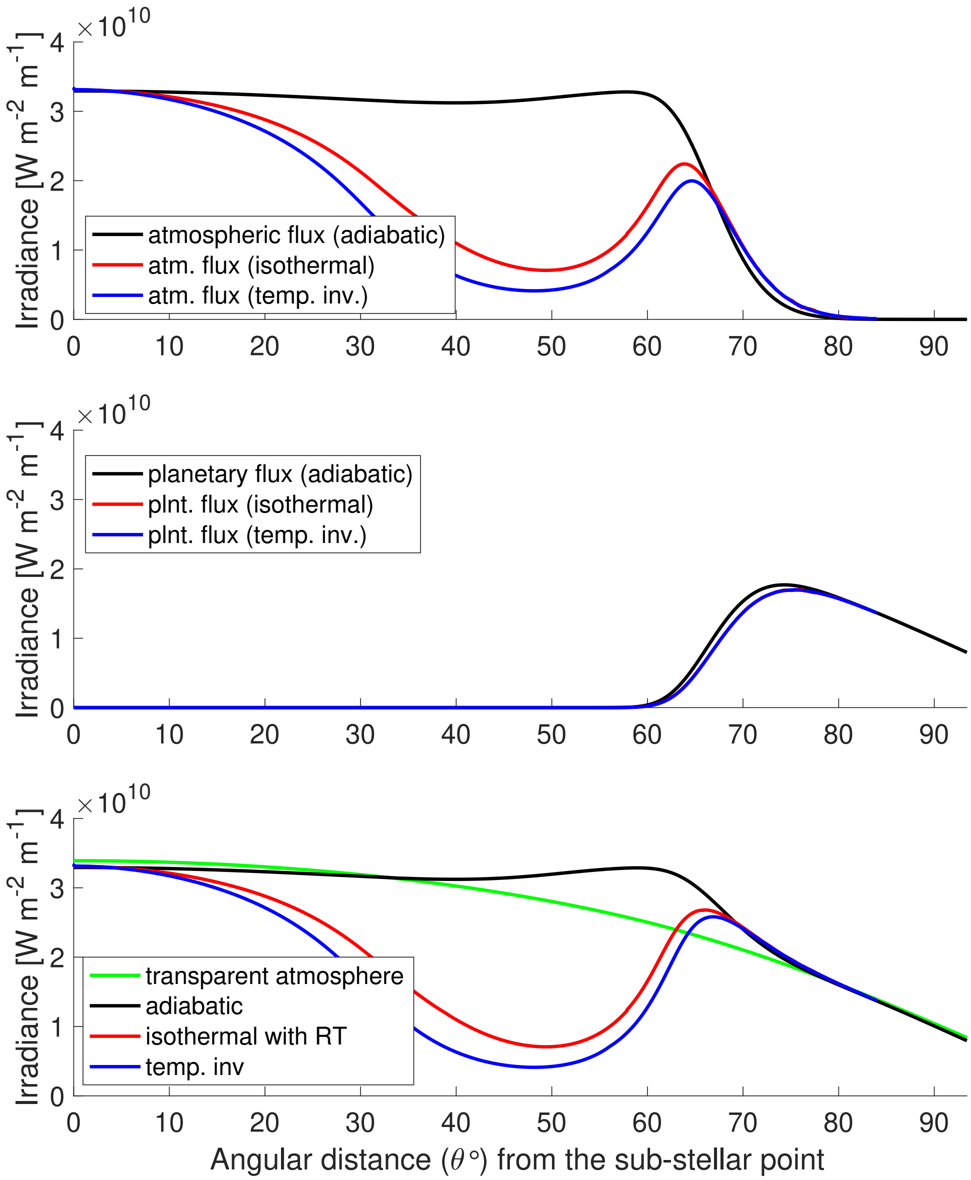

Figure 5.5: Irradiance of K2-141b at 4.5 μm i.e, at a wavelength where the atmosphere is optically thick over much of the dayside. *Top*: modeled outgoing atmospheric irradiance. *Middle*: outgoing planetary irradiance. *Bottom*: total outgoing irradiance at the top of the atmosphere. The adiabatic case has stronger emission at this wavelength while the other two cases have a weaker emission than the transparent atmosphere.

Keeping λ fixed at 4.5 μm and calculating $F(\xi)$ (from Eq. 5.5) yields the phase curve shown in Fig. 5.6. Because the dayside emission from the isothermal and inverted temperature profiles are smaller than the adiabatic case, their phase amplitudes are likewise smaller. Eclipse occurs when $\xi = 0$, and calculating F with respect to λ at this point leads to the eclipse spectrum plotted in Fig. 5.7.

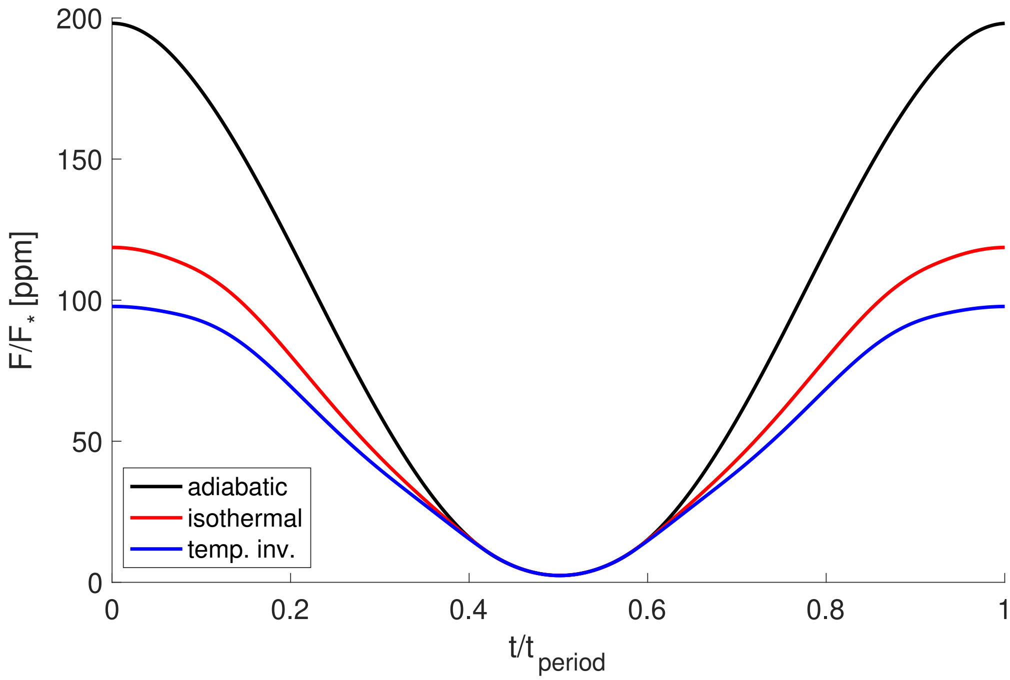

Figure 5.6: Simulated 4.5 μm phase curves from the three different vertical temperature structures. Note that eclipses have been omitted at phases 0 and 1; transit is omitted at phase 0.5. The adiabatic temperature profile produced an atmosphere with stronger dayside emission and therefore a larger phase amplitude.

Paradoxically, the adiabatic profile results in SiO spectral emission features while the isothermal and inverted profiles result in absorption features. SiO spectral features probe the atmosphere rather than the surface over much of the dayside. The adiabatic profile produces an atmosphere hotter than the surface and therefore its spectrum shows emission features. Meanwhile, the isothermal and inverted temperature profiles lead to cooler atmospheres (bottom panel of Fig. 4.5) and hence their spectra show absorption features.

We simulate JWST measurement uncertainties for 16 eclipses using PandExo (Batalha et al., 2017), plotted in the bottom panel of Fig. 5.7. Spectral features at 4.5 μm can be detected with NIRSpec. Spectral features at longer wavelengths are difficult to see with MIRI but observing more eclipses or phase curves may reduce the errors enough to make out the features.

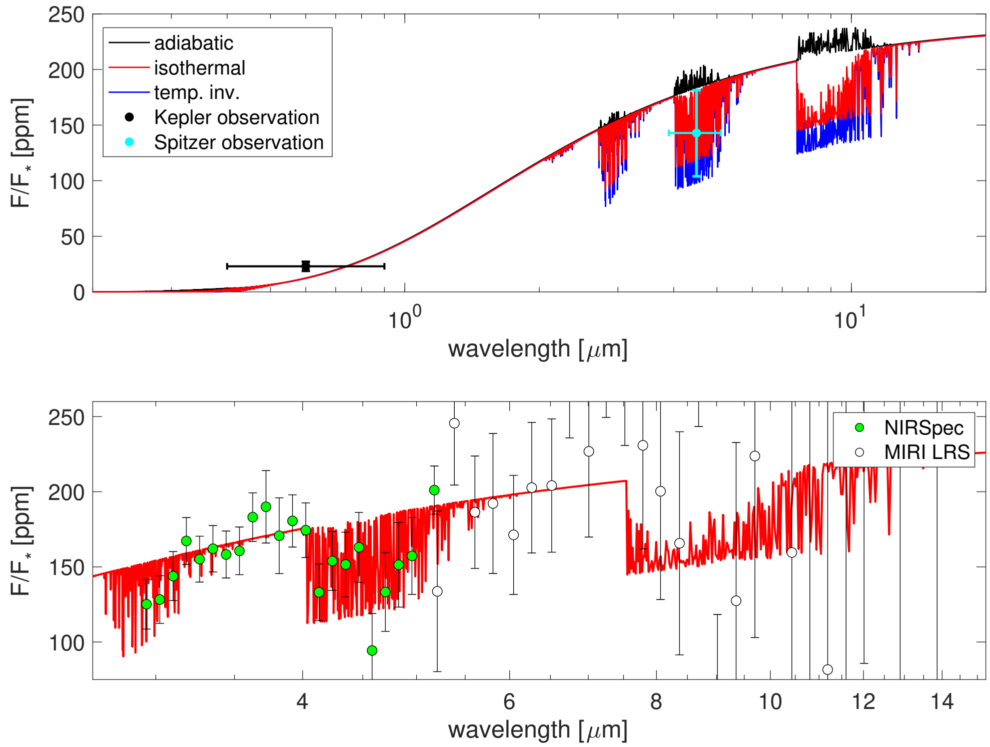

Figure 5.7: *Top*: simulated eclipse spectrum of K2-141b for three different assumed vertical temperature pressure profiles. The black dot and its bars show K2-141b's occultation depth as measured by Kepler (Malavolta et al., 2018), as well as Kepler's bandwidth (Van Cleve & Caldwell, 2016). The cyan dot and its bars likewise show the depth as measured by Spitzer (Zieba et al., 2022). The adiabatic case exhibits SiO emission features while the vertically isothermal and inverted models have absorption features. This counter-intuitive behaviour originates from the relation between vertical temperature profile, wind speed, and overall atmospheric temperature with respect to the surface. *Bottom*: simulated JWST observations at eclipse. We take the spectrum from the isothermal profile case and simulate NIRSpec and MIRI measurements for 16 eclipses using the tool PandExo (Batalha et al., 2017). Results for NIRSpec are promising and can detect the SiO absorption feature at 4–5 μm.

5.4 Future Observations

Because our atmospheric model is idealistic, the simulated observations from the model's results come with many caveats. We predict significant SiO spectral features coming from K2-141b. However, K2 and Spitzer lack the precision to definitely confirm a silicate atmosphere (Zieba et al., 2022). Upcoming observations from JWST may provide enough confidence atmospheric detection and show distinct absorptive or emission spectral features which can be compared to our theoretical predictions.

The simulated transmission spectra of K2-141b shows that current instruments, even JWST, cannot detect the planet's atmosphere through transit observations. However, with proposed future instruments such as LUVOIR (Large UV, Optical, IR surveyor), we can better detect signals in the UV range. The simulated transmission spectra then become useful for predicting LUVOIR observations because of the large UV signal as seen in Fig. 5.3.

The additional observational range in the optical would also be useful for better understanding of lava planet dynamics. The visible wavelengths are particularly useful for cloud detection which has huge implications on the planet's climate. Clouds have their own optical properties where spectral data can be used to infer atmospheric composition (Kitzmann & Heng, 2018). With better understood cloud properties, we can parameterized RT in the optical just as we did with IR and UV in the model. The results will likely be substantially significant as most of the star's radiation is in the visible wavelength.

5.5 Chapter Conclusions

We simulated the transit spectrum of K2-141b (Fig. 5.3) and found that the UV radiated atmosphere of Chapter 4 is much wamrmer than what was previously predicted from Chapter 3 which should lead to a much bigger scale height. Despite this, the surface pressure is very small and so features in the IR are too subtle for Spitzer or JWST to detect; the stronger SiO feature in the UV will likely have to wait for a more sensitive spectrograph than is currently available on Hubble.

Our simulated eclipse spectra of K2-141b (Fig. 5.7) are more promising. Because the different vertical temperature profiles lead to different dayside atmospheric temperatures, emission spectra ought to be distinguishable with Spitzer and JWST. The adiabatic profile has a warmer atmosphere so its spectrum has significant SiO emission features. The isothermal and inverted vertical temperature profiles, on the other hand, produce atmospheres cooler than the surface and hence SiO absorption features. Emission spectra are not only useful for detecting the atmosphere, but can also help to infer more nuanced properties such as vertical temperature profile.

6 | Conclusions

The research in this thesis follows the theme of exploring inner solar system dynamics and apply them to exoplanets. We focus on the atmosphere because of its importance for life on Earth, and it is often the first and only thing we see of other planets or moons. The atmosphere plays a vital role in material distribution on the surface and so we first study how water migrates in the exosphere across a diverse set of icy bodies. When presented with the challenge to characterize lava planets, the icy moons in the solar system provided great insight. We adopt the modelling techniques used for icy moons to predict conditions on the lava planet K2-141b. We uncover an extreme world with weather literally made of rocks. The lava planet modeling contributed to several publications and prompted further observations of lava planets. Therefore, the thesis can mainly be split into two parts: theoretical prediction of water transport in exospheres and characterizing the possible atmospheres of lava planets.

6.1 Water Migration in Exospheres

In Chapter 2, we modelled the non-collisional atmospheres of small planetoids to study how planetary properties affect water migration. Our results show while small bodies are prone to lose water from thermal escape, big bodies are also prone to lose water from photodissociation. Therefore, there is an ideal size, given the bulk composition and stellar radiation, that maximizes how much water is cold-trapped in the planet's permanently shadowed regions.

We find that the Moon is ideally sized for cold-trapping water molecules where it should trap about $\sim$20% of sublimated water molecules. This is consistent with other numerical studies for the Moon. Mercury, however, is too irradiated and large; it would lose most of its water due to photodissociation. Despite this, the Moon is observed to have less polar ice than Mercury suggesting that external processes such as meteor impacts, either cause the Moon to lose its water or allow Mercury to retain water.

Exospheric dynamics depend significantly on the composition of the sublimated volatiles. Both photo-dissociation and ballistic motion depends on the molecule's shape and mass which means that the planetary properties that favour cold-trapping water can be different for other molecules such as CO_2 and CH_4. This suggests that different airless bodies will favour cold-trapping specific molecules moreso than other planetoids. This has stronger implications for exoplanets given the vast diversity in planet types beyond our solar system.

6.2 Lava Planet Modelling and Observing

Chapters 3 - 5 featured simulating lava planet K2-141b's atmosphere and observations. Our model produces a thin silicate atmosphere that is largely confined to the dayside. While the magma ocean covers most of the dayside, the ocean's flow is unlikely fast enough to replenish highly volatile molecules. Therefore, the atmosphere may be starved of constituents like Na leading to dominantly SiO atmosphere. This work is one of the first work to characterize K2-141b's atmosphere and provide unique insights into non-global atmospheric dynamics of lava planets.

With a silicate atmosphere, stellar radiation absorption cannot be neglected. We coupled radiative transfer processes to the existing hydrodynamical model, the first to do so for lava planets. The new results showed that when pressure is low, the horizontal temperature becomes homogeneous. This is a result of the atmosphere's stellar UV absorption and radiative cooling in the UV reaching an equilibrium leading to a more gradual horizontal change in temperature. We also found that a large negative lapse rate caused by upper level UV heating induces strong winds and make the atmosphere cooler than previous thought.

Finally, we simulated the transit spectra and found that current instruments do not have the adequate precision to detect features in the IR range. However, there is a significant spectral feature in the UV which may be observable with future instruments such as LUVOIR. The simulated emission spectra, on the other hand, do show features detectable with current instruments. K2-141b is one of the best target to observe due to its exceptionally high signal-to-noise ratio and it may be the first rocky exoplanet to have its atmosphere detected.

These chapters have resulted in the publications Nguyen et al. (2020) and Nguyen et al. (2022). This modeling work was used for a successful observation proposal of K2-141b by JWST (Dang et al., 2021). It was also used to help with interpreting K2 and Spitzer data of the lava planet (Zieba et al., 2022). Upon publication, this research also generated significant public interest (Prior, 2020).

6.3 Future Work

There are many avenues of improvement for the work done in this dissertation. The exospheric study in Chapter 2 can yield more precise results by having a finer grid of parameters to be simulated so that data would not need to be interpolated. Because we use a Monte Carlo model, having more simulated tracers also add to the precision. Parameters that should additionally be tested are obliquity, eccentricity, and the diurnal period. These parameters may introduce dynamics that significantly vary ballistic timescales and photodissociation timescales, and subsequently alter how much water can be cold-trapped.

For the lava planet studies of Chapter 3 - 4, the work evolved to eliminate many of the original model's limitations, such as assuming a completely transparent atmosphere, neglecting the energy transfer from the surface, and having a uniform adiabatic temperature profile. The logical next step is to eliminate more assumptions and introduce processes such as cloud formation, chemical interactions of a complex atmosphere, and truly coupling the magma ocean to the atmosphere.

Our model calculates the evaporation and deposition rate of the magma ocean. When the atmosphere is oversaturated and is colder than the dew point temperature of SiO, we would expect condensation to take place. If we can implement a general parameterization for the size of cloud droplets and their abundance, this would greatly improve the dynamics and change how we observe lava planets. Clouds can reflect visible light which can drastically cool the atmosphere and the surface since almost all of the instellation comes from that spectral range. The reflected visible light may also produce a significant signal that is detectable with the Hubble Space Telescope.

Another aspect we neglected in our model is that SiO comes from SiO_2 and therefore the production of SiO includes the side product of monoatomic Oxygen. Oxygen has its own spectral features and thermodynamic properties, and may combine to make O_2 which further complicates the physics. In the model, we can split up the atmospheric pressure into partial pressure of each constituent, and implement a weighted average for thermodynamic variables such as heat capacity and density. However, the difficulty lies in determining the evaporation rate, as O and O_2 have different saturated vapour pressures.

Finally, we have treated the magma ocean as an endless source and sink for volatiles, and thus evaporation and condensation depend only on the atmosphere's saturation. However, the magma ocean has its own saturation of volatiles that can inhibit or promote evaporation and deposition. Another next step is to couple results from oceanic modelling of lava planets (Boukaré, Cowan, & Badro, 2022) to the atmosphere and achieve more realistic simulations.

Bibliography

Ballester, G. E., McGrath, M., Strobel, D., Zhu, X., Feldman, P. D., & Moos, H. (1994). Detection of the so2 atmosphere on io with the hubble space telescope. *Icarus*, *111*(1), 2–17.

Barragán, O, Gandolfi, D, Dai, F, Livingston, J, Persson, C., Hirano, T, Narita, N, Csizmadia, S., Winn, J., Nespral, D, et al. (2018). K2-141 b-a 5-m super-earth transiting a k7 v star every 6.7 h. *Astronomy & Astrophysics*, *612*, A95.

Barstow, J. K., Aigrain, S., Irwin, P. G., & Sing, D. K. (2016). A consistent retrieval analysis of 10 hot jupiters observed in transmission. *The Astrophysical Journal*, *834*(1), 50.

Barton, E. J., Yurchenko, S. N., & Tennyson, J. (2013). Exomol line lists–ii. the ro-vibrational spectrum of sio. *Monthly Notices of the Royal Astronomical Society*, *434*(2), 1469–1475.

Batalha, N. M., Borucki, W. J., Bryson, S. T., Buchhave, L. A., Caldwell, D. A., Christensen-Dalsgaard, J., Ciardi, D., Dunham, E. W., Fressin, F., Gautier III,

T. N., et al. (2011). Kepler's first rocky planet: Kepler-10b. *The Astrophysical Journal*, *729*(1), 27.

Batalha, N. E., Mandell, A., Pontoppidan, K., Stevenson, K. B., Lewis, N. K., Kalirai, J., Earl, N., Greene, T., Albert, L., & Nielsen, L. D. (2017). Pandexo: A community tool for transiting exoplanet science with jwst & hst. *Publications of the Astronomical Society of the Pacific*, *129*(976), 064501.

Bell, T. J., & Cowan, N. B. (2018). Increased heat transport in ultra-hot jupiter atmospheres through h2 dissociation and recombination. *The Astrophysical Journal Letters*, *857*(2), L20.

Benna, M, Hurley, D., Stubbs, T., Mahaffy, P., & Elphic, R. (2019). Lunar soil hydration constrained by exospheric water liberated by meteoroid impacts. *Nature geoscience*, *12*(5), 333–338.

Birkmann, S. M., Ferruit, P., Rawle, T., Sirianni, M., de Oliveira, C. A., Böker, T., Giardino, G., Lützgendorf, N., Marston, A., Stuhlinger, M., et al. The jwst/nirspec instrument: Update on status and performances. In: *Space telescopes and instrumentation 2016: Optical, infrared, and millimeter wave*. *9904*. International Society for Optics and Photonics. 2016, 99040B.

Boukaré, C.-É., Cowan, N. B., & Badro, J. (2022). Deep two-phase, hemispherical magma oceans on lava planets. *arXiv preprint arXiv:2205.02864*.

Burrows, A. S. (2014). Highlights in the study of exoplanet atmospheres. *Nature*, *513*(7518), 345–352.

Butler, B. J. (1997). The migration of volatiles on the surfaces of mercury and the moon. *Journal of Geophysical Research: Planets*, *102*(E8), 19283–19291.

Castan, T., & Menou, K. (2011). Atmospheres of hot super-earths. *The Astrophysical Journal Letters*, *743*(2), L36.

Catling, D. C., & Kasting, J. F. (2017). *Atmospheric evolution on inhabited and lifeless worlds*. Cambridge University Press. https://doi.org/10.1017/9781139020558

Charbonneau, D., Brown, T. M., Latham, D. W., & Mayor, M. (1999). Detection of planetary transits across a sun-like star. *The Astrophysical Journal*, *529*(1), L45.

Chase Jr, M. W. (1998). Nist-janaf thermochemical tables. *J. Phys. Chem. Ref. Data, Monograph*, *9*.

Cowan, N. B., & Agol, E. (2008). Inverting phase functions to map exoplanets. *The Astrophysical Journal Letters*, *678*(2), L129.

Cowan, N. B., & Agol, E. (2011). The statistics of albedo and heat recirculation on hot exoplanets. *The Astrophysical Journal*, *729*(1), 54.

Crovisier, J. (1989). The photodissociation of water in cometary atmospheres. *Astronomy and Astrophysics*, *213*, 459–464.

Dang, L., Cowan, N. B., Hammond, M., Kreidberg, L., Lupu, R., Miguel, Y., Nguyen, G., Pierrehumbert, R., Zieba, S., & Zilinskas, M. (2021). A hell of a phase curve: Mapping the surface and atmosphere of a lava planet k2-141b. *JWST Proposal. Cycle 1*, 2347.

Deutsch, A. N., Neumann, G. A., & Head, J. W. (2017). New evidence for surface water ice in small-scale cold traps and in three large craters at the north polar region of mercury from the mercury laser altimeter. *Geophysical Research Letters*, *44*(18), 9233–9241.

Ding, F., & Pierrehumbert, R. T. (2018). Global or local pure condensible atmospheres: Importance of horizontal latent heat transport. *The Astrophysical Journal*, *867*(1), 54.

Dongari, N., & Agrawal, A. (2012). Modeling of navier–stokes equations for high knudsen number gas flows. *International Journal of Heat and Mass Transfer*, *55*(15-16), 4352–4358.

Ermakov, A., Mazarico, E, Schröder, S., Carsenty, U., Schorghofer, N, Preusker, F., Raymond, C., Russell, C., & Zuber, M. T. (2017). Ceres's obliquity history and its implications for the permanently shadowed regions. *Geophysical Research Letters*, *44*(6), 2652–2661.

Essack, Z., Seager, S., & Pajusalu, M. (2020). Low-albedo surfaces of lava worlds. *The Astrophysical Journal*, *898*(2), 160.

France, K., Arulanantham, N., Fossati, L., Lanza, A. F., Loyd, R. P., Redfield, S., & Schneider, P. C. (2018). Far-ultraviolet activity levels of f, g, k, and m dwarf exoplanet host stars. *The Astrophysical Journal Supplement Series*, *239*(1), 16.

France, K., Loyd, R. P., Youngblood, A., Brown, A., Schneider, P. C., Hawley, S. L., Froning, C. S., Linsky, J. L., Roberge, A., Buccino, A. P., et al. (2016). The muscles treasury survey. i. motivation and overview. *The Astrophysical Journal*, *820*(2), 89.

Frantseva, K., Nesvorný, D., Mueller, M., van der Tak, F. F., ten Kate, I. L., & Pokorný, P. (2022). Exogenous delivery of water to mercury. *Icarus*, 114980.

Gladstone, G. R., & Young, L. A. (2019). New horizons observations of the atmosphere of pluto. *Annual Review of Earth and Planetary Sciences*, *47*, 119–140.

Gordon, I. E., Rothman, L. S., Hill, C., Kochanov, R. V., Tan, Y, Bernath, P. F., Birk, M., Boudon, V, Campargue, A., Chance, K., et al. (2017). The hitran2016 molecular spectroscopic database. *Journal of Quantitative Spectroscopy and Radiative Transfer*, *203*, 3–69.

Green, J. C., Froning, C. S., Osterman, S., Ebbets, D., Heap, S. H., Leitherer, C., Linsky, J. L., Savage, B. D., Sembach, K., Shull, J. M., et al. (2011). The cosmic origins spectrograph. *The Astrophysical Journal*, *744*(1), 60.

Han, E., Wang, S. X., Wright, J. T., Feng, Y. K., Zhao, M., Fakhouri, O., Brown, J. I., & Hancock, C. (2014). Exoplanet orbit database. ii. updates to exoplanets. org. *Publications of the Astronomical Society of the Pacific*, *126*(943), 827.

Hayne, P. O., Aharonson, O., & Schörghofer, N. (2021). Micro cold traps on the moon. *Nature Astronomy*, *5*(2), 169–175.

Ingersoll, A. P., Summers, M. E., & Schlipf, S. G. (1985). Supersonic meteorology of io: Sublimation-driven flow of so2. *Icarus*, *64*(3), 375–390.

Ito, Y., & Ikoma, M. (2021). Hydrodynamic escape of mineral atmosphere from hot rocky exoplanet. i. model description. *Monthly Notices of the Royal Astronomical Society*, *502*(1), 750–771.

Ito, Y., Ikoma, M., Kawahara, H., Nagahara, H., Kawashima, Y., & Nakamoto, T. (2015). Theoretical emission spectra of atmospheres of hot rocky super-earths. *The Astrophysical Journal*, *801*(2), 144.

Jolicard, G, Zucconi, J.-M., Drira, I, Spielfieldel, A, & Feautrier, N. (1997). The photodissociation of sio. *The Journal of chemical physics*, *106*(24), 10105–10112.

Kempton, E. M.-R., & Rauscher, E. (2012). Constraining high-speed winds in exoplanet atmospheres through observations of anomalous doppler shifts during transit. *The Astrophysical Journal*, *751*(2), 117.

Killen, R. M., Burger, M. H., & Farrell, W. M. (2018). Exospheric escape: A parametrical study. *Advances in Space Research*, *62*(8), 2364–2371.

Kite, E. S., Fegley Jr, B., Schaefer, L., & Gaidos, E. (2016). Atmosphere-interior exchange on hot, rocky exoplanets. *The Astrophysical Journal*, *828*(2), 80.

Kitzmann, D., & Heng, K. (2018). Optical properties of potential condensates in exoplanetary atmospheres. *Monthly Notices of the Royal Astronomical Society*, *475*(1), 94–107.

Kloos, J. L., Moores, J. E., Sangha, J., Nguyen, T. G., & Schorghofer, N. (2019). The temporal and geographic extent of seasonal cold trapping on the moon. *Journal of Geophysical Research: Planets*, *124*(7), 1935–1944.

Koch, D. G., Borucki, W., Dunham, E., Geary, J., Gilliland, R., Jenkins, J., Latham, D., Bachtell, E., Berry, D., Deininger, W., et al. Overview and status of the kepler mission. In: *Optical, infrared, and millimeter space telescopes. 5487*. International Society for Optics and Photonics. 2004, 1491–1500.

Kopal, Z. (1954). Photometric effects of reflection in close binary systems. *Monthly Notices of the Royal Astronomical Society*, *114*(1), 101–117.

Kreidberg, L., Lopez, E., Cowan, N., Lupu, R., Stevenson, K., Louden, T., & Malavolta, L. (2018). Taking the temperature of a lava planet. *Spitzer Proposal*.

Kurucz, R. L. (1992). Atomic and molecular data for opacity calculations. *Revista Mexicana de Astronomia y Astrofisica, vol. 23*, *23*.

Langmuir, I. (1916). The evaporation, condensation and reflection of molecules and the mechanism of adsorption. *Physical Review*, *8*(2), 149.

Lean, J., & Skumanich, A. (1983). Variability of the lyman alpha flux with solar activity. *Journal of Geophysical Research: Space Physics*, *88*(A7), 5751–5759.

Léger, A., Grasset, O, Fegley, B, Codron, F, Albarede, A., Barge, P, Barnes, R, Cance, P, Carpy, S, Catalano, F, et al. (2011). The extreme physical properties of the corot-7b super-earth. *Icarus*, *213*(1), 1–11.

Lim, H., Kim, T., Eom, S., Sung, Y.-i., Moon, M. H., & Lee, D. (2002). Vaporization process of sio 2 particles for slurry injection in inductively coupled plasma atomic emission spectrometry. *Journal of Analytical Atomic Spectrometry*, *17*(2), 109–114.

Machol, J, Snow, M, Woodraska, D, Woods, T, Viereck, R, & Coddington, O. (2019). An improved lyman-alpha composite. *Earth and Space Science*, *6*(12), 2263–2272.

Madhusudhan, N., Crouzet, N., McCullough, P. R., Deming, D., & Hedges, C. (2014). H2o abundances in the atmospheres of three hot jupiters. *The Astrophysical Journal Letters*, *791*(1), L9.

Malavolta, L., Mayo, A. W., Louden, T., Rajpaul, V. M., Bonomo, A. S., Buchhave, L. A., Kreidberg, L., Kristiansen, M. H., Lopez-Morales, M., Mortier, A., et al. (2018). An ultra-short period rocky super-earth with a secondary eclipse and a neptune-like companion around k2-141. *The Astronomical Journal*, *155*(3), 107.

Mansfield, M., Bean, J. L., Stevenson, K. B., Komacek, T. D., Bell, T. J., Tan, X., Malik, M., Beatty, T. G., Wong, I., Cowan, N. B., et al. (2020). Evidence for h2 dissociation and recombination heat transport in the atmosphere of kelt-9b. *The Astrophysical Journal Letters*, *888*(2), L15.

Mayor, M., & Queloz, D. (1995). A jupiter-mass companion to a solar-type star. *Nature*, *378*(6555), 355–359.

McGovern, J. A., Bussey, D. B., Greenhagen, B. T., Paige, D. A., Cahill, J. T., & Spudis, P. D. (2013). Mapping and characterization of non-polar permanent shadows on the lunar surface. *Icarus*, *223*(1), 566–581.

Mehio, N., Dai, S., & Jiang, D.-e. (2014). Quantum mechanical basis for kinetic diameters of small gaseous molecules. *The Journal of Physical Chemistry A*, *118*(6), 1150–1154.

Miguel, Y, Kaltenegger, L, Fegley, B, & Schaefer, L. (2011). Compositions of hot super-earth atmospheres: Exploring kepler candidates. *The Astrophysical Journal Letters*, *742*(2), L19.

Mogan, S. R. C., Tucker, O. J., Johnson, R. E., Vorburger, A., Galli, A., Marchand, B., Tafuni, A., Kumar, S., Sahin, I., & Sreenivasan, K. R. (2021). A tenuous, collisional atmosphere on callisto. *Icarus*, *368*, 114597.

Moores, J. E. (2016). Lunar water migration in the interval between large impacts: Heterogeneous delivery to permanently shadowed regions, fractionation, and diffusive barriers. *Journal of Geophysical Research: Planets*, *121*(1), 46–60.

Nguyen, T. G., Cowan, N. B., Banerjee, A., & Moores, J. E. (2020). Modelling the atmosphere of lava planet k2-141b: Implications for low-and high-resolution spectroscopy. *Monthly Notices of the Royal Astronomical Society*, *499*(4), 4605–4612.

Nguyen, T. G., Cowan, N. B., Pierrehumbert, R. T., Lupu, R. E., & Moores, J. E. (2022). The impact of ultraviolet heating and cooling on the dynamics and observability of lava planet atmospheres. *Monthly Notices of the Royal Astronomical Society*, *513*(4), 6125–6133.

Prem, P., Artemieva, N., Goldstein, D., Varghese, P., & Trafton, L. (2015). Transport of water in a transient impact-generated lunar atmosphere. *Icarus*, *255*, 148–158.

Prior, R. (2020). *This lava planet has 'rocky' weather and winds many times the speed of sound*. Retrieved November 6, 2020, from https://www.cnn.com/2020/11/06/world/lava-exoplanet-scn-trnd

Roth, L., Ivchenko, N., Gladstone, G. R., Saur, J., Grodent, D., Bonfond, B., Molyneux, P. M., & Retherford, K. D. (2021). A sublimated water atmosphere on ganymede detected from hubble space telescope observations. *Nature Astronomy*, *5*(10), 1043–1051.

Rubanenko, L., Venkatraman, J., & Paige, D. A. (2019). Thick ice deposits in shallow simple craters on the moon and mercury. *Nature Geoscience*, *12*(8), 597–601.

Rugheimer, S, Segura, A, Kaltenegger, L, & Sasselov, D. (2015). Uv surface environment of earth-like planets orbiting fgkm stars through geological evolution. *The Astrophysical Journal*, *806*(1), 137.

Rugheimer, S., Kaltenegger, L., Zsom, A., Segura, A., & Sasselov, D. (2013). Spectral fingerprints of earth-like planets around fgk stars. *Astrobiology*, *13*(3), 251–269.

Sandford, S. A., & Allamandola, L. J. (1988). The condensation and vaporization behavior of h2o: Co ices and implications for interstellar grains and cometary activity. *Icarus*, *76*(2), 201–224.

Schaefer, L., & Fegley, B. (2009). Chemistry of silicate atmospheres of evaporating super-earths. *The Astrophysical Journal Letters*, *703*(2), L113.

Schorghofer, N. (2014). Migration calculations for water in the exosphere of the moon: Dusk-dawn asymmetry, heterogeneous trapping, and d/h fractionation. *Geophysical Research Letters*, *41*(14), 4888–4893.

Schörghofer, N., Benna, M., Berezhnoy, A. A., Greenhagen, B., Jones, B. M., Li, S., Orlando, T. M., Prem, P., Tucker, O. J., & Wöhler, C. (2021). Water group exospheres and surface interactions on the moon, mercury, and ceres. *Space Science Reviews*, *217*(6), 1–35.

Schorghofer, N., Mazarico, E., Platz, T., Preusker, F., Schröder, S. E., Raymond, C. A., & Russell, C. T. (2016). The permanently shadowed regions of dwarf planet ceres. *Geophysical Research Letters*, *43*(13), 6783–6789.

Schorghofer, N., & Taylor, G. J. (2007). Subsurface migration of h2o at lunar cold traps. *Journal of Geophysical Research: Planets*, *112*(E2).

Shematovich, V., Johnson, R., Cooper, J., & Wong, M. (2005). Surface-bounded atmosphere of europa. *Icarus*, *173*(2), 480–498.

Snellen, I. (2014). High-dispersion spectroscopy of extrasolar planets: From co in hot jupiters to o2 in exo-earths. *Philosophical Transactions of the Royal Society A: Mathematical, Physical and Engineering Sciences*, *372*(2014), 20130075.

Stassun, K. G., Oelkers, R. J., Paegert, M., Torres, G., Pepper, J., De Lee, N., Collins, K., Latham, D. W., Muirhead, P. S., Chittidi, J., et al. (2019). The revised tess input catalog and candidate target list. *The Astronomical Journal*, *158*(4), 138.

Steckloff, J. K., Goldstein, D., Trafton, L., Varghese, P., & Prem, P. (2022). Exosphere-mediated migration of volatile species on airless bodies across the solar system. *Icarus*, 115092.

Strobel, D. F., & Wolven, B. C. The atmosphere of io: Abundances and sources of sulfur dioxide and atomic hydrogen. In: *Physics of space: Growth points and problems*. Springer, 2001, pp. 271–287.

Swamy, V, Saxena, S. K., Sundman, B., & Zhang, J. (1994). A thermodynamic assessment of silica phase diagram. *Journal of Geophysical Research: Solid Earth*, *99*(B6), 11787–11794.

Tan, X., & Komacek, T. D. (2019). The atmospheric circulation of ultra-hot jupiters. *The Astrophysical Journal*, *886*(1), 26.

Tsang, C. C., Spencer, J. R., Lellouch, E., Lopez-Valverde, M. A., & Richter, M. J. (2016). The collapse of io's primary atmosphere in jupiter eclipse. *Journal of Geophysical Research: Planets*, *121*(8), 1400–1410.

Van Cleve, J. E., & Caldwell, D. A. (2016). Kepler instrument handbook. *Kepler Science Document KSCI-19033-002*, 1.

Wakeford, H. R., & Sing, D. K. (2015). Transmission spectral properties of clouds for hot jupiter exoplanets. *Astronomy & Astrophysics*, *573*, A122.

Watson, K., Murray, B. C., & Brown, H. (1961). The behavior of volatiles on the lunar surface. *Journal of Geophysical Research*, *66*(9), 3033–3045.

Wells, M., Pel, J.-W., Glasse, A., Wright, G., Aitink-Kroes, G., Azzollini, R., Beard, S., Brandl, B., Gallie, A., Geers, V., et al. (2015). The mid-infrared instrument for the james webb space telescope, vi: The medium resolution spectrometer. *Publications of the Astronomical Society of the Pacific*, *127*(953), 646.

Werner, M. W., Roellig, T., Low, F., Rieke, G. H., Rieke, M, Hoffmann, W., Young, E, Houck, J., Brandl, B, Fazio, G., et al. (2004). The spitzer space telescope mission. *The Astrophysical Journal Supplement Series*, *154*(1), 1.

Widger Jr, W., & Woodall, M. (1976). Integration of the planck blackbody radiation function. *Bulletin of the American Meteorological Society*, *57*(10), 1217–1219.

Woods, T. N., Tobiska, W. K., Rottman, G. J., & Worden, J. R. (2000). Improved solar lyman α irradiance modeling from 1947 through 1999 based on uars observations. *Journal of Geophysical Research: Space Physics*, *105*(A12), 27195–27215.

Wordsworth, R. (2015). Atmospheric heat redistribution and collapse on tidally locked rocky planets. *The Astrophysical Journal*, *806*(2), 180.

Zieba, S, Zilinskas, M, Kreidberg, L, Nguyen, T., Miguel, Y, Cowan, N., Pierrehumbert, R, Carone, L, Dang, L, Hammond, M, et al. (2022). K2 and spitzer phase curves of the rocky ultra-short-period planet k2-141 b hint at a tenuous rock vapor atmosphere. *arXiv preprint arXiv:2203.00370*.

Zilinskas, M., van Buchem, C., Miguel, Y., Louca, A., Lupu, R., Zieba, S., & van Westrenen, W. (2022). Observability of evaporating lava worlds. *Astronomy & Astrophysics*, *661*, A126.

Appendices

A | Exosphere

Table A.1: Parameters and variables used for Eq. 2.1 - Eq. 2.6

Term	Eq. featured	Description
t_{res} [s]	(2.1)	surface resident time; time it takes for volatile to stay on surface
υ_0 [s^{-1}]	(2.1)	vibrational frequency of volatile
E_{a}	(2.1)	activational energy
T_{e}	(2.1), (2.3), (2.4)	surface equilibrium temperature
D	(2.2)	Maxwell-Boltzmann molecular speed distribution
v	(2.2)	molecular speed
m	(2.2), (2.3)	molecular mass
P_{photo}	(2.5), (2.6)	probability of photodissociation
t_{photo}	(2.5), (2.6)	photodissociation timescale
d	(2.6)	distance between star and planetoid

A.1 Example of Numerical Exospheric Simulation

Figure A.1 shows the ballistic hopping simulation done by Schörghofer et al. (2021) which is similar to what we do. However, we neglect planet-specific surface conditions of Schörghofer et al. (2021) but the number of planetary cases we tested is orders of magnitude greater.

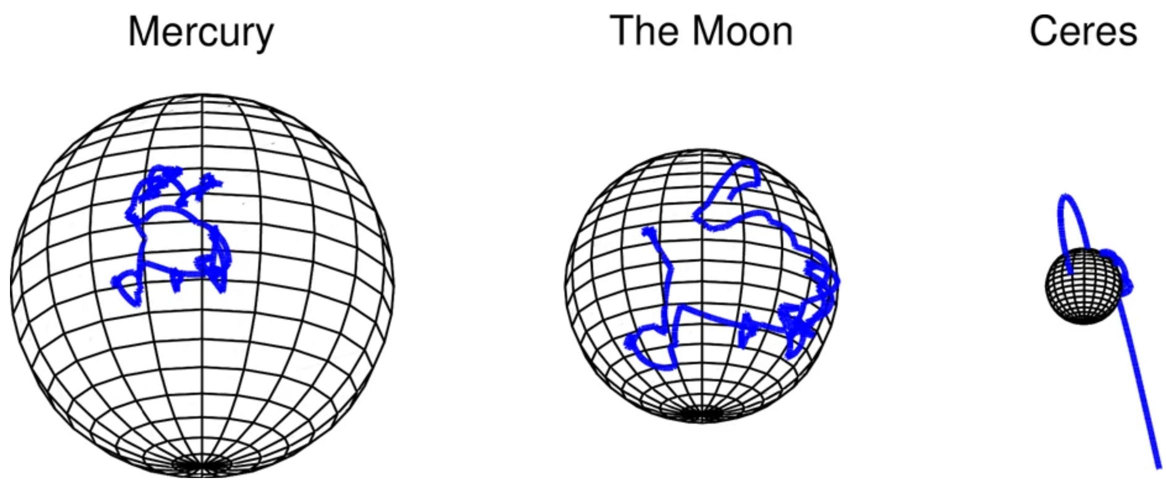

Figure A.1: Typical ballistic hopping simulation on Mercury, the Moon, and Ceres taken from Schörghofer et al. (2021).

A.2 Diagnostic Plots for Moon Simulation

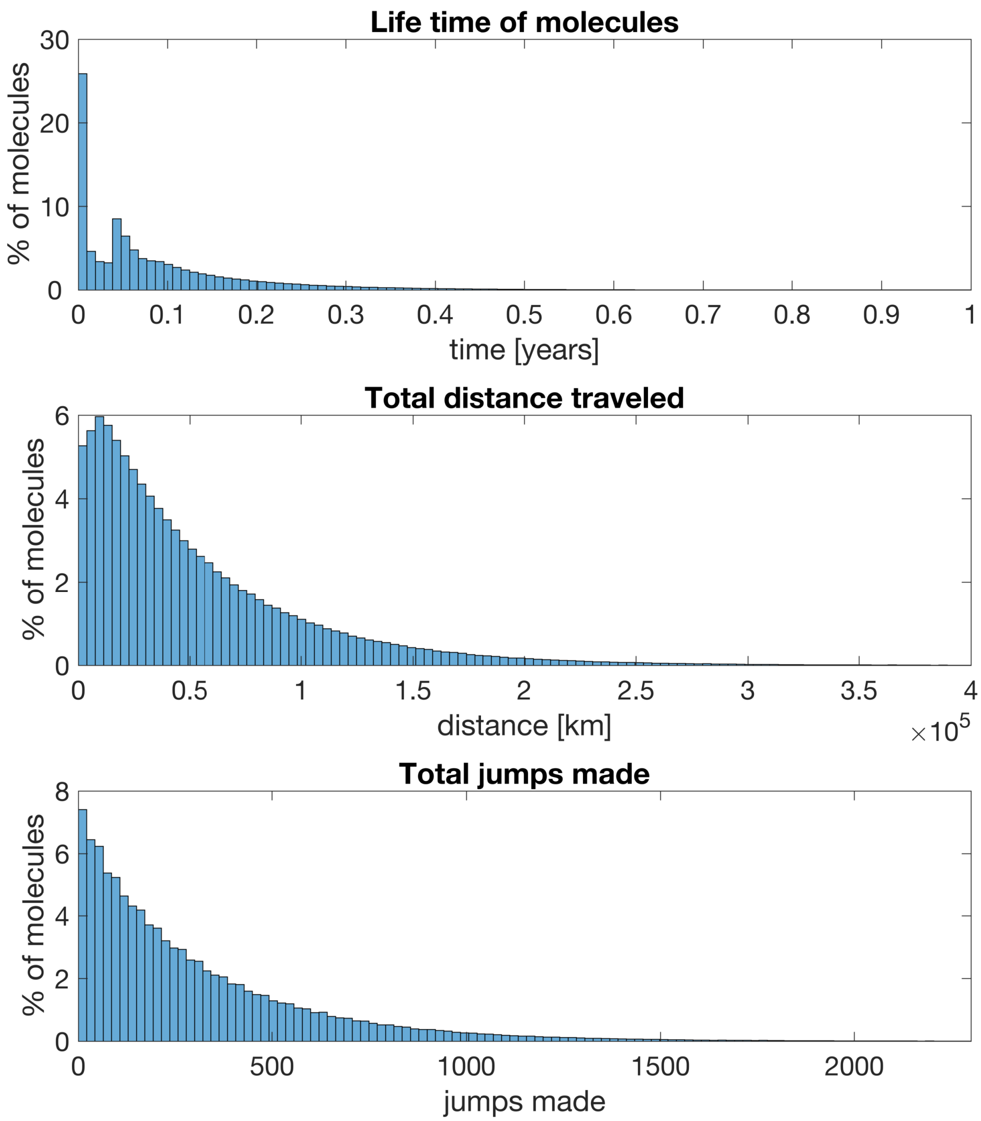

Figure A.2: Histogram of total life time, distance traveled, and jumps made for the moon.

A.3 Plots for Different Bulk Densities

Figure 2.7 shows the results when the set bulk density is 3 g cm^{-3}. The following figures, Fig. A.3 - A.6, show the results for 2, 4, 5, and 6 g cm^{-3} respectively.

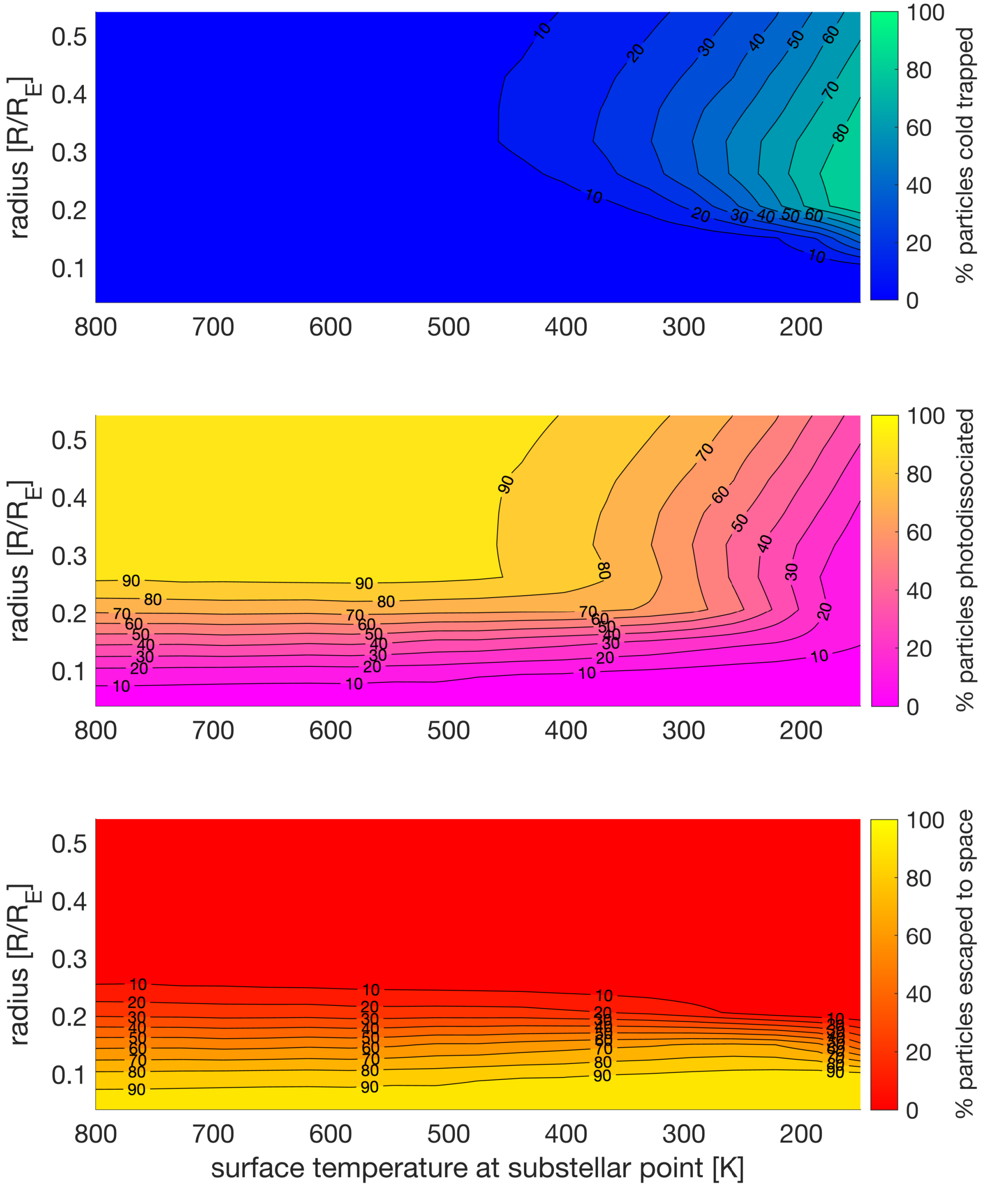

Figure A.3: Cold-trapping (*top*), photodissociation (*middle*), and thermal Jeans escape (*bottom*) within the parameter space. The bulk density is set to 2 g cm^{-3}.

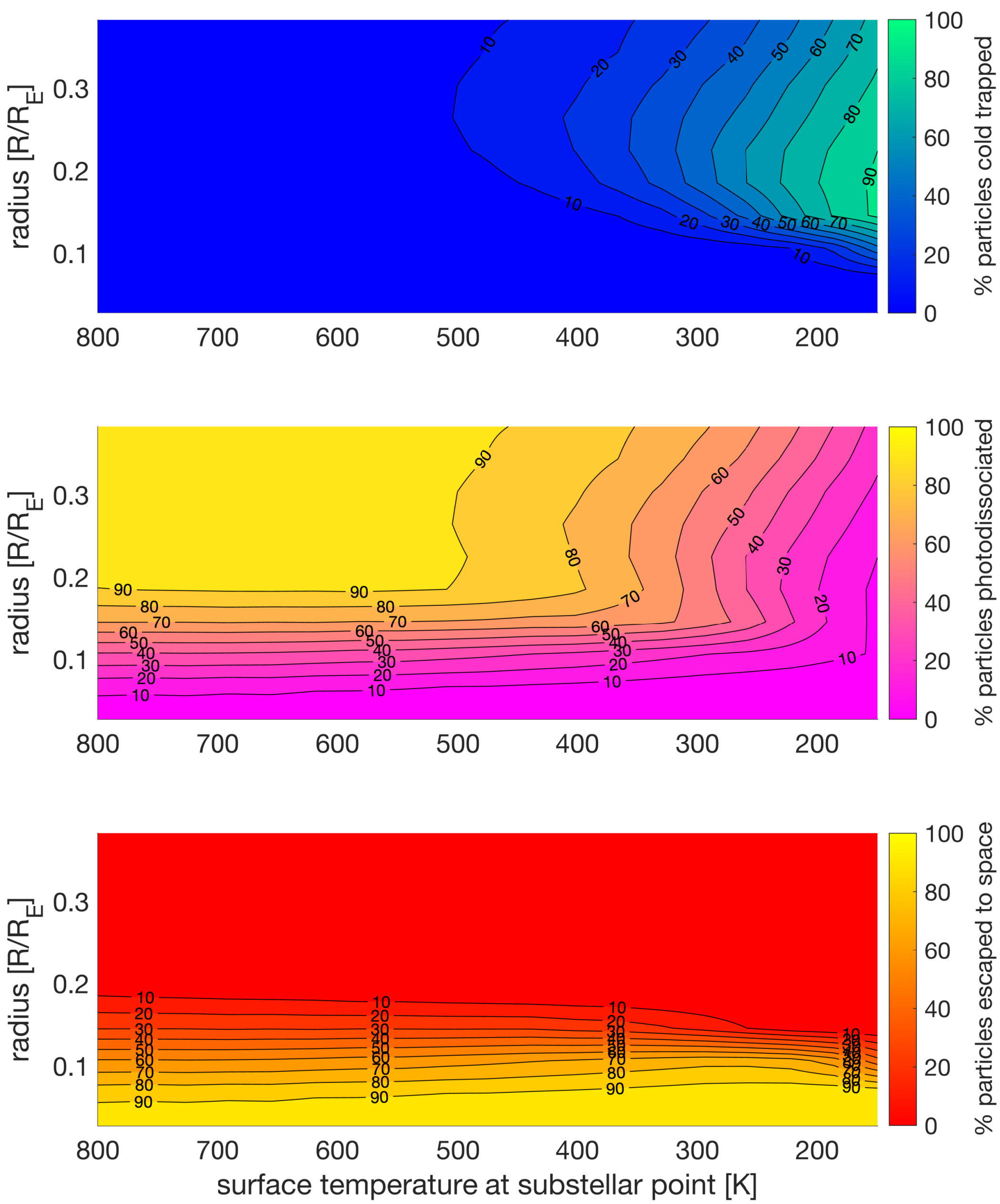

Figure A.4: Cold-trapping (*top*), photodissociation (*middle*), and thermal Jeans escape (*bottom*) within the parameter space. The bulk density is set to 4 g cm^{-3}.

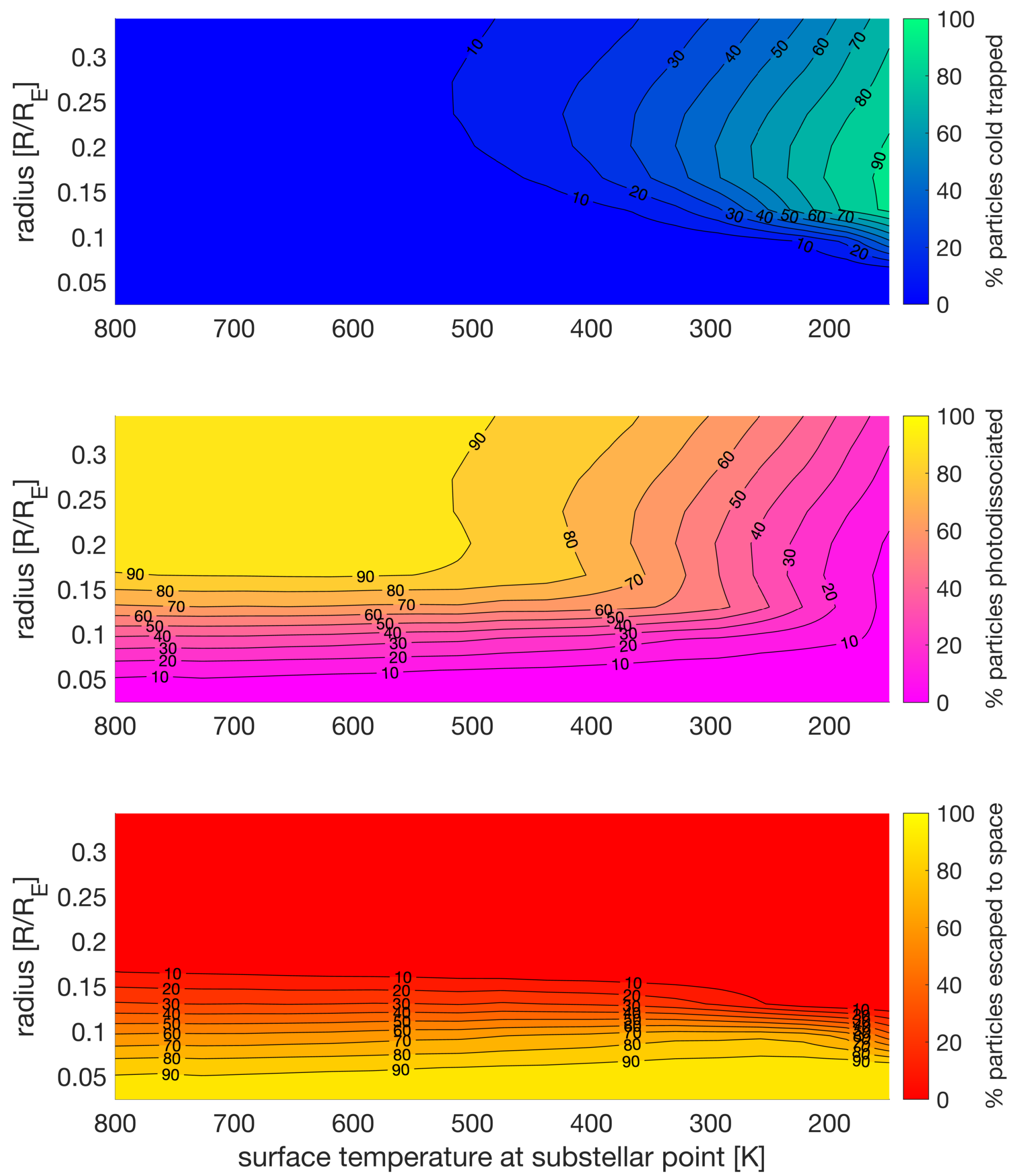

Figure A.5: Cold-trapping (*top*), photodissociation (*middle*), and thermal Jeans escape (*bottom*) within the parameter space. The bulk density is set to 5 g cm^{-3}.

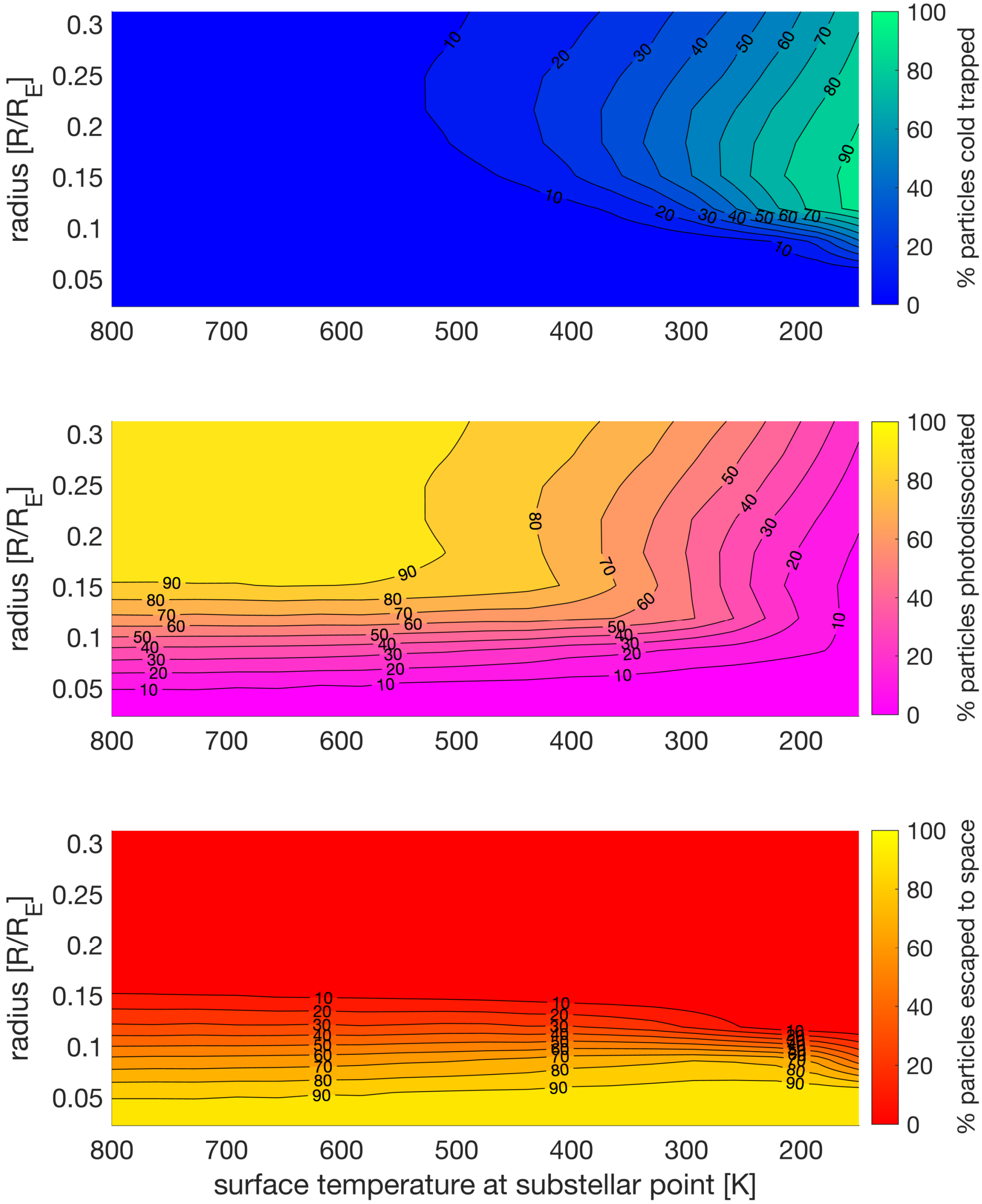

Figure A.6: Cold-trapping (*top*), photodissociation (*middle*), and thermal Jeans escape (*bottom*) within the parameter space. The bulk density is set to 6 g cm^{-3}.

B | Modelling Lava Planet

Table B.1: Parameters and variables used for Eq. 3.1 - Eq. 4.8

Term	Eq. featured	Description
r [m]	(3.2), (3.16), (3.5)	planetary radius
g [m s^{-2}]	(3.2), (3.16), (3.5)	surface gravity
m [kg molecule-1]	(3.2), (3.5)	molecular mass
E [molecules s^{-1} m^{-2}]	(3.2), (3.3)	mass flux
τ [kg m^{-2} s^{-1}]	(3.16), (3.17)	momentum flux
Q [W m^{-2}]	(3.5), (3.6)	energy flux
C_p [J kg^{-1} K^{-1}]	(3.16), (3.5)	specific heat capacity
β	(3.2), (3.5)	lapse rate scaling factor
R [J kg^{-1} K^{-1}]	(3.3)	specific gas constant
H [m]	(3.12)	atmospheric scale height
w_{s} & w_{a}	(3.6), (3.7)-(3.10)	energy transfer coefficients
V_{e} [m s^{-1}]	(3.7)-(3.10)	velocity of mean flow
V_{d} [m s^{-1}]	(3.7)-(3.10)	velocity due to eddies
V_{f} [m s^{-1}]	(3.11)	friction velocity
η [kg m^{-1} s^{-1}]	(3.11)	dynamic viscosity
ϵ_{IR}, ϵ_{UV}	(4.1), (4.4)-(4.6)	emissivity in IR and UV respectively
C_{IR}, C_{UV}	(4.1), (4.4)-(4.6)	fraction of stellar flux in IR and UV
F_{IR}, F_{UV} [W m^{-2}]	(4.1), (4.4), (4.5)	atmospheric absorption of stellar flux in IR and UV
F_* [W m^{-2}]	(4.1), (4.4) - (4.8)	total stellar flux
F_{surf} [W m^{-2}]	(4.6)	surface blackbody radiation
F_{RC} [W m^{-2}]	(4.7), (4.8)	atmospheric radiative cooling flux

Table B.2: Parameters and variables used for Eq. 5.1 - Eq. 5.5

Term	**Eq. featured**	**Description**
D_{t}	(5.1)	transit depth; fraction of starlight blocked by planet
r, r_* [m]	(5.1)	planetary and stellar radii
b [m]	(5.1)	projected distance from planet's centre to point of interest
τ_{c}	(5.1), (5.2)	optical depth from a limb observation
I [W m^{-2} m^{-1} sr^{-1}]	(5.3)	blackbody radiative intensity
F [W m^{-2}]	5.5	observed radiative flux
ξ	5.5	planet's position in its orbit

B.1 Saturated Vapour Pressure of Silicate Atmosphere

Figure B.1 shows the equilibrium saturated vapour pressure of a silicate atmosphere at different temperature from Schaefer and Fegley (2009).

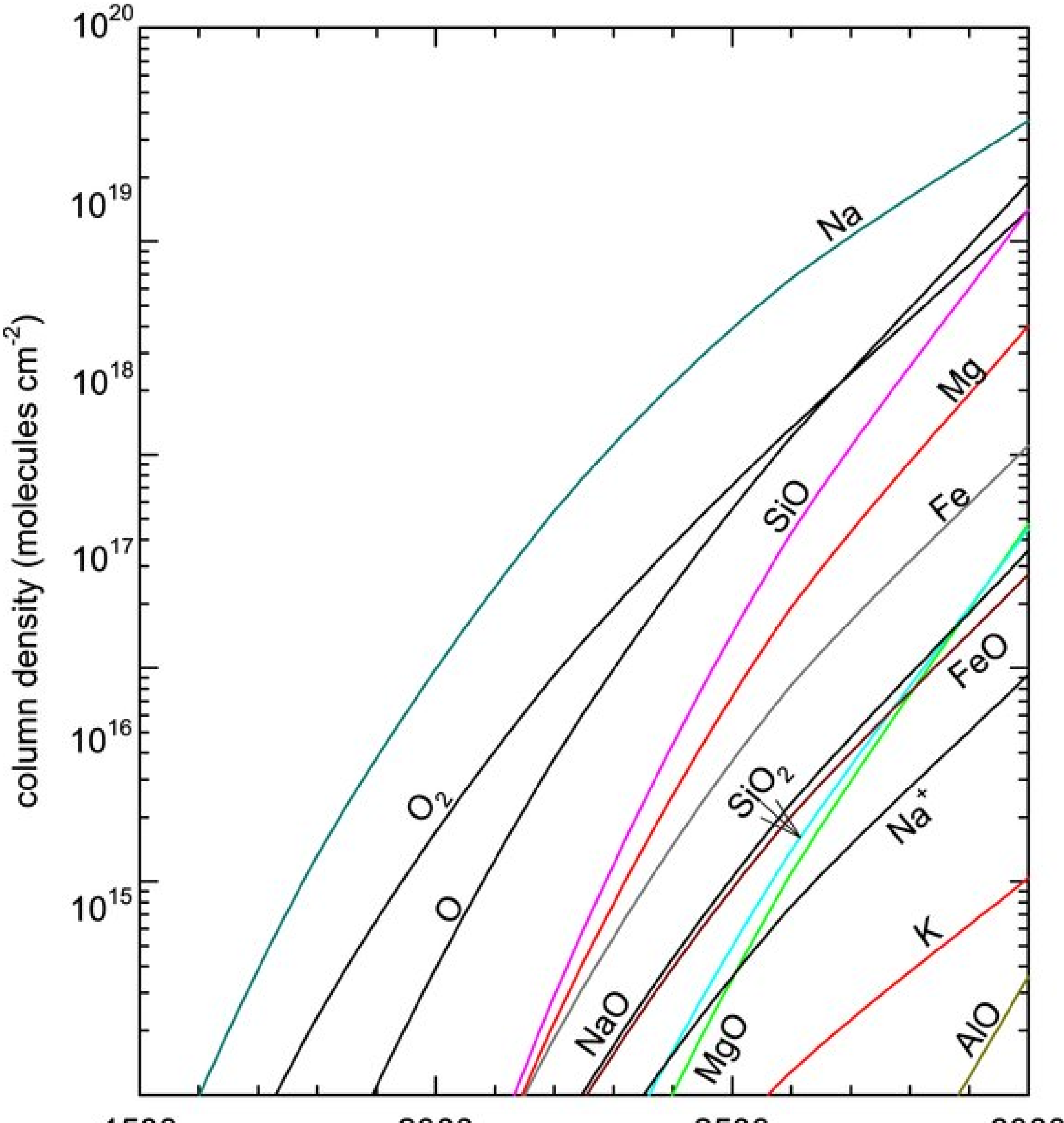

Figure B.1: Modelled atmospheric composition as a function of temperature for the Bulk Silicate Earth crust composition (Schaefer & Fegley, 2009).

B.2 Parameters for the Model

This subsection includes molecule specific parameters of Na, SiO, and SiO_2. The mass per molecule for the three constituents are: $m_{Na} = 3.82 \times 10^{-26}$ kg/molecule, $m_{SiO} = 7.32 \times 10^{-26}$ kg/molecule, and $m_{SiO_2} = 9.98 \times 10^{-26}$ kg/molecule. With this, you can compute the respective gas constant R with $R = k/m$ where k is the Boltzmann constant.

The heat capacity C_p of Na, SiO, and SiO_2 is 904 J/K/kg (Castan & Menou, 2011), 851 J/K/kg (evaluated from the Shomate equation at 2400 K provided by Chase Jr, 1998), and 1428 J/K/kg (Lim et al., 2002) respectively. With this, β can be calculated with the gas constant R where $\beta = R/(R + C_p)$.

The dynamic viscosity, η calculated from the following provided by Castan and Menou (2011): $\eta(T_s)\ [kg\ m^{-1}\ s^{-1}] = 1.8 \times 10^{-5}(T_s/291)^{3/2}(411/(T_s + 120))$.

The final component is the saturated vapour pressure approximated from the model of Schaefer and Fegley (2009) where: $P_v^{Na}[Pa] = 10^{9.6}e^{-38000/T_s}$, $P_v^{SiO}[Pa] = 6.16 \times 10^{13}e^{-69400/T_s}$, and $P_v^{SiO_2}[Pa] = 1.07 \times 10^{12}e^{-66600/T_s}$.

B.3 Definite integral of Planck function

Evaluating the radiative cooling requires a definite integral of the Planck function (Eq. 4.7). Doing the integral through finite differences can be computationally expensive but Widger Jr and Woodall (1976) provide a better alternative. We start with the definite integral of the Planck function from a wavelength λ_1 to infinity:

$$\int_{\lambda_1}^{\infty} \frac{2hc}{\lambda^5} \frac{1}{e^(hc/\lambda kT) - 1} = -\frac{2\pi k^4 T^4}{h^3 c^2} \sum_n G e^{-nJ}, \tag{B.1}$$

where $G = J^3/n + 3J^2/n^2 + 6J/n^3 + 6/n^4$ and $J = hc/(\lambda kT)$. Therefore, the definite integral between two wavelengths is:

$$\int_{\lambda_1}^{\lambda_2} (...) = \int_{\lambda_1}^{\infty} (...) - \int_{\lambda_2}^{\infty} (...), \tag{B.2}$$

and each term is calculated via the summation provided.

B.4 Vertical Temperature Profile of RT Models

Figure B.2 shows the temperature-pressure profile for lava planet atmospheres with respect to substellar surface temperature from Zilinskas et al. (2022).

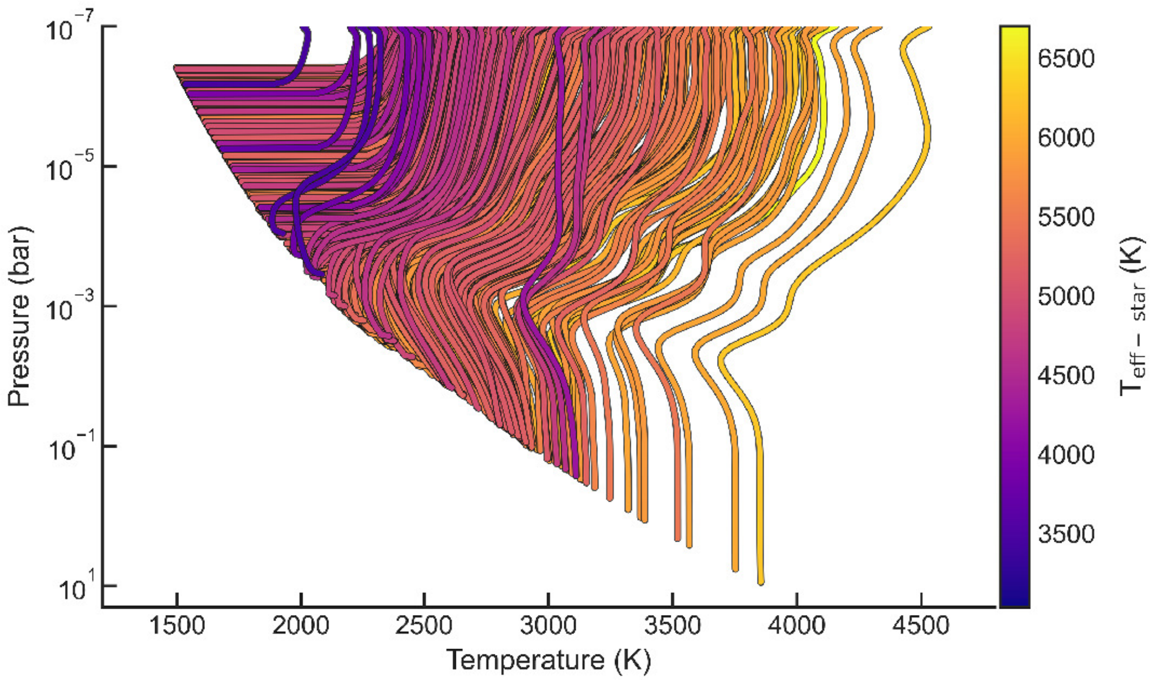

Figure B.2: Temperature-pressure profiles of confirmed lava planets with substellar surface temperatures greater than 1500 K (Zilinskas et al., 2022).

B.4.1 Definition of β

The parameter β is a lapse rate scaling factor that comes from Eq. 3.14. It is a dimensionless factor that scales the work done on the system whenever mass is evaporated from or deposited to the surface. The work done is scaled from the system's enthalpy H_* at the surface layer's boundary ($z = z_0$): $H_* = C_p\ T_*\ P_*\ /\ g$. The coefficient β can therefore be defined as:

$$\beta = \left(\int_0^{P_*} \left(T_* - T\right)\, dP \right) /\ T_*\ P_*. \tag{B.3}$$

By scaling the work done by evaporation and deposition from the enthalpy at the surface layer's boundary, we can calculate the horizontal pressure gradient that's been vertically integrated:

$$- \nabla_\theta \int_0^{\text{inf}} P(z,\theta)\ dz = \beta\ \frac{C_p}{g}\ T_*(\theta)\ P_*(\theta). \tag{B.4}$$

Note that while β depends on the T-P profile, only the integral of of TdP is essentially required. This means that the β value cannot be inverted to produce a specific T-P profile, but represents the general vertical lapse rate. Therefore, different vertical profiles can be parameterized by the same β value as seen in Fig. B.3.

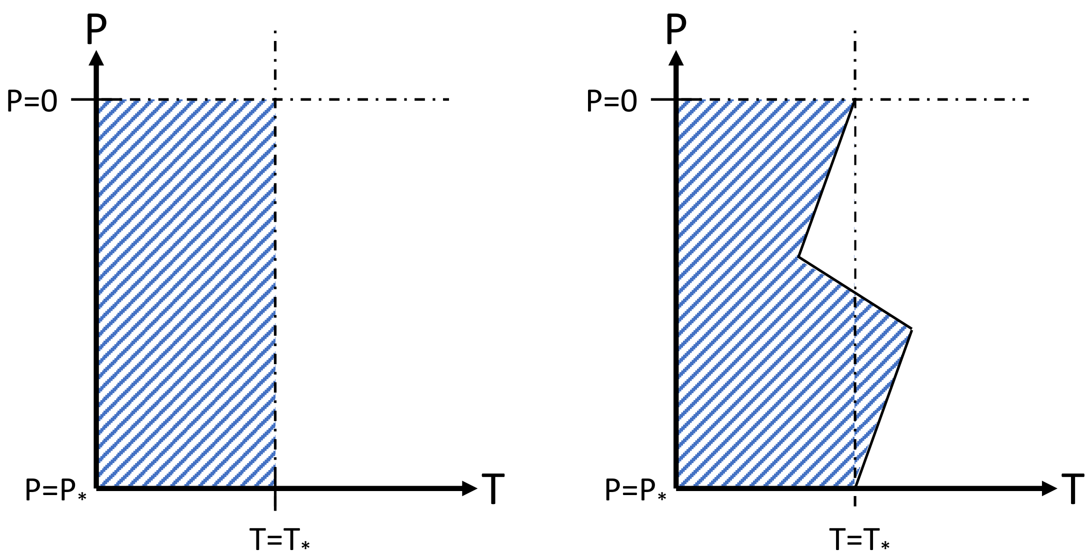

Figure B.3: The parameter β scales the work done from evaporation and deposition to the enthalpy, $C_p\ P_*\ T_*\ /\ g$ where $\int Pdz = \beta\ C_p\ P_*\ T_*\ /\ g$. Here, we use an example where $\beta = 1$ and so the highlighted area on the left panel is P_*T_*; this corresponds to a vertically isothermal atmosphere. The right panel has the same area as the left and would also be represented by the same β value. Therefore, the general lapse rate can be broadly represented by β but local lapse rate can vary significantly.